Fracturing of igneous intrusions emplaced in organic-rich shale:

Implications for hydrothermal flow, petroleum systems and exploration in volcanic basins

Ole Rabbel

Thesis
for the degree of
Philosophiae Doctor

Faculty of Mathematics and Natural Sciences
University of Oslo

June 2021

Series of dissertations submitted to the
Faculty of Mathematics and Natural Sciences, University of Oslo
No. 2441

ISSN 1501-7710

Cover: Hanne Baadsgaard Utigard.
Print production: Reprosentralen, University of Oslo.

Preface and Acknowledgements

When I first moved to Norway for an exchange year during my Bachelor studies in 2012, I did not expect to spend most of my twenties in this country, especially not in Oslo. Oslo, my Norwegian friends from Bergen said, was an unfriendly place with unfriendly people, expensive, grey, and not even with proper mountains. Nevertheless, after dropping out of my first masters studies in Germany, I did end up in Oslo. It turned out to be a fantastic decision, both personally and from an educational viewpoint. Also, the city is really nice, full of friendly people and the mountains are good enough for me. I came to the University of Oslo in 2015 with the clear aim of specializing in seismic exploration and reservoir geophysics – it seemed to be a great idea at the time. Now, six years and a quarter global energy transition later, I find myself writing a Ph.D. thesis about thermo-hydro-mechanical-chemical processes around magmatic intrusions emplaced in shale, with only one of four papers addressing seismic exploration. This unexpected transition of interest has not only broadened my view of the geosciences, but also gave me the opportunity to meet many people in Norway and around the planet, which have become good friends. For this I am incredibly thankful, and I believe that it is the most important results of this work.

Of course, I would like to thank a couple of people who helped me to not only survive but enjoy life as a Ph.D. student. If you don't find yourself in the acknowledgements, but think you should be mentioned, forgive me. You should probably be on that list. Just think of what Bilbo Baggins said: "I don't know half of you half as well as I should like; and I like less than half of you half as well as you deserve ".

Thank you, Olivier and Karen, for your great supervision and both scientific and personal advice. Both in Oslo, during field campaigns or in our weekly video conferences, I've always enjoyed our open, honest, and funny conversations. The mixture between scientific enthusiasm and a good understanding for all the other important and exciting things in life is not something all students get from their supervisors.

Octa and Juan, thank you so much for the incredible hospitality in Argentina, for all the great work we did in La Plata, El Manzano, Cara Cura, and during LASI, and for introducing me to the world of mate and Fernet! I'm already looking forward to seeing you again at some point, and hopefully we will have some Asado and watch Estudiantes play!

The colleagues at PGP/NJORD and friends in Oslo definitively deserve their own special thanks. After all, being a Ph.D. student (or human, for that matter) is not only about what you work on, but also who your colleagues and friends are. So, thank you for being there for short and long chats, fishing, camping, skiing, pub-quizzes, and evenings at all the craft-brew bars. Especially, I would like to thank my PGP office mates over the years: Frank, Øystein, Tobi, Håvard, and Thomas the Younger and Thomas the Elder. And Nanna, who has been the most fantastic flat mate and always kept the weirdo inside of me alive.

Thanks to my parents, who supported me in very different ways, be it to help me move, listen to my complaints, discussing science and, after all, spending your money on my education in probably the most expensive country in Europe.

And finally, a huge thanks goes to Kathi. You have been a great support in all situations. I'm very lucky to such a fantastic and relaxed person around me, and to just enjoy life with you!

Abstract

When magma intrudes organic-rich shale, the heat triggers contact-metamorphism, hydrocarbon generation and hydrothermal flow. Intrusions may also reconfigure basin-scale permeability distribution and thus impact long-term fluid migration. For both processes, fracturing in and around intrusions is a critical factor. However, our understanding of fracturing of igneous intrusions and the surrounding host rock is still limited. Therefore, this thesis investigates fracturing mechanisms and fracture network properties, as well as the effects of fracturing of intrusions on hydrothermal flow and geophysical properties.

To address these issues, I first present a geological field study of fracturing in outcropping sill intrusions in the Neuquén Basin, Argentina. The study identifies four main fracture types in the intrusions, including cooling joints, bitumen injection structures (dykes), hydrothermal calcite veins, and tectonic fractures. The bitumen occupying the fracture network is strongly graphitized, indicating a high-temperature environment. Fracture intensity, orientations, connectivity, and length vary considerably, and correlate with the distribution of the different fracture types.

The outcrop observations motivate a numerical study of hydrothermal flow in and around igneous sill intrusions, and compare impermeable vs. permeable (i.e., fractured) intrusions. Results show three distinct flow phases: (1) contact parallel flow below the sill and hydrothermal plume initiation before complete solidification. (2) “flushing” of hydrocarbon-rich fluids upward through the hot intrusion once it is solidified and permeable, which may explain graphitization. (3) partial backflow of hydrocarbons into the sill. This three-phase flow pattern strongly differs from hydrothermal flow around impermeable intrusions, which shows sustained contact-parallel flow below the sill and plume formation.

To improve the understanding of hydrocarbon expulsion and migration in heated shale, I then present a hydromechanical modeling study of fracture network evolving from initial microfractures. The results show that network evolution and fluid expulsion include three main phases. (1) initial growth of cracks with limited fracture opening and propagation angles aligning with far-field stresses. (2) fracture interaction and coalescence. (3) fluid expulsion, stress relaxation and closure of fractures. Highest network connectivity is achieved if far-field stresses are nearly isotropic and initial fractures are randomly oriented, or if mild stress anisotropy is combined with aligned initial fractures.

Finally, I present a workflow for realistic forward-modelling of intrusions based on cm-resolution 3D outcrop models and well data. The results illustrate that sub-seismic scale intrusion features may cause characteristic interference patterns in the seismic image that can be used as a signature to detect intruded intervals. In addition, variability of seismic properties of both intrusions and their host rocks can lead to very different seismic expressions of intrusions. Intrusions are very well imaged if acoustic impedance contrasts between intrusions and their host rocks are consistently large. However, reduced impedance contrasts can lead to poorly imaging. This is the case in the Neuquén Basin, where fractured

andesitic intrusions are emplaced in a succession with strong internal acoustic impedance contrasts, and intrusion are challenging to detect.

In conclusion, the fracture networks of shale-hosted intrusions can be substantially more variable than previously thought. The intrusions investigated in this study developed fracture networks and became accessible to hydrothermal fluids and hydrocarbons while they were still hot enough to cause graphitization. Numerical modeling supports this scenario, and shows that if intrusions become permeable upon solidification, hydrocarbon-rich fluids flow through the intrusion and may be exposed to temperatures of more than 400°C. This represents a valuable addition to our view on hydrothermal flow around intrusions since the igneous bodies are generally assumed to be impermeable.

For igneous petroleum systems, this means that migration into fractured igneous intrusions during their cooling phase may destroy locally generated hydrocarbons. However, the field data indicate that reservoir properties of intrusions locally benefit from additional fracturing through bitumen dykes or hydrothermal veins. For the igneous intrusions acting as reservoirs in the Neuquén Basin, this thesis provides additional data to improve reservoir models.

Lastly, the seismic modelling results expand our view on the range of seismic expressions of intrusions. The example of the Neuquén Basin demonstrates that seismic reflections from intrusions can vary between strong reflections to transparent, depending on fracturing, igneous rock type and host rock variability. Therefore, locally calibrated seismic forward modelling based on outcrop analogues can be of great value for seismic interpreters.

Graphical Abstract

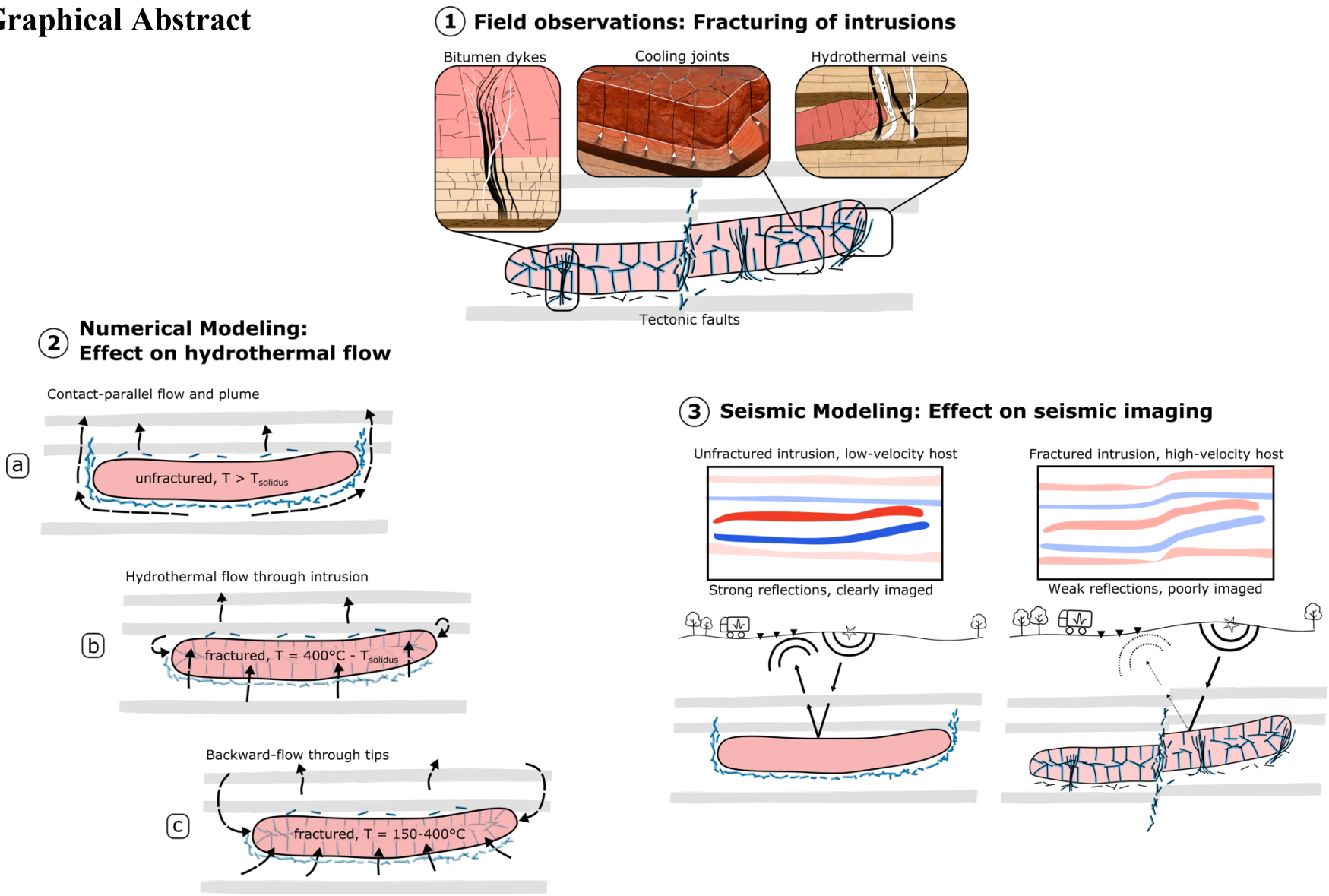

Table of Contents

1. Introduction and Aim

Magmatic activity is one of the most fascinating geological processes on Earth. While most people will think of magmatism mainly as volcanic eruptions, only a relatively small amount of magma reaches the surface. Most of the molten rock mass solidifies in the Earth's crust. When magma enters other rock formations such as sedimentary rocks and crystallizes in the subsurface, we define this as magmatic or igneous intrusions. Such igneous intrusions and their interactions with the surrounding sedimentary rock formations (termed "host rocks") are the central topic of this thesis.

Interactions between igneous intrusions and sedimentary rocks include coupled thermal, hydraulic, mechanical, and chemical processes (Aarnes et al., 2012; Iyer et al., 2017). Excluding the mechanical deformation resulting from the forceful emplacement of the intrusion, all processes are driven by the immense heat input that magma introduces into the geological system. The heat may, for instance, cause fast generation of liquid and gaseous hydrocarbons around igneous intrusions in organic-rich rocks like shale (Aarnes et al., 2010). If hydrocarbon gases are released into the atmosphere, they can cause global climate change and contribute to mass extinction events (e.g., Svensen et al., 2004; Aarnes et al., 2010). However, if the hydrocarbons remain underground, they can form economically relevant resources. As igneous intrusions cool down, they progressively solidify and often develop networks of cooling joints. If these joint networks remain open, they may provide pathways or storage space for the hydrocarbons, forming unconventional reservoirs (e.g., Senger et al., 2017; Witte et al., 2012).

This thesis aims to improve our understanding of fracturing in and around igneous intrusions and its link to magma-sediment interactions. It focuses on the setting of the Neuquén Basin, Argentina, where intrusions have generated hydrocarbons in the surrounding rocks and simultaneously act as fractured igneous reservoirs. The thesis combines three elements: field observations, numerical modelling, and seismic modelling.

The main foundation of any geological study are observations. The first element of this thesis is thus a detailed field study of fractured, shale-hosted intrusions in the Neuquén Basin, Argentina, to investigate and document fracture networks and intrusion-sediment interactions. The outcropping igneous sills in my study area constitute direct analogues to producing igneous reservoirs in nearby oil fields. Our understanding of the link between fracturing processes and fracture network properties in such intrusion reservoirs is still sparse, and conclusions on fracture network properties of igneous sill intrusions in general are conflicting (Senger et al., 2015; Witte et al., 2012). Therefore, the first aim of this thesis is as follows:

Identify fracture mechanisms and quantify their influence on fracture networks in igneous intrusions emplaced in organic-rich shale, focusing on intrusions that act as fractured hydrocarbon reservoirs.

The field observations provide insights to fracturing processes in and around igneous intrusions emplaced in organic-rich shale, but outcrops only offer the possibility to study the end-product of these processes. To investigate the dynamics of the involved physical and chemical processes around intrusions on different scales, numerical modeling techniques have been used extensively (e.g., Iyer et al. 2013; Iyer et al. 2017). However, the focus of previous numerical studies has neglected the impact of fracturing of the intrusions themselves. Thus, I combined outcrop observations with two numerical modeling studies to address the second aim of this thesis:

Investigate the influence of porosity and permeability generation in a cooling sill and its metamorphic aureole due to fracturing on local hydrothermal flow and hydrocarbon transport.

Finally, seismic data have been playing a critical role in understanding the emplacement and distribution of igneous intrusions and their effects on sedimentary basins (e.g., Planke et al. 2005; Schofield et al., 2015). Igneous intrusions (especially sills) are commonly described as easy targets for seismic interpreters, because large property contrasts between intrusions and their sedimentary host rocks are large, causing strong reflections. Nevertheless, several aspects such as limited resolution and interference of seismic reflections from thin sills pose significant challenges (Magee et al., 2015; Planke et al., 2015; Schofield et al., 2015). Additionally, the prevailing assumptions of high seismic property contrasts between igneous intrusions and their host rocks are based on specific settings of mafic intrusions emplaced in siliciclastic host rocks. This may not always be the case, because intrusions can be more silicic and/or fractured or emplaced in high-velocity host rocks like carbonates or evaporites. My study area in the Neuquén Basin represents such a case and is thus ideal to explore the range of seismic expressions of igneous intrusions. In this way, we can combine the geological understanding from outcrop and process modeling studies with geophysical exploration. The third goal of this thesis is therefore:

Develop an outcrop-based workflow to model realistic seismic images of igneous sill intrusions and use this workflow to understand how elastic property variations of sills and their host rock, for instance due to fracturing or varying lithology, change the seismic expression.

2. Scientific Background

2.1 Volcanic Basins

Volcanic basins are sedimentary basins that contain a significant amount of igneous rocks. Both extrusive volcanism and emplacement of igneous intrusions in the subsurface not only add new rock types to a sedimentary basin, but also influence its structural and thermal evolution (Galland et al., 2018; Svensen et al., 2004). Figure 1 illustrates important elements and processes typical for volcanic basins, such as surface features like volcanoes and the so-called ”magmatic plumbing system”, including subsurface sheet intrusions like horizontal or saucer-shaped sills and vertical dykes (Galland et al., 2018; Jerram and Bryan, 2017; Schofield et al., 2015). Note that although most of the thesis deals with sill intrusions, I will mostly use the more general term igneous intrusions. The findings will often be applicable not only to sills, but also dykes or other shallow intrusion types with slightly different geometries like laccoliths or inclined sheets.

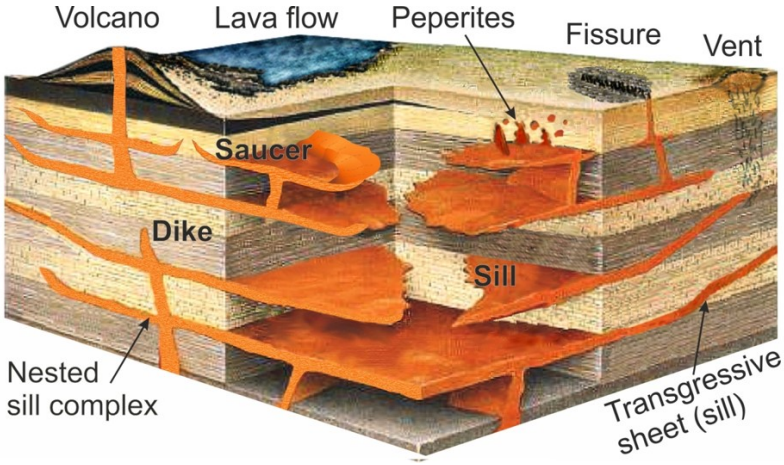

Figure 1. Schematic sketch of the main elements of a volcanic sedimentary basin (w. permission from Planke et al., 2018).

Volcanic basins with extensive sill complexes exist on all continents and are usually located along rifted and compressional continental margins (Figure 2), where sedimentary basins are abundant and magmatism or its remnants are concentrated (Senger et al., 2017). Some prominent examples of volcanic basins include the Karoo Basin in South Africa (Svensen et al., 2012), the Vøring-Møre and Faroe-Shetland Basins in the NE Atlantic (Bell and Butcher, 2002; Berndt et al., 2000; Planke et al., 2005; Schofield et al., 2015), the Siberian Tunguska Basin (Kontorovich et al., 1997) and the Neuquén Basin in Argentina (Kay et al., 2006; Spacapan et al., 2018). Intrusive complexes in such basins can cover enormous subsurface areas on the order of 10^4-10^6 km^2 and affect all stratigraphic levels and rock types present in a sedimentary basin (Magee et al., 2016; Spacapan et al., 2020a; Svensen et al., 2012).

The interactions between magma and sedimentary units have attracted the attention of scientists for many decades, especially due to hydrothermal flow triggered through igneous intrusions (Berndt et al., 2016; Delaney, 1982; Einsele et al., 1980; Jamtveit et al., 2004). Magmatic heat input initiates this hydrothermal flow, which can last 1000s to 100000s of years for a single intrusion or intrusive complex (Galerne and Hasenclever, 2019; Iyer et al.,

2013; Rodriguez Monreal et al., 2009). Active hydrothermal systems around intrusions evidence this link, for instance through the eruption of hydrothermal fluids at the surface such as the LUSI mud eruption (Mazzini et al., 2007) or on the seafloor (e.g., in the Guyamas Basin, Berndt et al., 2016; Einsele et al., 1980).

This type of magma-sediment interaction is relevant both from a research and economic perspective because hydrothermal activity due to sill intrusions may have caused global climate crises during the Earth's history (Aarnes et al., 2010; Iyer et al., 2017; Svensen et al., 2004), and also influences the generation of hydrocarbons (Delpino and Bermúdez, 2009; Schutter, 2003; Senger et al., 2017). Ancient, extinct hydrothermal vent complexes of enormous extent are documented for instance in the Vøring-Møre Basin and the Karoo Basins (Kjoberg et al., 2017; Planke et al., 2005). It is a widely accepted hypothesis that in these basins, intrusions have triggered the generation of greenhouse gases like CH_4 and CO_2 on the order of 10^3 gigatons, which were emitted into the atmosphere through many (in some cases thousands) of hydrothermal vents (Galerne and Hasenclever, 2019; Iyer et al., 2017; Svensen et al., 2004). Thermal input and hydrothermal flow may also generate and transport hydrocarbons in the subsurface and thereby affect petroleum systems (Delpino and Bermúdez, 2009; Senger et al., 2017). As indicated in Figure 2, we find such igneous petroleum systems affected by intrusions worldwide, for instance in the Neuquén Basin or the NE Atlantic (Schofield et al., 2015; Spacapan et al., 2020a). In addition, igneous intrusions affect local and basin-scale fluid flow long-term. After intrusions have cooled and solidified, they permanently alter the permeability structure of a volcanic basin and may represent everything between a highly efficient flow path to a regional barrier for fluid flow (Rateau et al., 2013; Senger et al., 2017). The following section will introduce the role of igneous intrusions in igneous petroleum systems in more depth.

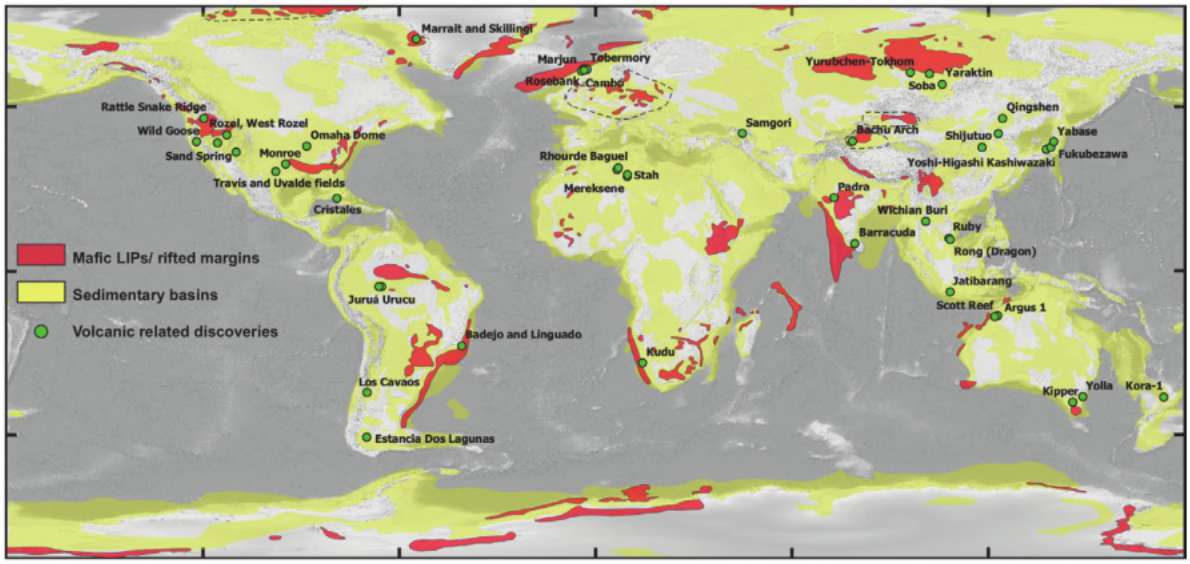

Figure 2. Global distribution of sedimentary basins and large igneous provinces (w. permission from Senger et al., 2017).

2.2 Effects of Igneous Intrusions on Petroleum Systems

When magmatism affects a petroleum system, we can define it as an igneous petroleum system. Igneous petroleum systems involving intrusions like sills, dykes or laccoliths exist in several volcanic basins globally (Senger et al., 2017). Intrusions may positively or negatively impact all elements of a petroleum system, which makes exploration and production in these systems challenging (Delpino and Bermúdez, 2009; Rohrman, 2007; Senger et al., 2017). To understand the effect of intrusions, it is important to define the main elements of a petroleum system which after Senger et al. (2017) comprise:

- *charge* (hydrocarbon generation from an organic-rich source rock)
- *migration* (flow of hydrocarbons from the source rock through the subsurface and towards the reservoir)
- *reservoir* (porous and permeable rock formation that allows storage of hydrocarbons)
- *trap* (a geological structure leading to accumulation)
- *seal* (impermeable formation preventing vertical or lateral discharge of the reservoir within the trap).

The following paragraphs will briefly summarize both positive and negative effects of intrusions on each of these elements known from various igneous petroleum systems worldwide and focus on those of relevance for this thesis. Figure 3 visualizes different potential impacts of intrusions and volcanism on an igneous petroleum system within a volcanic basin as presented by Planke et al. (2018).

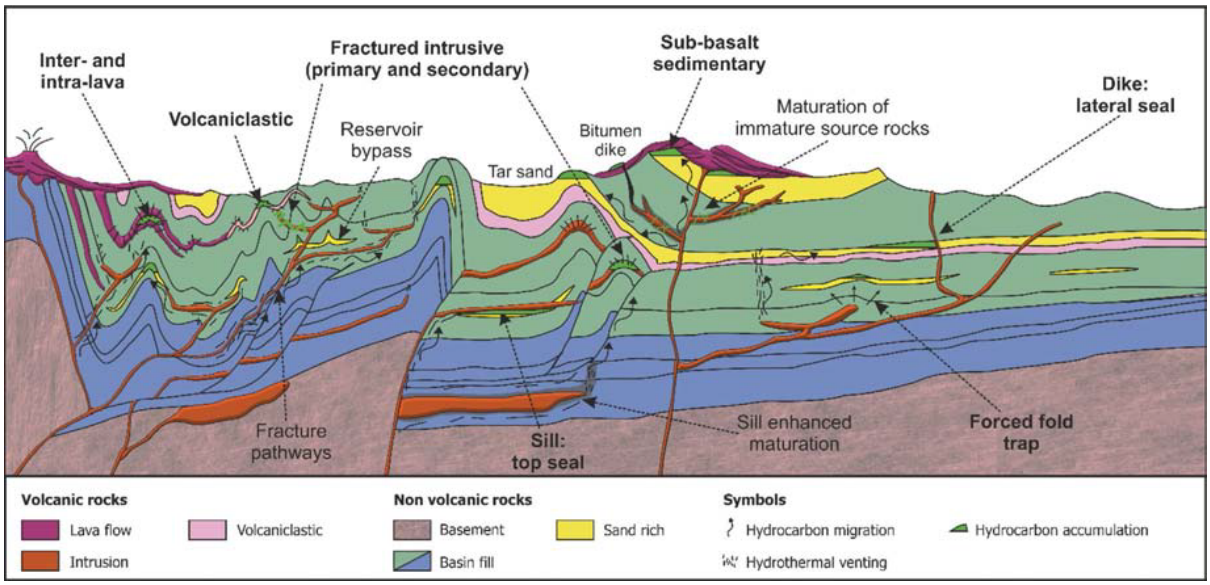

Figure 3. Synthesis of potential impacts of intrusions in igneous petroleum systems in a compressive margin setting (w. permission from Planke et al. 2018).

The main influence on the *charge* is the heat input provided by intrusions. In source rocks with low thermal maturity, the heat can generate a beneficial additional pulse of hydrocarbon generation (Spacapan et al., 2018). Such effects have been documented in parts of the

Neuquén and Parnaíba Basins in Argentina and Brazil, respectively (de Miranda et al., 2018; Rodriguez Monreal et al., 2009; Spacapan et al., 2018). In contrast, sediments can become overmature if magmatic intrusions lift the temperatures too much. This is the case in the innermost part of the host rock aureole close to the intrusion contact, where temperatures can reach 400-600°C for hundreds of years (Aarnes et al., 2010; Spacapan et al., 2018) and if intrusions enter source rocks at higher depth where background temperatures and maturity levels are high (Iyer et al., 2017; Sydnes et al., 2018). In addition to the expected correlation of intrusion thickness with the extent of the thermal aureole, clusters of stacked sills can significantly enhance maturity in the host rock layers due to superposition of the thermal effects of individual sills (Aarnes et al., 2011; Spacapan et al., 2018; Sydnes et al., 2018).

Intrusions affect hydrocarbon *migration* in several ways. While a newly emplaced intrusion cools down, its heat drives hydrothermal fluid flow and thus transport of hydrocarbons (Rodriguez Monreal et al., 2009). For instance, convection cells may initially transport hydrocarbons away from the intrusion and back towards it as it cools down (Rodriguez Monreal et al., 2009). Intrusions themselves can represent impermeable barriers for fluid flow, which can be both positive or negative, since hydrocarbons may either be redirected towards traps or away from them (Rateau et al., 2013). Fractured intrusions and fractured aureoles can also be preferred pathways rather than barriers, which can be an efficient mechanism to enhance vertical migration from lower levels (Rateau et al., 2013; Schofield et al., 2020; Senger et al., 2015). A basin may also inherit permeable structures like hydrothermal vents and breccia pipes from intrusions, which can serve as effective vertical fluid pathways (Hamilton and Minshell, 2019).

Fractured igneous intrusions can become excellent *reservoirs*. A network of cooling joints and possible tectonic fractures typically constitutes the main porosity of such unconventional reservoirs (Bermúdez and Delpino, 2008; Gudmundsson and Løtveit, 2014; Witte et al., 2012). For instance, fractured intrusions constitute the main reservoirs in currently exploited igneous petroleum systems of the Rio Grande Valley located in the Neuquén Basin (Spacapan et al., 2020a; Witte et al., 2012). Additionally, fracturing owing to fluid overpressure in the aureole during contact metamorphism can extend fractured sill reservoirs in shale formations (Spacapan et al., 2019). On the negative side, contact metamorphism around sills emplaced in sandstones may reduce reservoir porosity due to alteration or precipitation of minerals, and impermeable sills and dykes can compartmentalize conventional reservoirs, leading to challenges for hydrocarbon production (Jackson et al., 2020; Senger et al., 2017).

Intrusions can either form *traps* themselves or generate traps in the overburden. For instance, impermeable igneous sills and christmas tree laccoliths form traps in several oil and gas fields in Brazil and Thailand (de Miranda et al., 2018; Schutter, 2003). Elastic bending of the overburden can create so-called "forced fold", which then form four-way closures (Hansen and Cartwright, 2006; Jackson et al., 2020). Intrusion of magma into existing traps, however, can destroy them by generating escape routes for hydrocarbons (Senger et al., 2017).

Whether intrusions represent effective *seals* or not depends on their thickness, lateral continuity, and their bulk permeability properties (de Miranda et al., 2018; Senger et al., 2017). The latter depends to a large degree on the existence of an open fracture network. If fractures are absent, sills and dykes provide excellent top as well as lateral seals, while fractured intrusions can act as seal-bypass systems (Cartwright et al., 2007; Senger et al., 2015; Senger et al., 2017).

From the above it is clear that in addition to thermal maturation triggered by the magmatic heat input, fracturing plays a key role in determining the effect of igneous intrusions on petroleum systems. The significant uncertainty around this topic requires more systematic reserach on fracture systems in and around intrusions as well as the different processes of fracturing. This is one the central goals of this thesis.

2.3 Fracturing of Igneous Sill Intrusions

As described in the previous section, fractures are a critical part of the pore space within igneous intrusions, because they can add significant porosity and often control the bulk permeability of igneous intrusions.

First, let us define the possible elements of the pore space in igneous intrusions. For igneous rocks in general, we distinguish primary from secondary porosity (Petford, 2003; Zou, 2013). Table 1 summarizes this classification in an adapted version for igneous intrusions by Bermúdez and Delpino (2008). Primary porosity includes pore space formed during emplacement and the cooling and solidification of magma, i.e., cooling joints (columnar and intracolumnar), flow joints, intercrystalline and vesicular porosity. Secondary porosity comprises all elements of the pore space added through processes that alter the intrusion after its solidification, such as mineral alteration through hydrothermal fluids or tectonic joints and faults. Petford (2003) additionally subdivides primary porosity according to the rate of diffusive transport vs. transport by flow supported by the respective part of porosity. Primary pores like vesicles or intercrystalline pores are often isolated. Thus, intrusions typically require both cooling joints and other types of macro- or microfractures to enhance connectivity and develop significant porosity and permeability to allow efficient fluid flow or even storage (Bermúdez and Delpino, 2008; Jamtveit et al., 2014; Petford, 2003; Senger et al., 2015). However, minerals precipitation may seal the fractures fully or partially, which may limit fluid flow (Ogata et al., 2014; Senger et al., 2015).

Table 1. Porosity classification for igneous rocks edited after Bermudez and Delpino (2008) and Petford (2003).

Porosity Type	Primary	Secondary	Transport regime
Fractures	Columnar joints Intracolumnar joints Flow joints	Tectonic joints Faults and associated fractures Microfractures	Flow dominated (class F)
Cavities	Vesicles Intercrystalline voids Miaroles	Intercrystal and intracrystal voids (alteration, dissolution)	Diffusion dominated (class D)

We see from the porosity classification that fracture networks in intrusions may evolve in several stages related to different processes, which mainly include cooling joint formation during magma solidification and tectonic fracturing (Gudmundsson and Løtveit, 2014; Senger et al., 2017). This evolution depends on the involved fracturing processes, such as intrusion geometry, thickness, or fault proximity, why can lead to spatially heterogenous fracture networks (Galland et al., 2019; Senger et al., 2015; Witte et al., 2012). To understand fracturing of igneous intrusions and its influence on fluid transport properties, we therefore need to understand two aspects: (1) the physical mechanisms and characteristics of fracturing processes, especially cooling joints, and tectonic fractures and (2) how to quantify fracture network parameters and their link to bulk transport properties.

Cooling joints and tectonic fracturing in igneous intrusions

Cooling joints are the most common fracture type observed in igneous intrusions. Based on field observations, laboratory modelling with analogue materials and numerical calculations, it is now generally accepted that cooling joints form due to contraction of cooling magma (Goehring and Morris, 2008; Hetényi et al., 2012; Jaeger, 1961; Müller, 1998). As magma cools due to conductive heat loss to its host rock, its volume continuously decreases. When the magma reaches its solidus temperature, the contraction leads to the build-up of thermal stress which increase until the stress exceeds the tensile strength of the solidified igneous rock, resulting in fracturing (Hetényi et al., 2012). The fracture front thus follows a front of tensile stress that represents the level of thermal contraction, which usually also corresponds to a path perpendicular to the respective isotherm (Hetényi et al., 2012).

Cooling joints in intrusions grow orthogonal to the magma-host contact, i.e., vertical in the center and radially around bends or near the lava flow or intrusion tip (Galland et al., 2019; Kattenhorn and Schaefer, 2008). The joint surfaces are often randomly oriented and form columns ("columnar jointing"), which are famous for their often polygonal shapes (Goehring and Morris, 2005). However, cooling joints may also record far-field stresses during solidification by aligning with principal stress directions (Maher et al., 2020). Horizontal or oblique fractures are common where columns connect, which may lead to fracture zonation that is summarized in Figure 4 and explained below.

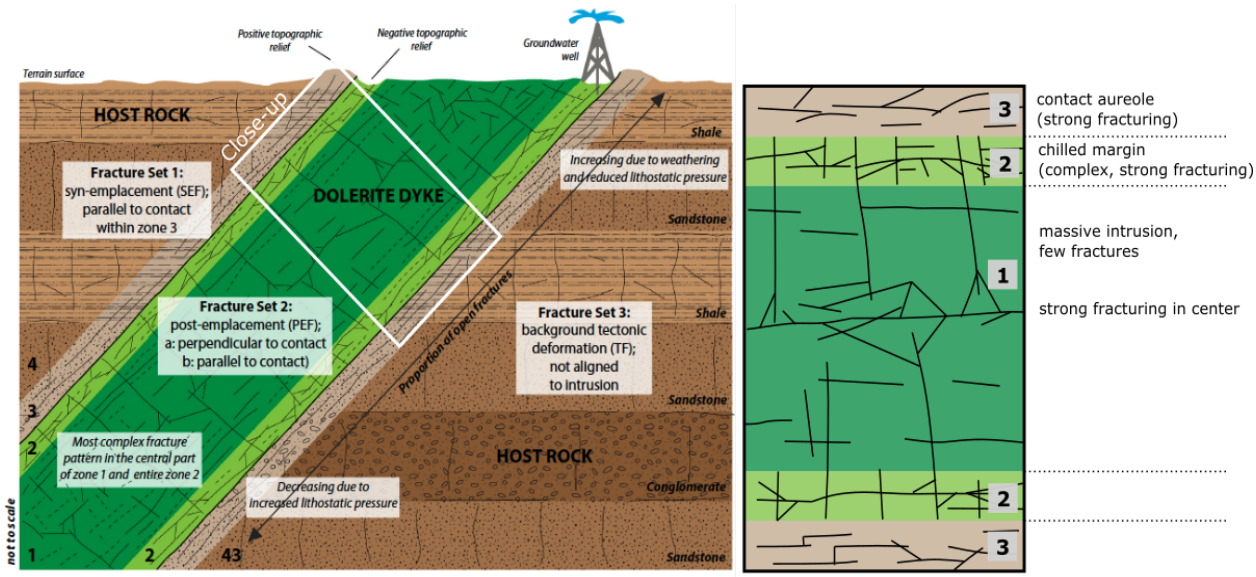

Figure 4. Model for joint zonation in igneous intrusions, modified w. permission from Senger et al. (2015).

Temperature gradients and thus cooling rates control joint scaling and spacing, where larger cooling rates cause smaller column diameters and thus spacing (Goehring et al., 2006; Müller, 1998). Since cooling rates are controlled by the boundary conditions, three important controls on joint scaling are (1) intrusion thickness, (2) intrusion geometry, (3) magma chemistry (i.e., initial magma temperature), and (4) emplacement depth, i.e., host rock temperature (Hetényi et al., 2012). Joint spacing and orientation commonly show a zonation

(Figure 4). Senger et al. (2015) describe intensely jointed zones near the contact ("chilled margins") and a generally less fractured intrusion interior but including a zone of complex fracturing near the center, where both cooling joint fronts meet ("entablature"). Bermúdez and Delpino (2008) document increasing cooling joint density towards the center, and a zone of cavities in the center due to late-stage volatiles. In summary, cooling joints in sheet intrusions are a common occurrence, but there is no consensus on their spatial distribution.

Igneous intrusions are concentrated along rifted and compressional tectonic margins, and therefore emplaced near potentially active faults. The interactions between magmatic and tectonic activity can encompass exploitation of pre-existing faults by intrusions (Galland et al., 2006; Galland et al., 2003; Galland et al., 2007; Magee et al., 2013), control of the tectonic stress regime on intrusion geometries (Galland et al., 2006; Menand, 2011), and tectonic jointing, deformation or even faulting of intrusions after their emplacement (Senger et al., 2015; Senger et al., 2017; Spacapan et al., 2020a; Witte et al., 2012). Some of these interactions are visualized in Figure 3. Tectonic joints and damage zones around faults that cross-cut intrusions can locally or regionally increase fracture density and connectivity, improving permeability in igneous intrusions (McCaffrey et al., 2003; Senger et al., 2015; Senger et al., 2017; Sidney and Clapp, 1932; Witte et al., 2012). In addition, pre-existing fractures like cooling joints may be reactivated and reopened by tectonic processes, providing additional effective fracture porosity (Spacapan et al., 2020a; Witte et al., 2012).

Quantification of fracture networks

Quantitative fracture network characterisation is critical to decipher fracture evolution, provide scaling relationships, and model fractured reservoirs (Bonnet et al., 2001; Zeeb et al., 2013). Sampling along 1D profiles ("scanlines"), in 2D windows, or circular scanlines provides important fracture network parameters including distributions of orientation, density or intensity, length, aperture, and connectivity (Healy et al., 2017; Zeeb et al., 2013). In studies of fractured reservoirs, these values are usually obtained either from boreholes that yield in-situ 1D data, or analogue outcrops that allow 2D/3D data collection but may not perfectly represent subsurface conditions (Casini et al., 2016; Zeeb et al., 2013). The collected parameters are then typically used to estimate fracture porosity and permeability, and to create discrete fracture networks (DFNs) for reservoir modeling (Casini et al., 2016).

While this procedure is standard to describe fracture networks in sedimentary rocks, fracture networks of igneous intrusions are not nearly as well described or understood. To the best of my knowledge, only a handful of studies exist that quantify fracturing in igneous intrusions (Festøy, 2017; McCaffrey et al., 2003; Senger et al., 2015; Witte et al., 2012). The reported observations vary substantially. Fracture networks may be very heterogenous in terms of fracture orientation and density both between different study sites and within single outcrops, which is related to a combination of emplacement-related cooling joints and tectonic fractures (Senger et al., 2015). On the other hand, the fracture network parameters of a mixture of cooling and tectonic joints can also be laterally consistent and their scaling may follow power-law relationships (McCaffrey et al., 2003; Witte et al., 2012).

2.4 Magma-sediment interaction: Thermo-hydro-mechanical-chemical (THMC) processes

In addition to the processes inside a cooling intrusion, the host rock aureole experiences temperature-driven contact metamorphism and hydrothermal flow (Aarnes et al., 2010; Delaney, 1982; Einsele et al., 1980; Svensen et al., 2004). In this thesis, I focus on settings where the host rock is organic-rich shale, although many processes are generally valid for sedimentary rocks intruded by magma. Magmatic heating of shale leads to coupled thermo-hydro-mechanical-chemical (THMC) processes with important consequences for volcanic sedimentary basins (section 2.1) and igneous petroleum systems (section 2.2). Figure 5 illustrates the THMC processes, which mainly comprise thermally driven fluid generation leading to fluid overpressure and fracturing. Our understanding of the THMC processes relies greatly on field, laboratory and numerical modeling studies at different scales, which I will summarize in this section. I will begin with temperature-driven metamorphic chemical reactions, then outline the impact of these reactions and general heating on the pore fluid pressure and fluid flow, and finally discuss the resulting mechanical processes in the host rock, i.e., fracturing.

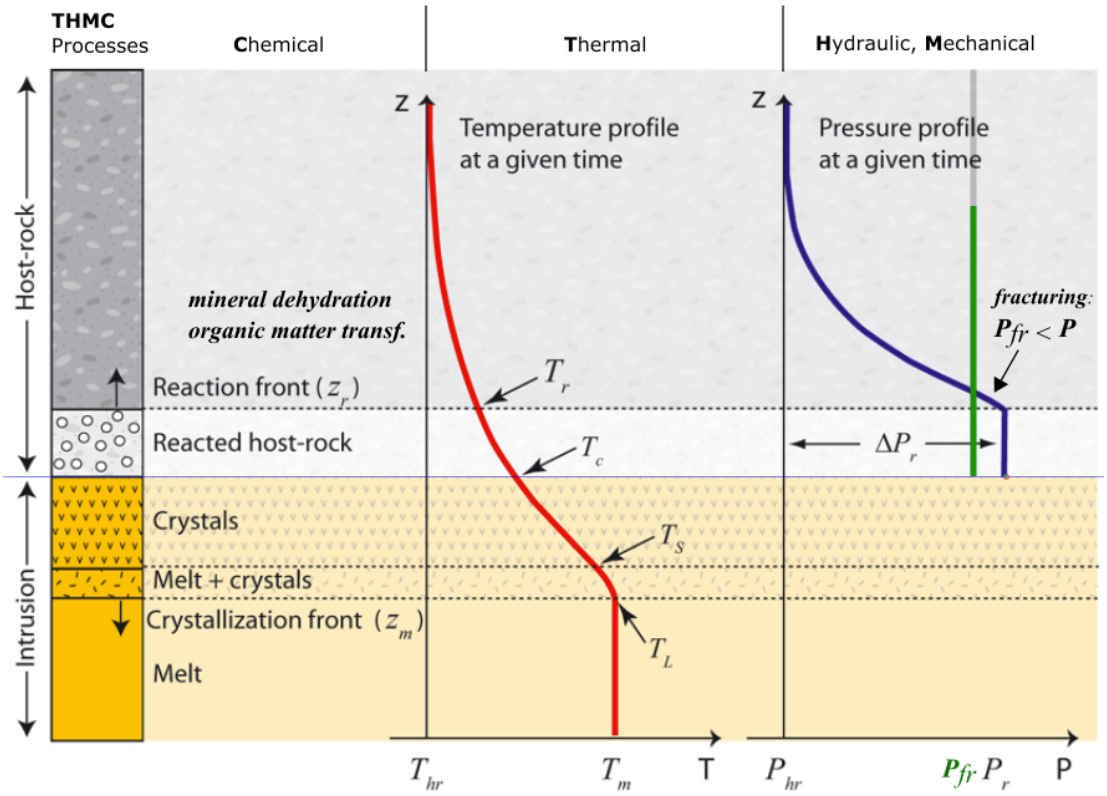

Figure 5. Illustration of coupled thermo-hydro-mechanical-chemical (THMC) processes in shale: a thermally driven reaction front leads to rapid fluid or gas generation in the host rock aureole. This results in strong overpressure which may eventually cause fracturing if fluid pressure exceeds the fracture pressure.
T_L = liquidus temp., T_S = solidus temp., T_C = contact temp., T_r = temp. at reaction front, T_{hr} = host rock background temp., P_r = fluid pressure in reacted host, P_{fr} = fracture pressure, P_{hr} = background fluid pressure in host rock (edited w. permission from Aarnes et al., 2012).

Chemical reactions

The two most important metamorphic reactions in strongly heated shale include (1) dehydration of minerals containing bound water and (2) transformation of solid organic material into hydrocarbons, which are primarily (exponential) functions of time and temperature (Aarnes et al., 2010). There is a long record of documented chemical alterations in the thermal aureoles, especially when it comes to enhanced maturation of organic matter and associated hydrocarbon production (Aarnes et al., 2015; Muirhead et al., 2017; Sidney and Clapp, 1932; Simoneit et al., 1978; Spacapan et al., 2018). While the conversion may take millions of years under shallow burial conditions, these reactions may be completed within years, months, days in the thermal aureole of igneous intrusions, where temperatures can reach values of 300-600°C (Aarnes et al., 2010; Panahi et al., 2018; Pytte and Reynolds, 1989; Spacapan et al., 2018).

Unaltered clay minerals contain bound water which is released into the pore space as clay minerals transform under elevated temperatures. Probably the most important example is the illite-smectite transition which happens between 70-250°C under burial conditions. This corresponds to similar temperature range as oil and gas generation in hydrocarbon source rocks (Pytte and Reynolds, 1989). At higher temperatures of 200-400 °C, also other silicate and carbonate minerals may dehydrate (Panahi et al., 2018). The stable mineral assemblage for sediments of varying initial compositions can be calculated as a function of temperature based on thermodynamic considerations, which yields the amount of water released into the pore space during contact metamorphism (Aarnes et al., 2010; Connolly, 2009).

Organic matter transformation into hydrocarbons is the second important reaction in the metamorphic aureole. It includes the conversion of solid matter into liquid or gas, which are released into the pore space. Typical parameters to describe and quantify the degree of thermal maturity are the reflectance of vitrinite particles *Ro* under the microscope (Price, 1983), or Pyrolysis parameters such as hydrogen index, transformation ratio, and total organic carbon (TOC) in the host rock (Espitalié et al., 1985). These methods were originally developed to analyze petroleum source rocks in general but have been widely adopted to characterize thermal effects of igneous intrusions, both in field and modeling studies (e.g., Aarnes et al., 2010; Iyer et al., 2013; Iyer et al., 2018).

The strongly increased temperatures usually lead to a typical aureole of high thermal maturity around igneous intrusion emplaced in organic-rich shale, which may have a width of 30-250% of the respective sill thickness (Aarnes et al., 2010). Documenting this aureole using vitrinite reflectance or transformation ratio of organic matter represents a crucial task for any geological study of contact metamorphism around sills because it constrains the extent of the thermal impact and background maturity in the sedimentary host rock (Aarnes et al., 2015; Muirhead et al., 2017; Simoneit et al., 1978; Spacapan et al., 2018). The inner aureole close to the intrusion usually shows full transformation and thermal overmaturity, while the outer aureole typically reflects thermal maturity corresponding to the gas or oil windows.

Hydro-mechanical processes and host rock fracturing

The sudden addition of fluids or gases to the pore space and the thermal expansion of pore fluids generate strong fluid overpressure (Aarnes et al., 2012; Delaney, 1982; Townsend, 2018). If the rate of overpressure generation exceeds pressure dissipation through flow, the consequence is the formation of hydrofractures that open fluid pathways and additional pore space (Aarnes et al., 2012; Jamtveit et al., 2004). Key evidence for this process is the general observation from field and seismic studies that the density of tensile fractures increases towards the intrusion contact as well as the observation of breccia pipes and hydrothermal vents originating from igneous intrusions (Aarnes et al., 2012; Jamtveit et al., 2004; Senger et al., 2015; Spacapan et al., 2019; Zhang et al., 2017).

Laboratory and numerical modeling studies significantly improved our understanding of the dynamics of dehydration and organic matter transformation in shale, and their coupling to hydrofracturing and fluid release. The coupled processes involve three stages including (1) fracture initiation in response to overpressure, (2) fracture propagation and coalescence and (3) fluid expulsion and closure of fractures (Kobchenko et al., 2014; Panahi et al., 2018; Panahi et al., 2019). Experiments involving heating of immature shale over several hours to days showed that microfracture formation around ellipsoidal kerogen patches starts at around 300-350°C (Kobchenko et al., 2011; Panahi et al., 2018; Teixeira et al., 2017). The fluid generation leads to a periodic process, where fractures open due to overpressure accumulation, allowing expulsion and subsequent closing of fractures (Panahi et al., 2019). Figure 6 illustrates the fracture network of heated shale samples with clearly visible oil stains due to expulsion along the fractures.

Interestingly, all the above studies intended to model hydrocarbon generation under burial conditions. However, due to the necessity to speed up the process to an observable time scale, the temperature conditions in the shale experiments (300-750°C) are very well suited to apply the results to magma-shale interactions.

The experimental results also help to validate numerical models of the coupled THMC processes, which are currently mainly modeled as hydromechanical (HM) processes and only implicitly include chemical and thermal effects. Both experimental and numerical results indicate that the layered nature of shale as well as the stress regime control the propagation of fractures and formation of a percolating network (Chauve et al., 2020; Panahi et al., 2018; Teixeira et al., 2017). Under isotropic stresses, the hydraulic fractures tend to exploit the mechanical weakness along shale layers and propagate layer-parallel, i.e., horizontally (Chauve et al., 2020; Teixeira et al., 2017). Therefore, the presence of a differential stress with the largest stress being vertical is likely an important factor, since tensile hydraulic fracture propagate in the direction of this stress (Teixeira et al., 2017). Despite recent progress in numerical modeling, it remains challenging to quantify the effect of fracturing on the hydraulic properties of the shale. The available modeling studies did not yet explore the continuous evolution of fracture networks in terms of fracture network parameters, or the cyclic fracturing and expulsion process observed in experiments.

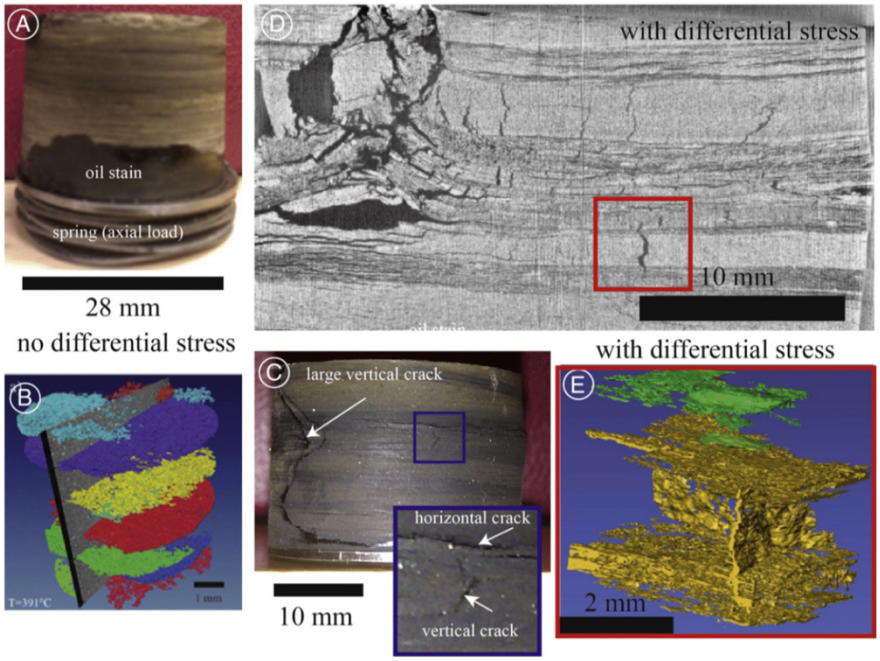

Figure 6. Fracturing in a laboratory sample of strongly heated, initially immature shale, showing how fast hydrocarbon generation may lead to the creation fracture networks. (A) sample with oil stains after heating, (B) horizontal fracture surfaces from microtomography after experiment without differential stress, (C-D) visible networks of horizontal and vertical microcracks in sample heated under differential stress (w. permission from Teixeira et al., 2017).

Large-scale models of THMC processes on volcanic basins

The described coupled THMC processes strongly impact hydrothermal fluid flow and hydrocarbon migration around intrusions emplaced in organic-rich rock units within volcanic sedimentary basins. Therefore, these processes need to be considered for models of hydrothermal flow on the scale of intrusions or even whole volcanic basins. The most common approach includes the application of the finite element method (FEM), which is used to model 1D or 2D thermal evolution, associated transformation reactions and/or fluid flow of sills and the surrounding host rock in volcanic sedimentary basins (Aarnes et al., 2010; Galerne and Hasenclever, 2019; Iyer et al., 2013; Iyer et al., 2017; Iyer et al., 2018; Rodriguez Monreal et al., 2009; Svensen et al., 2010).

For instance, the formation of hydrothermal vents and release of the generated hydrocarbons depend on the THMC processes and has been thoroughly investigated using FEM modeling (Galerne and Hasenclever, 2019; Iyer et al., 2013; Iyer et al., 2017). The combination of fluid generation and low permeability leads to progressive hydraulic fracturing and flow-focusing along the intrusions toward their tips, where breccia pipes and hydraulic vents form only some decades after emplacement (Aarnes et al., 2012; Galerne and Hasenclever, 2019; Iyer et al., 2013; Iyer et al., 2017). Aarnes et al. (2012) and Jamtveit et al. (2004) formulated limiting conditions based on emplacement depth (i.e., lithostatic pressure to overcome for fracturing), permeability and total organic carbon (TOC) content that create conditions that favour fracturing and vent formation, which then control upward flow of hydrothermal fluids and hydrocarbons.

Moreover, hydrothermally driven migration of hydrocarbons generated close to intrusions has been proposed as an important mechanism in igneous petroleum systems (Rodriguez Monreal et al., 2009; Spacapan et al., 2018; Witte et al., 2012). Understanding and evaluating this mechanism in petroleum system modeling relies on a correct implementation of THMC processes, because they change the porosity-permeability distribution in the affected rocks over time, e.g., due to fracturing. However, most petroleum-related thermal modeling studies involving sills do not consider thermal effects and fluid flow as coupled THMC problems. Instead, the thermal effect on shales, i.e., additional maturation, is normally treated as a simple conductive problem separate from later fluid migration (Spacapan et al., 2018; Spacapan et al., 2020b; Sydnes et al., 2018). To my knowledge, only Rodriguez Monreal et al. (2009) attempted to include hydrothermal transport in their analysis of the effect of laccolith emplacement within organic-rich shale, but they did not account for fracturing. Thus, there is a need to investigate the effects of intrusions on igneous petroleum systems with a model including coupled THMC processes.

2.5 Geophysical Exploration of Igneous Intrusions

In addition to geological fieldwork, seismic reflection data have been playing a key role in the study of volcanic sedimentary basins. In fact, much of the evidence for the importance of the processes discussed in the previous chapters, such as hydrothermal vent formation, originally stems from seismic data (Jamtveit et al., 2004; Svensen et al., 2004). Igneous intrusions are usually characterised by high seismic velocities and high densities, giving them a much higher acoustic impedance than many of their sedimentary host rocks (Planke et al., 2015). This situation is to a large degree responsible for the success of seismic imaging of intrusions, because the large impedance contrasts generate bright reflections and make intrusions relatively easy targets for interpretation (Magee et al., 2018; Planke et al., 2015). Figure 7 shows a seismic image from offshore Norway, illustrating a typical example of a clearly imaged igneous sill complex.

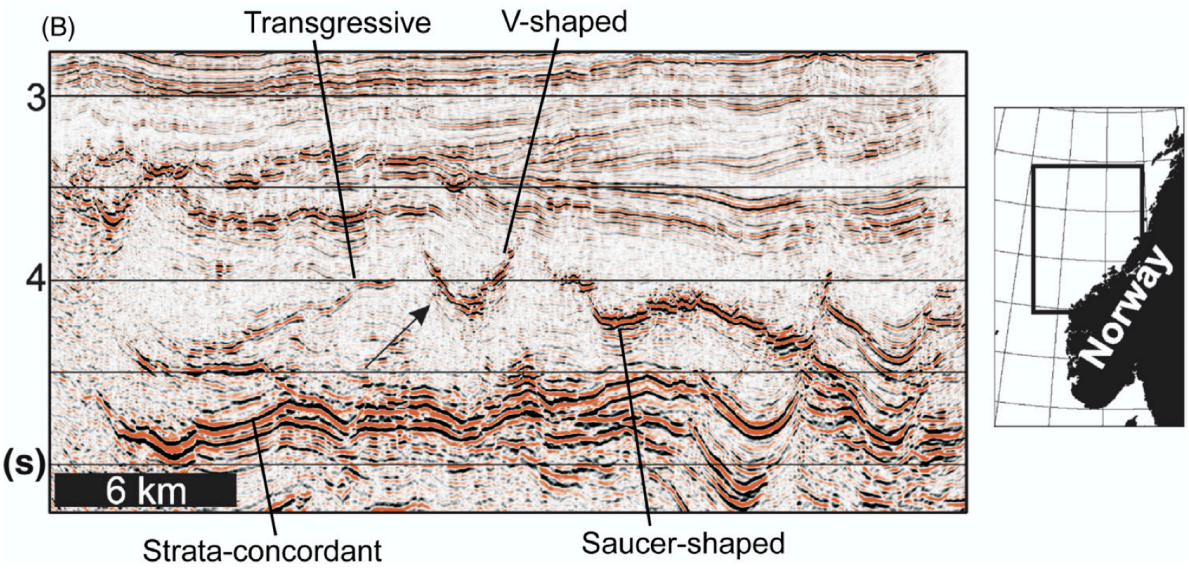

Figure 7. Example of a sill complex imaged by a seismic reflection survey, illustrating the typical strong reflections and different sill geometries (w. permission from Galland et al. 2018).

Seismic properties of igneous intrusions

Two main factors control the seismic properties of crystalline igneous rocks such as intrusions or lava flows: (1) primary and secondary mineral composition, and (2) porosity and fracturing (Berge et al., 1992; Mark et al., 2018; Planke et al., 2015; Smallwood and Maresh, 2002). Table 2 contains ranges for P-wave velocities and densities for intrusions of varying composition taken from selected studies, and put them into perspective with the range of velocities for possible sedimentary host rocks.

P-wave velocity data from mafic intrusions like dolerites are very well documented, for example from borehole data and seismic refraction surveys along the rifted margin of the NE Atlantic. Reported values vary significantly and lie between 4.5 - 7.4 km/s (Berndt et al., 2000; Planke et al., 2015; Smallwood and Maresh, 2002). However, average values of 5.5-6 km/s are usually assumed, which combined with an average density of around 3000 kg/m^3

make mafic intrusions bodies of very high acoustic impedance (Berndt et al., 2000; Planke et al., 2015; Smallwood and Maresh, 2002). S-wave velocities are less available, but range between 2.2-3.8 km/s, leading to V_P/V_S ratios around 1.8-2.0 in massive basaltic rocks (Berndt et al., 2000; Klarner and Klarner, 2012; Planke et al., 2015; Smallwood and Maresh, 2002).

However, more silicic and/or hydrothermally altered igneous intrusions often show much smaller seismic velocities (Mark et al., 2018; Mordensky et al., 2018). V_P and V_S in this case are closer to that of many sedimentary rocks (cf. Table 2). This means that depending on the specific composition of intrusions and their host rocks, seismic property contrasts might be relatively small, leading to rather dim reflections more challenges for seismic interpretation. For instance, Mark et al. (2018) reported several silicic and altered intrusions that appeared as intermediate-amplitude reflections in seismic reflection data, and were erroneously interpreted as hydrocarbon-bearing sandstones. Moreover, the data presented in Table 2 show that some sedimentary rocks, including highly cemented sandstones, carbonates and evoparites may even exhibit V_P values comparable to relatively high-velocity igneous rocks.

Table 2. Summary of typical compressional wave velocities of igneous intrusions and their sedimentary host rocks. References: B = Berndt et al. (2000), K = Kearey et al. (2002), Ma = Mark et al. (2018), Mo = Mordensky et al. (2018), Sc = Schön (2015), Sm = Smallwood & Maresh (2002)

Rock type	P-wave velocity [km/s]
Mafic intrusions (dolerite)	4.5-7.4[Sm, B]
Felsic (granite, dacite) / altered intrusions	3.3-5.85[Ma, Mo, Sc]
Siliciclastics (Sandstone/Claystone)	2.0-6.0[K, Sc]
Carbonates	3.0-6.5[K]
Evaporites (Salt, Anhydrite)	4.5-6.5[K]

Benefits and challenges of seismic imaging and interpretation of igneous intrusions

Seismic reflection data have many advantages over other geophysical methods in the imaging of igneous intrusions. High-quality 2D and 3D seismic data from hydrocarbon exploration are readily available from industry collaboration or even open data bases in many countries worldwide. This is reflected by the global distribution of seismic studies of igneous intrusive complexes, which have been conducted in many countries with prolific hydrocarbon provinces such as Norway (Berndt et al., 2000; Kjoberg et al., 2017; Planke et al., 2005; Schmiedel et al., 2017), the UK (Mark et al., 2018; Schofield et al., 2015), New Zealand (Bischoff et al., 2017; Infante-Paez and Marfurt, 2017), Australia (Jackson et al., 2013; Magee et al., 2015a; Magee et al., 2017) and China (Sun et al., 2014).

Seismic data reach vertical resolutions of meters to tens of metres in shallow crustal depths relevant for volcanic sedimentary basins, which greatly exceeds the resolution of other geophysical imaging methods like controlled-source electromagnetic (CSEM), magneto-telluric (MT), magnetic or gravimetric surveying (Magee et al., 2018; Planke et al., 2015).

Specifically, for a typical sill of 5500 km/s velocity and a signal frequency 13-45 Hz, sills down to 105-30 m thickness would be resolvable, i.e., with top and bottom contact imaged as separate reflections (cf. Figure 8). For most cases the resolution limit, which is approximated as a quarter wavelength, lies somewhere between these values (Magee et al., 2015b). The detectability limit is even smaller, such that under optimal conditions, even sills of just a few meters thickness can theoretically be visible (Eide et al., 2017; Magee et al., 2015b; Planke et al., 2015).

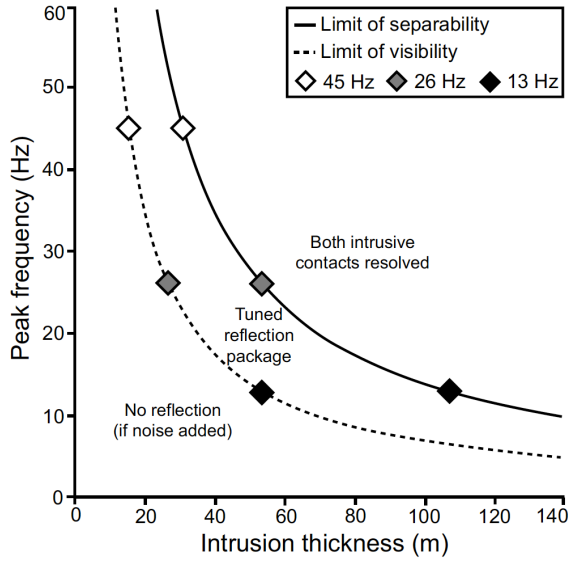

Figure 8. Resolution (separability) and detection (visibility) limits for typical dolerite sills (Vp = 5500 m/s) imaged at different peak signal frequencies presented by Magee et al. (2015). Reprinted w. permission.

This makes it possible to image large complexes of layered intrusions like sills, and assess basin-scale magma transport on the basis of lateral intrusion extent and connectivity, as well as detailed intra-intrusion structures like lobes and magma fingers that can serve as magma flow indicators (Magee et al., 2016; Schofield et al., 2012; Schofield et al., 2015). Sills can appear as laterally discontinuous reflections that may be layer-parallel, saucer-shaped, transgressive (i.e., climbing up or down through stratigraphic levels) or follow pre-existing faults (Planke et al., 2005). These «seismic sill facies» units were developed from seismic datasets (e.g., Figure 7) but correspond well to field observations from exposed igneous sills (Eide et al., 2016; Galland et al., 2019; Magee et al., 2015b; Schofield et al., 2012; Schofield et al., 2010).

Despite the many benefits, several challenges remain for seismic interpretation of intrusive complexes. Especially in areas with insufficient knowledge on the possible subsurface lithology, igneous intrusions can be confused with geological bodies with similar seismic properties, like carbonate build-ups or gas-charged sandstones (Infante-Paez and Marfurt, 2018; Klarner and Klarner, 2012; Mark et al., 2018). Additionally, seismic reflections from thin and stacked intrusions can cause tuning and interference effects which make thickness estimates and identification of single sills challenging or impossible in some cases, especially where splitting and merging of several intrusions occurs (Eide et al., 2017; Planke et al.,

2015; Schofield et al., 2015). Finally, high-angle inclined sheets and dykes are difficult to image directly since the reflected waves from interfaces with high angles to the horizontal do not reach the receivers (Planke et al., 2015).

Seismic forward modelling of igneous intrusions

Seismic forward modelling represents an important tool to meet some of these challenges and improve confidence in interpretations of intrusions. In most cases, this forward modeling is done via convolution. A geological model with seismic properties allocated to intrusion and host rock results in a seismic reflectivity model, which is then convolved with a source function (wavelet) representing the seismic signal to give a synthetic seismic image (Lecomte et al., 2016; Magee et al., 2015b). Whether the synthetic seismic image is a realistic representation of a real image depends on the important factors including the geometrical complexity of the target, illumination, vertical and lateral resolution and seismic survey geometry (Lecomte et al., 2015; Lecomte et al., 2016). Recently developed space-domain 2D/3D convolution technology offers similar speed and ease of use as the “classic” time-domain 1D convolution but produces much more realistic results, because it considers the factors mentioned above (Lecomte et al., 2015; Lecomte et al., 2016).

Simple geometries such as wedges, bars, "stair-like" steps help to assess tuning and interference behaviour of igneous intrusions, for instance as a function of seismic velocity, signal frequency or source-receiver offsets (Magee et al., 2015b; Planke et al., 2005). These idealised shapes may even give initial hints at more complex interference behaviour, for example due to interaction of a sill intrusion with surrounding sediments or other igneous bodies (Magee et al., 2015b).

However, since detectability limits are in the range of meters for many igneous intrusions, more detailed and realistic model representations of intrusions based on field analogues add further insight. The basis of such field-based, realistic intrusion shapes for seismic modeling are usually 3D digital outcrop models created from remote sensing data, e.g., LiDAR, or structure-from-motion photogrammetry. The results of such field-based modeling is particularly useful to constrain the seismic response in specific geological settings analogous to those studied at high detail in the outcrops (Anell et al., 2016; Eide et al., 2017).

3. Geological Setting – The northern Neuquén Basin, Argentina

This thesis makes extensive use of field observations from the northern Neuquén Basin, Argentina. In this volcanic sedimentary basin, it is possible to collect and combine geological and geophysical data from fieldwork and subsurface. As illustrated in Figure 9, commercial hydrocarbon production of igneous petroleum systems has generated large datasets from wells and seismic exploration, and the neighboring fold-thrust belts offer spectacular outcrops of direct analogue systems (Spacapan et al., 2020a; Witte et al., 2012). Our study area comprises the Río Grande Valley and Sierra Azul mountain range in the southern Mendoza province, ca. 70 km south of the town Malargüe (Figure 9a). In the following, I will briefly summarize the geological history of the northern Neuquén Basin and the current understanding of the igneous petroleum systems of Río Grande Valley.

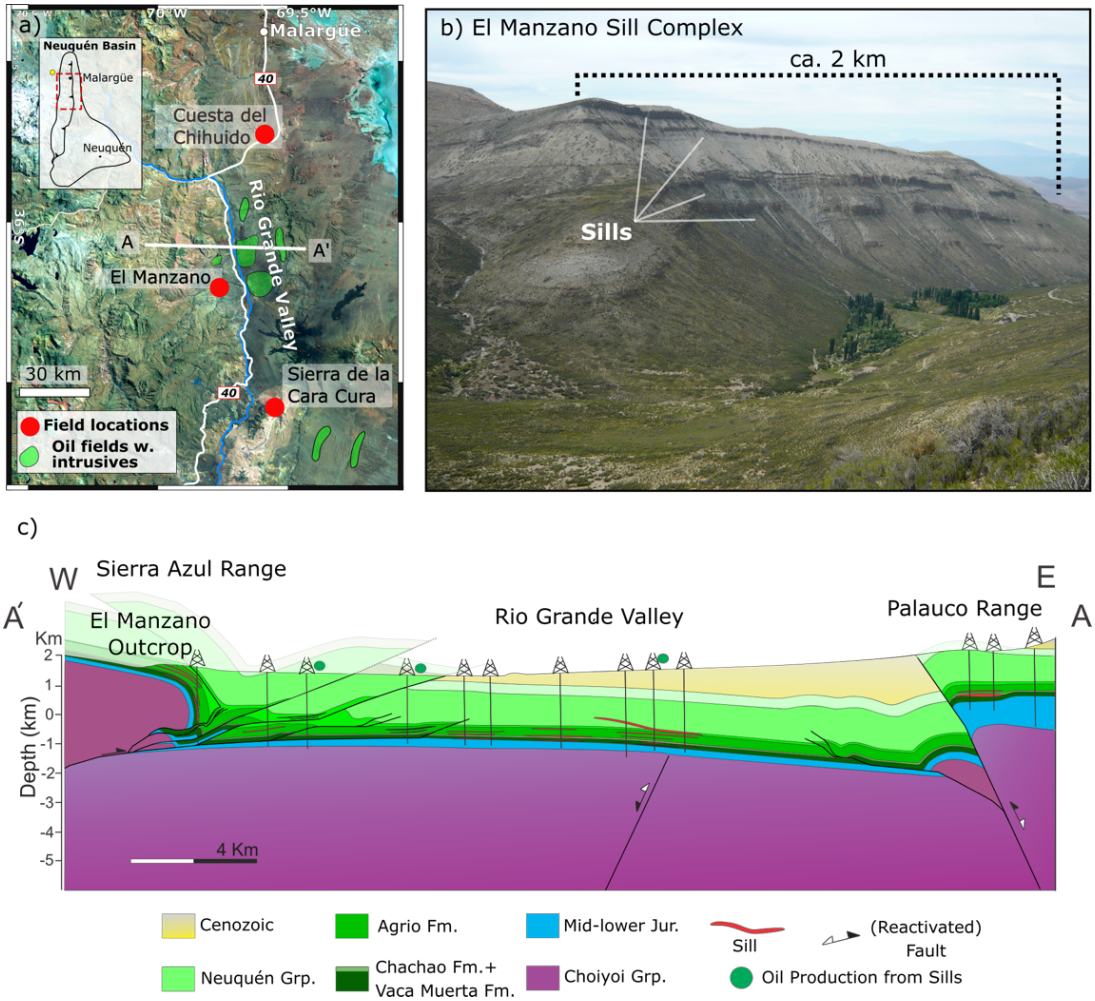

Figure 9. (a) Satellite imagery of the study area around the Río Grande Valley, indicating oil fields and outcrop localities. (b) Panorama of the spectacular outcrop at El Manzano in the Sierra Azul range, which features a km-scale sill complex emplaced in organic-rich shale formations. (c) Structural section through Rio Grande Valley and Sierra Azul, showing the analogy between subsurface sills and outcrops. Figure from Rabbel et al. (in prep., this thesis).

3.1 Basin History and Volcanism

The Neuquén Basin represents a volcanic sedimentary basin in compressive tectonic setting. It developed in three main phases, including (1) an initial rift phase, (2) a phase of thermal subsidence, and (3) foreland basin phase (Howell et al., 2005). During the rift phase (late Triassic-early Jurassic), several isolated halfgrabens developed, resulting in continental and volcaniclastic synrift deposits. As extension ceased, continued thermal subsidence and a shift to a marine environment (early Jurassic-early Cretaceous) lead to a connection of the depocenters and deposition of a thick succession of marine sediments. This part of the succession contains sedimentary rocks of all kinds, including siliciclastics, carbonates and evaporites. For this thesis the Mendoza Group (late Jurassic-early Cretaceous) is the most important one, because it contains the organic-rich Vaca Muerta and Agrío shale formations that represent the main source rocks of the igneous petroleum systems investigated in this work (Howell et al., 2005; Spacapan et al., 2020a). Massive carbonates (Chachao Fm.) locally separate these two shale formations, which are overlain by the evaporitic Huitrín Fm. From the late Cretaceous and onwards, Andean compression controlled the development of the Neuquén Basin, which now represents a foreland basin. Reactivation of the Triassic normal faults created several fold-thrust belts along the western basin margin, which also comprise the Sierra Azul range (Manceda and Figueroa, 1995). The proposed onset of uplift in the Sierra Azul varies between late Cretaceous and middle Miocene (Folguera et al., 2015; Silvestro and Atencio, 2009).

Contemporaneous to tectonic uplift, the northern Neuquén Basin including Sierra Azul and Río Grande Valley experienced extensive volcanism (Combina and Nullo, 2011; Kay et al., 2006). This caused the emplacement of thick lava flows as well as subvolcanic intrusive complexes, which include networks of predominantly andesitic to basaltic sills, but also dacitic dykes and laccoliths (Rodriguez Monreal et al., 2009; Schiuma, 1994). Spacapan et al. (2019) mapped the Río Grande Valley sill complexes and found that they extend over more than 100 km^2. The volcanism in the study area occurred in two main episodes in the late Oligocene, Miocene and Pliocene termed the Molle and Huincán Eruptive Cycles (Combina and Nullo, 2011; Witte et al., 2012). Although nearly all sedimentary formations host intrusions, they are preferentially emplaced as sills in the organic-rich Agrío and Vaca Muerta formations, which host the igneous petroleum systems (Rodriguez Monreal et al., 2009; Schiuma, 1994; Spacapan et al., 2020a). Magmatic heat input has also been suggested as an important factor in the formation of bitumen dykes, which are common around volcanic centers in the Neuquén Basin and have been mined since the early 20^{th} century (Cobbold et al., 2014; Rassmuss, 1923; Zanella et al., 2015).

3.2 Igneous Petroleum Systems of Río Grande Valley

The igneous petroleum systems of the Río Grande Valley area include several commercially producing oil fields with up to 25 million barrels of recoverable oil per field (Witte et al., 2012). The reservoirs in these fields are fractured igneous sills emplaced mainly in the Vaca Muerta and Agrío formations and were discovered nearly 40 years ago (Perea et al., 1984). After initial description of these reservoirs as tabular andesitic intrusions by Schiuma (1994), it took ca. 20 years before renewed efforts were made to develop models for the evolution of the fractured igneous reservoirs and their impact on the local source rocks (Spacapan et al., 2018; Witte et al., 2012). Below, I will present the current conceptual model for the evolution of the Río Grande Valley igneous petroleum systems (Figure 10), which is primarily the result of extensive subsurface and modeling studies published in the last 12 years (Rodriguez Monreal et al., 2009; Spacapan et al., 2018; Spacapan et al., 2020a; Spacapan et al., 2019; Witte et al., 2012).

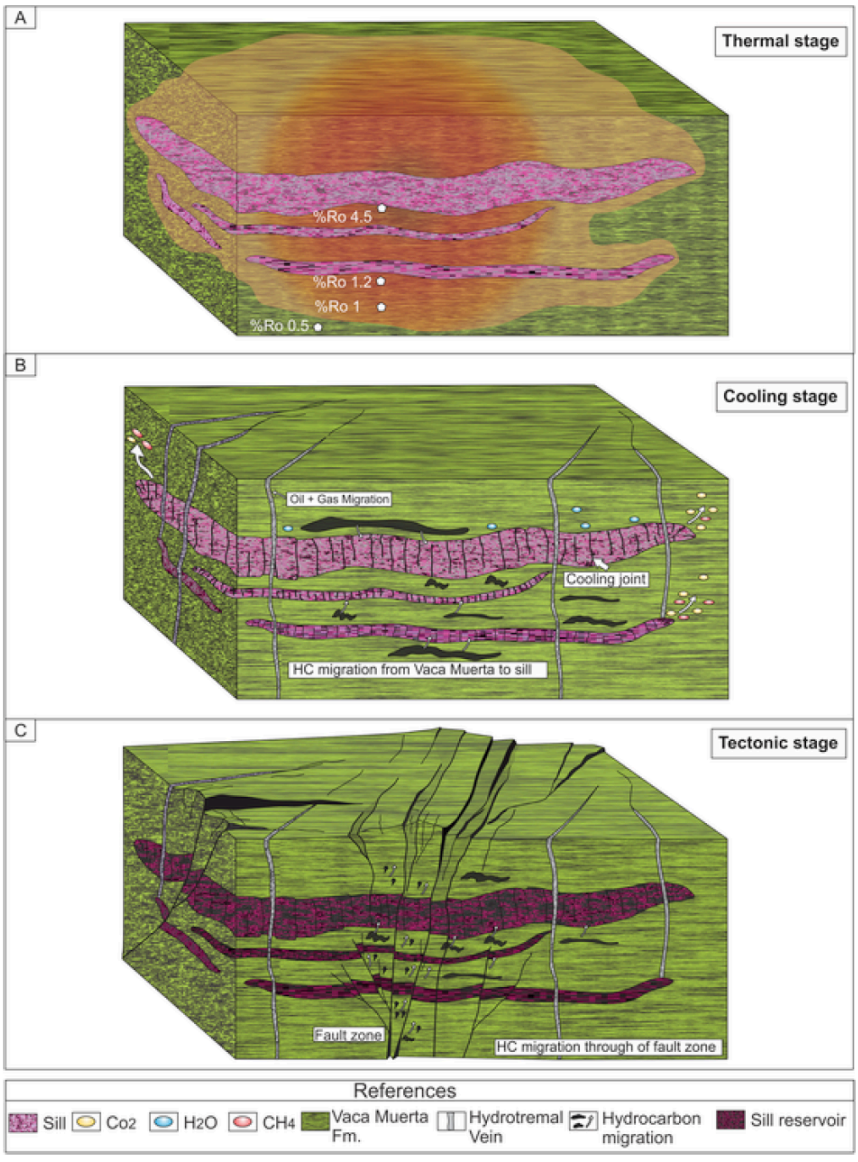

Figure 10. Conceptual model comprising (a) thermal stage, (b) cooling stage, and (c) tectonic stage of the evolution of the igneous petroleum systems in the Río Grande Valley. With permission from Spacapan et al. (2020a).

Emplacement of sill clusters during Miocene times was crucial to facilitate hydrocarbon generation, because shallow burial depth of the Agrío and Vaca Muerta formations (2-2.5 km depth) prevented significant burial-driven maturation (Spacapan et al., 2018). Spacapan et al. (2020a) term this phase of intrusion-driven charge the *thermal stage* (Figure 10a). Geometrically complex sill clusters intruded the shale formations in several pulses, leading to a strong but heterogeneous heating of the source rocks and thus a wide range of thermal maturity (Spacapan et al., 2018). Rodriguez Monreal et al. (2009) made similar observations in a nearby oilfield featuring fractured laccoliths within the source rock intervals and concluded that the variable heating may explain the wide range of observed oil gravity.

During the *cooling stage* (Figure 10b), the sills solidified and developed primary porosity such as cooling joints and vesicles. Meanwhile, fluid generation due to chemical reactions in the aureole continued, causing overpressure and generation of fracture networks in the low-permeable shale (Spacapan et al., 2020a; Spacapan et al., 2019). The model assumes that generation of porosity in the sills caused local underpressure, generating an inward-directed fluid pressure gradient that promoted initial hydrocarbon migration into the sill (Spacapan et al., 2020a; Witte et al., 2012). Note, however, that this early migration pulse has been proposed conceptually based on a study from another basin (Svensen et al., 2010), but timing, dynamics and P-T-conditions remain unclear in Río Grande Valley. In addition to cooling joints within the intrusion, hydrofractures in the aureole may enhance overall porosity and permeability in the vicinity of the sill intrusions and establish migration pathways for hydrothermal fluids and hydrocarbons (Spacapan et al., 2020a).

The post-magmatic *tectonic stage* (Figure 10c) includes tectonic faulting and fracturing of the sills, which generates more fracture porosity and better connectivity of flow paths in the sill reservoirs (Spacapan et al., 2020a; Witte et al., 2012). Faults may also allow further upward migration of hydrocarbons, thereby potentially allowing hydrocarbons to accumulate in upper sill levels, for instance in less organic-rich formations. In general, traps seem to be largely stratigraphic, and the organic-rich shales representing the source rocks are the sealing formations at the same time (Spacapan et al., 2020a; Witte et al., 2012). However, fractured dykes or transgressing sill limbs may provide seal-bypass mechanism (Spacapan et al., 2020a).

4. Summary of manuscripts

The review of the scientific background provided the not only the context and state of the art for the topic of my thesis, but also highlighted some of the existing knowledge gaps. The overarching goal of this work is to advance the understanding of fracturing in and around igneous intrusions and its influence on fluid flow and connect this knowledge with seismic exploration of intrusions in volcanic sedimentary basins. The thesis applies a wide spectrum of methods and consists of four separate manuscripts, of which three are published or accepted for publication by peer-reviewed journals and one is in final preparation for submission. I will use the following paragraphs not only to summarize the main findings of each individual manuscript, but also to point out the connection between the articles. For this purpose, I will present the manuscripts in an order that seems most natural to create this connection rather than sorting them by publication date.

As a reminder, the three main scientific aims of this these are to:

(1) Identify fracture mechanisms and quantify their influence on fracture networks in igneous intrusions emplaced in organic rich shale, focusing on intrusions that act as fractured hydrocarbon reservoirs.

    Addressed by Manuscript 1.

(2) Investigate the influence of porosity and permeability generation in a cooling sill and its metamorphic aureole due to fracturing on local hydrothermal flow and hydrocarbon transport.

    Addressed by Manuscripts 1, 2 and 3.

(3) Develop a workflow to model realistic seismic images of igneous sills, and use this workflow to understand how elastic property variations of sills and their host rock, e.g. due to fracturing or varying composition, change the seismic expression.

    Addressed by Manuscript 4.

All manuscripts, including supplementary material, are available in the Appendix of this thesis. The graphical abstract on page V visualizes the combined results of this thesis.

Manuscript 1*: *"Fracture networks in shale-hosted igneous intrusions: Processes, distribution, and implications for igneous petroleum systems"
(Journal of Structural Geology, in press; available online 21.06.2021

To address the first aim of th thesis, this work documents the range of fracture types and their involvement in fluid migration and storage and quantifies fracture network variability. The presented geological data from the El Manzano sill complex in the northern Neuquén Basin (cf. Figure 9) include field observations of different fracture types, geochemical analysis of host rock maturity and bitumen composition as well as detailed fracture network maps derived from high-resolution orthophotographs.

The fracture networks of the sills at El Manzano comprise four different fracture types that are associated with different physical processes: (1) Cooling joints resulting from thermal contraction of the cooling sill intrusion during magma solidification, (2) tectonic faults and tectonic, (3) bitumen dykes and injection structures and (4) hydrothermal calcite veins. The latter two fracture types are interpreted as the result of hydrofracturing due to fluid overpressure in a hydrothermal environment since they carry rock fragments from sills and the surrounding shale, and the bitumen is strongly graphitized. All fracture types may host solid bitumen or liquid hydrocarbons and are thus act as potential fluid pathways or storage.

Geochemical data shows that the sills were crucial for local hydrocarbon generation and migration at El Manzano. Background maturity of the organic-rich host rocks (Agrío Fm.) is very low because of relatively shallow burial depths (2-2.5 km) but increases strongly towards the intrusions. The bitumen dykes are localized around the sills and originate in the contact aureole. They usually consist of multiple dykelets, indicating several pulses of fluid flow. Raman spectra of samples from the bitumen dykes and good electrical conductivity evidence graphitization of the bitumen. Graphitization at such shallow burial must be driven by magmatic heat input. Thus, we argue that hydrocarbons migrated into the intrusions while they were still hot and were graphitized, probably at >350-400°C.

The combination of four different fracture types creates a highly heterogenous fracture network. The analysis of a 2D fracture map shows strong lateral variations of the fracture network. Faults and bitumen dykes increase fracture intensity and connectivity, a wider orientation distribution and a varying fracture length distribution relative to background fracturing with only cooling joints. Thus, not only faults, but also bitumen dykes can contribute to increased fracturing and improve fluid flow properties. Length distributions are variable but follow a log-normal distribution rather than previously suggested power-law.

In summary, the study extends the understanding of fracture networks of igneous sill intrusions emplaced in organic-rich shale, which can be much more variable than previously thought. Except tectonic fractures, all fracture types form due to intrusion cooling or intrusion-driven hydrothermal processes. The study provides new geological data to constrain and interpret numerical modeling results (manuscripts 2 and 3) of the underlying THMC processes, but also for reservoir modeling of igneous intrusions.

Manuscript 2*: *"Impact of permeability evolution in igneous sills on hydrothermal flow and hydrocarbon transport in volcanic sedimentary basins"
(in final preparation before submission)

The second manuscript builds upon and extends the geological field evidence presented in the first manuscript and integrates it with numerical modeling. Using the finite-element method (FEM), we simulate intrusion-driven hydrocarbon generation, fracturing and hydrothermal flow around impermeable vs. permeable intrusions emplaced in a low-permeability host rock. In this way, the study investigates the influence of permeability evolution on hydrothermal flow and transport of hydrocarbons generated around intrusions (scientific aim 2).

The extended field evidence shows that graphitized bitumen within intrusions also occurs in other outcropping sill complexes in the study area. Additionally, the manuscript provides observations of bitumen or fluidized bituminous shale occupying the cooling joint network. Both shale fluidization and graphitization of bitumen requires high temperatures (>350-400°C) and fluid overpressure. We use these observations to argue that the early fracture network of intrusions, including cooling joints and bitumen dykes, must become accessible to fluid flow shortly after the magma has solidified.

Accordingly, the modelling part of the study investigates hydrothermal flow and transport of locally generated hydrocarbons around an intrusion that becomes porous and permeable once it reaches the solidus temperature, i.e., cooling joints are formed. We identify three main flow phases. (1) Before the sill becomes fully permeable, strong overpressure and hydrofracturing drives hydrothermal fluids and hydrocarbons towards the intrusion tips, where initial plumes form. (2) When the sill becomes fully permeable, the fluids exploit the newly established pathway, and the flow suddenly becomes vertical. Hydrocarbons trapped in the aureole below the sill are "flushed" through the sill, releasing much of the fluid overpressure. In this phase, the sill is >400°C hot. This fits very well with the field observations of graphitized bitumen observed in the fractures inside the sills. (3) Finally, the change in the fluid pressure field initiates backward flow towards the sill tip, which may lead to some accumulation of hydrocarbons in the intrusion. Parameter testing indicates that the last phase (backward flow) only occurs for sills that are at least 30 m thick. The flow patterns around permeable intrusions differ markedly from an impermeable sill, which has been the standard scenario in previous modeling studies of hydrothermal flow around sills. An impermeable sill can sustain high fluid overpressures in the host rock aureole below them, which may drive flow and hydrocarbons to the tip and feed hydrothermal upward migration in plumes.

Overall, the results have some important implications for hydrothermal flow in volcanic basins. Permeability evolution in igneous sills can reconfigure hydrothermal flow and efficiently release fluid overpressure. This can drive hydrocarbons into the hot sill and lead to formation of graphite or graphitic bitumen, which means that initial hydrocarbon migration into the sill is likely not beneficial from a petroleum system standpoint. For the understanding of hydrothermal flow in volcanic sedimentary basins, this study shows that hydrothermal flow and hydrocarbon transport through fractured sills should be considered as a possibility.

Manuscript 3 "Numerical modeling of fracture network evolution in organic-rich shale with rapid internal fluid generation"

(Published in Journal of Geophysical Research – Solid Earth on 3rd June 2020)

The third manuscript focuses on the evolution of fracture networks in shales with fast internal fluid production. These fracture networks control fluid expulsion and migration in shale, but their complex evolution is not captured in the large-scale hydrothermal simulations used in the second manuscript. Therefore, this manuscript aims to better understand the fracture network evolution and fluid expulsion on the cm-scale and assess the effect of far-field stresses and initial micro-fracturing on fracture geometry and connectivity.

The study uses the extended finite element method (X-FEM) to simulate coupled hydromechanical propagation of a 2D fracture network. The network starts as a grid of microcracks with high pore fluid pressure representing initial cracks around hydrocarbon-generating kerogen patches. We compare fracture propagation and network evolution under varying stress anisotropy and initial microcrack orientation by quantifying the cumulative fracture length, opening, average propagation angle and network connectivity for each simulation. We then combine the evolution of this set of network parameters with the stress field in the model to link the fracture network evolution to the local stress state.

The simulations show that the dynamics of fracture network growth and fluid expulsion follow three main phases. First, we observe initial growth of cracks with limited fracture opening and propagation angles aligning with far-field stresses. In the second phase, fractures begin to interact and coalesce, leading to local stress redistribution and deviation from the previous propagation direction. Finally, fluid expulsion occurs from the fully developed fracture network, stresses relax, and fractures close. This behavior fits with laboratory observations from heated shale, which show pulses of opening and closure corresponding to fluid generation and pressure build-up followed by expulsion-related pressure relaxation.

Furthermore, the study shows that higher stress anisotropy causes stronger fracture alignment with the largest principal stress and larger fracture opening, leading to a network that consists of aligned fracture arrays and shows high directional, but relatively low overall connectivity. Highest network connectivity is achieved if either stress is nearly isotropic and the initial fractures are randomly oriented, or if mild stress anisotropy (5-10%) is combined with aligned initial microcracks. The latter scenario is particularly interesting when interpreting the results in the context of layered organic-rich shale.

This work represents a step towards bridging the gap between small-scale fracturing and large-scale simulations of magma-shale interactions. The results show that connectivity of fracture networks in shales can be highly anisotropic and variable in their overall connectivity. Large-scale simulations will need to be informed by further small-scale laboratory and modeling studies to correctly implement the effect of fracturing on permeability evolution, especially in terms of potential permeability anisotropy.

Manuscript 4: "From field analogues to realistic seismic modelling: a case study of an oil-producing andesitic sill complex in the Neuquén Basin, Argentina
(Published in Journal of the Geological Society on 2nd March 2018)

In the fourth manuscript, the focus shifts to seismic exploration of igneous intrusions to address the third aim of the thesis. A realistic seismic forward-modelling workflow should consider geological complexity of the target, detailed information on the distribution of seismic velocity and density and adequate modelling technique that correctly implements resolution and illumination. We use the kilometer-scale outcropping sill complex at El Manzano to develop and demonstrate such a workflow. The results help us to understand how the seismic expression changes with elastic property of sills and their host rock, for instance due to fracturing or varying composition.

The workflow comprises three main steps. First, we generate a 3D digital outcrop model of a suitable analogue outcrop. In this case, we acquire a set of overlapping aerial photographs from the El Manzano sill complex and use structure-from-motion photogrammetry to generate the digital model. This model then provides a high-resolution interpretation of the sill complex with geometries resolved at the sub-meter scale. We then use well data to build a detailed elastic property model of the host rock. Combining the real sill geometries from the outcrop with subsurface data creates a realistic geological and geophysical model. Finally, an advanced 2D convolution technique generates synthetic seismic images representing realistic resolution and illumination conditions.

The results illustrate that including intrusion geometries at the sub-seismic scale, i.e., below the "quarter-wavelength" resolution limit, is important to create a realistic forward-modelled seismic image. The reason is that, for instance, stacked, thin sills may cause characteristic interference patterns in the seismic waveforms, such as "pseudo-faults" or splitting and "braided" reflections. Such patterns can then be used to identify intruded intervals in seismic images, even if it is impossible to identify single intrusions.

In addition, good knowledge of the lithological variations is key to predict seismic response of sill intrusions. If the host rock has relatively homogeneous elastic properties and much lower seismic velocities than the intrusions (e.g., dolerite in siliciclastic rocks), strong reflections are observed. However, the host rocks in the Neuquén Basin are extremely variable and contain high-velocity rocks like carbonates and evaporites. The sills are andesitic and heavily fractured, which can reduce velocities compared to more mafic or unfractured intrusions. As a result, many sill intrusions are challenging to detect due to low reflection amplitudes, and mainly cause subtle disturbance of the sedimentary reflections.

The main conclusion of this work is that one should avoid generalized statements on the seismic response of igneous intrusions. It should be reviewed under explicit consideration of the factors that may influence the seismic property contrasts, which include host rock lithology, fracturing and composition of intrusions. Thus, case-by-case evaluation using a realistic, outcrop-based forward-modelling workflow can be a valuable tool for interpreters.

5. Discussion and Outlook

In this final chapter, I will put the results of this thesis in context with the current state of research presented in chapters 2 and 3. This includes a discussion of the advances made in the understanding of geological processes related to intrusion fracturing, magma-shale interaction, their implications for igneous petroleum systems in the Río Grande Valley and in general, as well as the main take-away messages for seismic exploration targeting intrusions. At the end of this chapter, I will additionally provide some recommendations for future research based on the findings of my work.

Fracture network evolution in igneous sills

The existing literature describes the fracture systems of igneous intrusions mainly as networks of cooling joints that may be modified by tectonic faulting and jointing (Senger et al., 2015; Witte et al., 2012). These processes are well understood, and it is widely accepted that factors like intrusion geometry or fault-proximity control parameters like fracture orientation and intensity (Hetényi et al., 2012; Kattenhorn and Schaefer, 2008; Witte et al., 2012). However, very few studies quantitatively describe fracture network properties of intrusions, and their observations are not consistent. Senger et al. (2015) pointed out the "pervasive heterogeneity" of fracture networks in studied dolerite intrusions, which were highly variable both between different sites and in the same outcrop. Witte et al. (2012) on the other hand suggested scale-independency (power-law behavior) and lateral consistency of the fracture parameters in andesitic intrusions of the Neuquén Basins. This thesis adds another quantitative dataset to the research, and specifically focuses on the question of heterogeneity and scaling (manuscript 1).

Based on the results, I argue that fracture networks of igneous intrusion are indeed "pervasively heterogenous", especially when they are emplaced within organic-rich shale and located in tectonically active regions. The reason for this is the mix of different fracturing mechanisms involved in the fracture network evolution: Thermal contraction (cooling joints), hydrofracturing (bitumen dykes and sediment injections), and tectonic shearing and jointing all contribute, but often in different locations. Especially bitumen dykes as a fracture mechanism of intrusions represent a novel finding, since hydrofracturing and bitumen dyke formation due to hydrocarbon generation has usually been described as a process affecting the sediments around intrusions, but not intrusions themselves (Aarnes et al., 2012; Cobbold et al., 2014; Zanella et al., 2015). Moreover, the field study took extreme care to evaluate scaling relationships and can with near certainty rule out power-law behavior of fracture lengths. Even the scaling relations themselves are laterally inconsistent, but best described by log-normal distributions. This fits well with theoretical considerations of fracture networks confined to layers, which certainly applies to sill intrusions (Bonnet et al., 2001). With these results in mind, this thesis has advanced our understanding of fracture networks and their evolution in igneous sills and provides valuable insight and data for both academia and industry.

Magma-shale interaction and coupled THMC processes around intrusions

The presented work also advances our understanding of magma-shale interaction. In studies of large-scale THMC processes, such as hydrothermal venting, intrusions have usually been assumed to be impermeable (Galerne and Hasenclever, 2019; Iyer et al., 2013; Iyer et al., 2017). The field observations of liquified shale and/or graphite or graphitic bitumen occupying the fracture network of sill intrusions show that intrusions can become permeable upon solidification (manuscripts 1 and 2). Although Svensen et al. (2010) describes sediment dykes that must have entered intrusions shortly after solidification, graphitic bitumen dykes within shallow igneous intrusions represent a novel observation to the best of my knowledge. Hydrothermal modelling shows that this finding has important implications, because hydrothermal flow patterns and thus hydrocarbon transport paths change distinctly if intrusions become permeable during cooling (manuscript 2). While especially thick sills may indeed not be fractured, there is increasing evidence that porous and permeable intrusions in volcanic sedimentary basins may be found in many sedimentary volcanic basins (Schofield et al., 2020; Teske et al., 2020; Witte et al., 2012). Therefore, transport of hydrothermal fluids and hydrocarbons through hot sills should be considered a possibility in all volcanic basins. Because of the strong impact on flow patterns and hydrocarbon transport, numerical simulations need to justify their choice for porosity and permeability of igneous intrusions. This adds yet another aspect to consider in the already complex geological processes of volcanic sedimentary basins.

Concerning the understanding of THMC processes in the aureole on the microscale, this work advanced modelling of fracturing in shales due to fluid generation by focusing on a better quantitative description of the fracture network *evolution*. Previous studies mainly focused on comparing final fracture networks for different scenarios of stress anisotropy, kerogen distribution or mechanical layering (Chauve et al., 2020; Teixeira et al., 2017), we introduced an easily understandable set of parameters that describe the evolving fracture network over time and can be combined with stress maps. In this way, it is possible to connect the stress state and its changes to geologically important events like opening or closing of fractures, or the development of connectivity. In addition, monitoring the fracture propagation and network evolution allows a direct comparison to the observations of natural hydrofracturing processes in shale and gelatin experiments. By demonstrating that the numerical models show similar dynamics as natural systems, i.e., 3-phase growth and pulse-like fluid escape (Kobchenko et al., 2014; Panahi et al., 2018; Panahi et al., 2019), the third manuscript builds confidence in the presented models as a foundation for studies including more realistic setups. Even the results from the simple setup indicate that variable geological boundary conditions like alignment of initial microcracks and far-field stress can cause significant variations in network connectivity and fracture alignment, which could lead to anisotropic permeability.

Implications for igneous petroleum systems

The results also have implications for igneous petroleum systems, especially those in the Río Grande Valley, Argentina. The occurrence of graphite suggests that early fracture porosity development may indeed lead to a first migration pulse as postulated by previous studies (Spacapan et al., 2020a; Witte et al., 2012), but the hydrocarbons migrating into the intrusions during this first pulse are unlikely to survive. The hydrothermal modeling (manuscript 2) provides an explanation, because instead of slowly migrating into the fractured intrusion as previously thought, the hydrocarbons generated in the aureole flow towards and through the intrusion at temperatures of >400°C. Likely this has been overlooked in previous thermal modeling studies of intrusions in source rock intervals. These studies focused on the thermal effect on maturity alone that is well described by conductive heat transfer but did not explore early hydrothermal migration (Aarnes et al., 2011; Spacapan et al., 2018; Sydnes et al., 2018).

Based on the results of the first and second manuscript, I argue that *thermal* and *cooling* stage (Figure 10a, b) are not separable events, but characterized by simultaneous processes. Hydrocarbons are continuously generated in the aureole, both before and after formation of fractures in the intrusions and in the aureole itself. Nevertheless, our understanding of the migration mechanisms and timing remains incomplete because hydrocarbon generation and hydrothermal flow involving multiple fractured intrusions have not yet been investigated.

Seismic imaging of intrusions

The thesis also raises awareness for the range of possible expressions of igneous sills in seismic reflection data and provides an outcrop-based seismic modeling workflow that is applicable to different geological settings. Manuscript 4 highlights that seismic velocity and thus acoustic impedance contrasts between intrusions and their hosts are not always as large as often postulated in the existing literature (e.g., Magee et al., 2015b; Planke et al., 2015). High-velocity rocks like evaporites and carbonates may reduce acoustic impedance contrasts and seismic reflection amplitudes from intrusion-sediment interfaces. Fractured and more silicic intrusions like the sills in the northern Neuquén Basin can reduce the amplitudes even more, up to the point where intrusions can be transparent or cause soft reflections. Even larger sill complexes like in the Río Grande Valley that we would usually expect to be easily detectable may be challenging to detect, if intra-sedimentary seismic properties contrasts are high and intrusions are stacked and largely layer-parallel. This means that resolution is a not the only limiting factor for the imaging of intrusions in volcanic basins. Importantly, Mark et al. (2018) published a study almost simultaneously to manuscript 4, which concurs with the findings of our work. They report silicic intrusions in the Faroe Shetland Basin that either show relatively low-amplitude reflection or are completely hidden. Therefore, it is crucial for interpreters to be aware of the full range of expected property contrasts in the basin of interest. Looking for the typical high-amplitude reflections is a proven and often successful approach to map sill complexes in seismic data but may also suffer from confirmation bias and lead to erroneous or incomplete interpretation results.

Outlook

As is the case with most research projects, my thesis sparks at least as many new questions as it provides answers. Here, I would like to outline a few suggestions for future research.

Firstly, the occurrence of graphite in the outcrops of my study area could have implications for igneous petroleum systems (destroyed hydrocarbons), greenhouse gas release (reduced CH_4-CO_2 emissions) and other economic sectors such as graphite mining. More systematic field campaigns focused on this topic can help to quantify the proportion of carbon trapped as graphitic bitumen or pure graphite in the sill-aureole systems in volcanic basins. Due to their immense size, high outcrop-quality and good accessibility, outcrops like El Manzano are ideal for this task. Note that the 5 km of outcrop that we explored in detail for this work represents around half of the total outcrop. Reconstructing the emplacement history of this large sill complex is a task that, combined with other geological and geophysical data, could turn this into a true showcase for igneous petroleum systems.

Secondly, the scale gap in the modeling of THMC processes needs to be reduced, and knowledge from laboratory measurements and simulations should be included in large-scale hydrothermal models. The effect of permeability increase should be better quantified to include e.g., permeability anisotropy depending on the far-field stresses. To take the next step towards realistic modeling, simulations of hydrothermal flow around sills also need to consider porosity-reducing processes such as mineral precipitation (Townsend, 2018) and a more detailed implementation of magma solidification.

I hope that this thesis contributes to the awareness of the wide range of possible seismic expressions of igneous sills. Future modeling work should also include lateral variations of velocities within the sills. Manuscript 1 shows how variable fracturing along sills can be, and this will certainly alter the seismic response. However, the link between geological factors related to intrusions, such as fracturing, alteration and primary composition and seismic velocities remains qualitative in this work. To extract more information from sonic logs and seismic data, relationships between petrophysics and seismic properties need to be established, for instance via laboratory analysis and rock physics modeling. Rock physics modeling could offer a valuable tool especially for applied geoscientists who need to characterize igneous rocks as reservoirs, e.g., in geothermal energy, hydrocarbon exploration or carbon-capture and storage projects in igneous rocks.

References

Aarnes, I., Planke, S., Trulsvik, M. and Svensen, H., 2015. Contact metamorphism and thermogenic gas generation in the Vøring and Møre basins, offshore Norway, during the Paleocene–Eocene thermal maximum. Journal of the Geological Society, 172(5): 588-598.

Aarnes, I., Podladchikov, Y. and Svensen, H., 2012. Devolatilization-induced pressure build-up: Implications for reaction front movement and breccia pipe formation. Geofluids, 12(4): 265-279.

Aarnes, I., Svensen, H., Connolly, J.A.D. and Podladchikov, Y.Y., 2010. How contact metamorphism can trigger global climate changes: Modeling gas generation around igneous sills in sedimentary basins. Geochimica et Cosmochimica Acta, 74(24): 7179-7195.

Aarnes, I., Svensen, H., Polteau, S. and Planke, S., 2011. Contact metamorphic devolatilization of shales in the Karoo Basin, South Africa, and the effects of multiple sill intrusions. Chemical Geology, 281(3-4): 181-194.

Anell, I., Lecomte, I., Braathen, A. and Buckley, S., 2016. Synthetic seismic illumination of small-scale growth faults, paralic deposits and low-angle clinoforms: A case study of the Triassic successions on Edgeøya, NW Barents Shelf. Marine and Petroleum Geology, 77: 625-639.

Bell, B. and Butcher, H., 2002. On the emplacement of sill complexes: evidence from the Faroe-Shetland Basin. In: D.W. Jolley and B.R. Bell (Editors), The North Atlantic Igneous Province: Stratigraphy, Tectonic, Volcanic and Magmatic Processes. Geological Society, London, Special Publications, pp. 307-329.

Berge, P.A., Fryer, G.J. and Wilkens, R.H., 1992. Velocity-porosity relationships in the upper oceanic crust: Theoretical considerations. Journal of Geophysical Research: Solid Earth, 97(B11): 15239-15254.

Bermúdez, A. and Delpino, D.H., 2008. Concentric and radial joint systems within basic sills and their associated porosity enhancement, Neuquén Basin, Argentina. Geological Society, London, Special Publications, 302(1): 185-198.

Berndt, C., Hensen, C., Mortera-Gutierrez, C., Sarkar, S., Geilert, S., Schmidt, M., Liebetrau, V., Kipfer, R., Scholz, F., Doll, M., Muff, S., Karstens, J., Planke, S., Petersen, S., Böttner, C., Chi, W.-C., Moser, M., Behrendt, R., Fiskal, A., Lever, M., Su, C.-C., Deng, L., Brennwald, M. and Lizarralde, D., 2016. Rifting under steam—How rift magmatism triggers methane venting from sedimentary basins. Geology.

Berndt, C., Skogly, O.P., Planke, S., Eldholm, O. and Mjelde, R., 2000. High-velocity breakup-related sills in the Vøring Basin, off Norway. Journal of Geophysical Research: Solid Earth, 105(B12): 28443-28454.

Bischoff, A.P., Nicol, A. and Beggs, M., 2017. Stratigraphy of architectural elements in a buried volcanic system and implications for hydrocarbon exploration. Interpretation, 5(3): SK141-SK159.

Bonnet, E., Bour, O., Odling, N.E., Davy, P., Main, I., Cowie, P. and Berkowitz, B., 2001. Scaling of fracture systems in geological media. Reviews of Geophysics, 39(3): 347-383.

Cartwright, J., Huuse, M. and Aplin, A., 2007. Seal bypass systems. AAPG bulletin, 91(8): 1141-1166.

Casini, G., Hunt, D.W., Monsen, E. and Bounaim, A., 2016. Fracture characterization and modeling from virtual outcrops. AAPG Bulletin, 100(1): 41-61.

Chauve, T., Scholtes, L., Donzé, F.v., Haque Mondol, N. and Renard, F., 2020. Layering in shales controls microfracturing at the onset of primary migration in source rocks. Journal of Geophysical Research: Solid Earth, 125(5): e2020JB019444.

Cobbold, P.R., Ruffet, G., Leith, L., Loseth, H., Rodrigues, N., Leanza, H.A. and Zanella, A., 2014. Radial patterns of bitumen dykes around Quaternary volcanoes, provinces of northern Neuquén and southernmost Mendoza, Argentina. Journal of South American Earth Sciences, 56: 454-467.

Combina, A.M. and Nullo, F., 2011. Ciclos tectónicos, volcánicos y sedimentarios del Cenozoico del sur de Mendoza-Argentina (35-37 S y 69 30'W). Andean geology, 38(1): 198-218.

Connolly, J., 2009. The geodynamic equation of state: what and how. Geochemistry, Geophysics, Geosystems, 10(10).

de Miranda, F.S., Vettorazzi, A.L., da Cruz Cunha, P.R., Aragão, F.B., Michelon, D., Caldeira, J.L., Porsche, E., Martins, C., Ribeiro, R.B. and Vilela, A.F., 2018. Atypical igneous-sedimentary petroleum systems of the Parnaíba Basin, Brazil: seismic, well logs and cores. Geological Society, London, Special Publications, 472(1): 341-360.

Delaney, P.T., 1982. Rapid intrusion of magma into wet rock: Groundwater flow due to pore pressure increases. Journal of Geophysical Research: Solid Earth, 87(B9): 7739-7756.

Delpino, D. and Bermúdez, A., 2009. Petroleum systems including unconventional reservoirs in intrusive igneous rocks (sills and laccoliths). The Leading Edge, 28(7): 804-811.

Eide, C.H., Schofield, N., Jerram, D.A. and Howell, J.A., 2016. Basin-scale architecture of deeply emplaced sill complexes: Jameson Land, East Greenland. Journal of the Geological Society: 1-18.

Eide, C.H., Schofield, N., Lecomte, I., Buckley, S.J. and Howell, J.A., 2017. Seismic interpretation of sill complexes in sedimentary basins: implications for the sub-sill imaging problem. Journal of the Geological Society.

Einsele, G., Gieskes, J.M., Curray, J., Moore, D.M., Aguayo, E., Aubry, M.-P., Fornari, D., Guerrero, J., Kastner, M., Kelts, K., Lyle, M., Matoba, Y., Molina-Cruz, A., Niemitz, J., Rueda, J., Saunders, A., Schrader, H., Simoneit, B. and Vacquier, V., 1980. Intrusion of basaltic sills into highly porous sediments, and resulting hydrothermal activity. Nature, 283(5746): 441-445.

Espitalié, J., Deroo, G. and Marquis, F., 1985. La pyrolyse Rock-Eval et ses applications. Revue de l'Institut français du pétrole, 40: 563-579.

Festøy, M.H., 2017. Integrated characterization of igneous intrusions in Central Spitsbergen, UiT Norges arktiske universitet.

Folguera, A., Bottesi, G., Duddy, I., Martín-González, F., Orts, D., Sagripanti, L., Vera, E.R. and Ramos, V., 2015. Exhumation of the Neuquén Basin in the southern Central Andes (Malargüe fold and thrust belt) from field data and low-temperature thermochronology. Journal of South American Earth Sciences, 64: 381-398.

Galerne, C.Y. and Hasenclever, J., 2019. Distinct Degassing Pulses During Magma Invasion in the Stratified Karoo Basin—New Insights From Hydrothermal Fluid Flow Modeling. Geochemistry, Geophysics, Geosystems, 20(6): 2955-2984.

Galland, O., Bertelsen, H., Eide, C., Guldstrand, F., Haug, Ø., Leanza, H.A., Mair, K., Palma, O., Planke, S. and Rabbel, O., 2018. Storage and transport of magma in the layered crust—Formation of sills and related flat-lying intrusions, Volcanic and igneous plumbing systems. Elsevier, pp. 113-138.

Galland, O., Cobbold, P.R., Hallot, E., de Bremond d'Ars, J. and Delavaud, G., 2006. Use of vegetable oil and silica powder for scale modelling of magmatic intrusion in a deforming brittle crust. Earth and Planetary Science Letters, 243(3–4): 786-804.

Galland, O., De Bremond d'Ars, J., Cobbold, P.R. and Hallot, E., 2003. Physical models of magmatic intrusion during thrusting. Terra Nova, 15(6): 405-409.
Galland, O., Hallot, E., Cobbold, P.R., Ruffet, G. and de Bremond D'Ars, J., 2007. Volcanism in a compressional Andean setting: A structural and geochronological study of Tromen volcano (Neuquén province, Argentina). Tectonics, 26(4).
Galland, O., Spacapan, J.B., Rabbel, O., Mair, K., Soto, F.G., Eiken, T., Schiuma, M. and Leanza, H.A., 2019. Structure, emplacement mechanism and magma-flow significance of igneous fingers–Implications for sill emplacement in sedimentary basins. Journal of Structural Geology, 124: 120-135.
Goehring, L. and Morris, S.W., 2005. Order and disorder in columnar joints. EPL (Europhysics Letters), 69(5): 739.
Goehring, L. and Morris, S.W., 2008. Scaling of columnar joints in basalt. Journal of Geophysical Research: Solid Earth, 113(B10): n/a-n/a.
Goehring, L., Morris, S.W. and Lin, Z., 2006. Experimental investigation of the scaling of columnar joints. Physical Review E, 74(3): 036115.
Gudmundsson, A. and Løtveit, I.F., 2014. Sills as fractured hydrocarbon reservoirs: examples and models. Geological Society, London, Special Publications, 374(1): 251-271.
Hamilton, R. and Minshell, B., 2019. Hydrothermal vents and seismic anomalies: implications for the petroleum system NE of Shetland. Petroleum Geoscience, 25(1): 90-101.
Hansen, D.M. and Cartwright, J., 2006. The three-dimensional geometry and growth of forced folds above saucer-shaped igneous sills. Journal of Structural Geology, 28(8): 1520-1535.
Healy, D., Rizzo, R.E., Cornwell, D.G., Farrell, N.J., Watkins, H., Timms, N.E., Gomez-Rivas, E. and Smith, M., 2017. FracPaQ: A MATLAB™ toolbox for the quantification of fracture patterns. Journal of Structural Geology, 95: 1-16.
Hetényi, G., Taisne, B., Garel, F., Médard, É., Bosshard, S. and Mattsson, H.B., 2012. Scales of columnar jointing in igneous rocks: field measurements and controlling factors. Bulletin of Volcanology, 74(2): 457-482.
Howell, J.A., Schwarz, E., Spalletti, L.A. and Veiga, G.D., 2005. The Neuquén Basin: an overview. In: G.D. Veiga, L.A. Spalletti, J.A. Howell and E. Schwarz (Editors), Geological Society, London, Special Publications, pp. 1-14.
Infante-Paez, L. and Marfurt, K., 2017. Seismic expression and geomorphology of igneous bodies. A Taranaki Basin, New Zealand case study. Interpretation: 1-72.
Infante-Paez, L. and Marfurt, K.J., 2018. In-context interpretation: Avoiding pitfalls in misidentification of igneous bodies in seismic data. Interpretation, 6(4): SL29-SL42.
Iyer, K., Rüpke, L. and Galerne, C.Y., 2013. Modeling fluid flow in sedimentary basins with sill intrusions: Implications for hydrothermal venting and climate change. Geochemistry, Geophysics, Geosystems, 14(12): 5244-5262.
Iyer, K., Schmid, D.W., Planke, S. and Millett, J., 2017. Modelling hydrothermal venting in volcanic sedimentary basins: Impact on hydrocarbon maturation and paleoclimate. Earth and Planetary Science Letters, 467: 30-42.
Iyer, K., Svensen, H. and Schmid, D.W., 2018. SILLi 1.0: a 1-D numerical tool quantifying the thermal effects of sill intrusions. Geoscientific Model Development, 11(1): 43-60.
Jackson, C.A.-L., Magee, C. and Jacquemyn, C., 2020. Rift-related magmatism influences petroleum system development in the NE Irish Rockall Basin, offshore Ireland. Petroleum Geoscience, 26(4): 511-524.
Jackson, C.A.-L., Schofield, N. and Golenkov, B., 2013. Geometry and controls on the development of igneous sill–related forced folds: A 2-D seismic reflection case study

from offshore southern Australia. Geological Society of America Bulletin, 125(11-12): 1874-1890.
Jaeger, J., 1961. The cooling of irregularly shaped igneous bodies. American Journal of Science, 259(10): 721-734.
Jamtveit, B., Krotkiewski, M., Kobchenko, M., Renard, F. and Angheluta, L., 2014. Pore-space distribution and transport properties of an andesitic intrusion. Earth and Planetary Science Letters, 400: 123-129.
Jamtveit, B., Svensen, H., Podladchikov, Y.Y. and Planke, S., 2004. Hydrothermal vent complexes associated with sill intrusions in sedimentary basins. Physical Geology of High-Level Magmatic Systems. Geological Society, London, Special Publications, 234: 233-241.
Jerram, D.A. and Bryan, S.E., 2017. Plumbing Systems of Shallow Level Intrusive Complexes. In: C. Breitkreuz and S. Rocchi (Editors), Advances in Volcanology. Springer Berlin Heidelberg, Berlin, Heidelberg, pp. 1-22.
Kattenhorn, S.A. and Schaefer, C.J., 2008. Thermal–mechanical modeling of cooling history and fracture development in inflationary basalt lava flows. Journal of Volcanology and Geothermal Research, 170(3-4): 181-197.
Kay, S.M., Burns, W.M., Copeland, P. and Mancilla, O., 2006. Upper Cretaceous to Holocene magmatism and evidence for transient Miocene shallowing of the Andean subduction zone under the northern Neuquén Basin. Geological Society of America Special Papers, 407: 19-60.
Kjoberg, S., Schmiedel, T., Planke, S., Svensen, H., Millett, J., Jerram, D., Galland, O., Lecomte, I., Schofield, N., Haug, Ø. and Helsem, A., 2017. 3D structure and formation of hydrothermal vent complexes at the Paleocene-Eocene transition, the Møre Basin, mid-Norwegian margin. Interpretation: SK65-SK81.
Klarner, S. and Klarner, O., 2012. Identification of paleo-volcanic rocks on seismic data. INTECH Open Access Publisher.
Kobchenko, M., Hafver, A., Jettestuen, E., Renard, F., Galland, O., Jamtveit, B., Meakin, P. and Dysthe, D.K., 2014. Evolution of a fracture network in an elastic medium with internal fluid generation and expulsion. Physical Review E, 90(5): 052801.
Kobchenko, M., Panahi, H., Renard, F., Dysthe, D.K., Malthe-Sørenssen, A., Mazzini, A., Scheibert, J., Jamtveit, B. and Meakin, P., 2011. 4D imaging of fracturing in organic-rich shales during heating. Journal of Geophysical Research: Solid Earth, 116(B12): n/a-n/a.
Kontorovich, A.E., Khomenko, A.V., Burshtein, L.M., Likhanov, I.I., Pavlov, A.L., Staroseltsev, V.S. and Ten, A.A., 1997. Intense basic magmatism in the Tunguska petroleum basin, eastern Siberia, Russia. Petroleum Geoscience, 3(4): 359-369.
Lecomte, I., Lavadera, P.L., Anell, I., Buckley, S.J., Schmid, D.W. and Heeremans, M., 2015. Ray-based seismic modeling of geologic models: Understanding and analyzing seismic images efficiently. Interpretation, 3(4): SAC71-SAC89.
Lecomte, I., Lavadera, P.L., Botter, C., Anell, I., Buckley, S.J., Eide, C.H., Grippa, A., Mascolo, V. and Kjoberg, S., 2016. 2 (3) D convolution modelling of complex geological targets beyond–1D convolution. First Break, 34(5): 99-107.
Magee, C., Duffy, O.B., Purnell, K., Bell, R.E., Jackson, C.A.L. and Reeve, M.T., 2015a. Fault-controlled fluid flow inferred from hydrothermal vents imaged in 3D seismic reflection data, offshore NW Australia. Basin Research: 1-20.
Magee, C., Jackson, C., Hardman, J. and Reeve, M., 2017. Decoding sill emplacement and forced fold growth in the Exmouth Sub-basin, offshore northwest Australia: Implications for hydrocarbon exploration. Interpretation: SK11-SK22.

Magee, C., Jackson, C.A.-L. and Schofield, N., 2013. The influence of normal fault geometry on igneous sill emplacement and morphology. Geology, 41(4): 407-410.
Magee, C., Maharaj, S.M., Wrona, T. and Jackson, C.A.-L., 2015b. Controls on the expression of igneous intrusions in seismic reflection data. Geosphere, 11(4): 1024-1041.
Magee, C., Muirhead, J.D., Karvelas, A., Holford, S.P., Jackson, C.A.L., Bastow, I.D., Schofield, N., Stevenson, C.T.E., McLean, C. and McCarthy, W., 2016. Lateral magma flow in mafic sill complexes. Geosphere, 12(3): 809-841.
Magee, C., Stevenson, C.T., Ebmeier, S.K., Keir, D., Hammond, J.O., Gottsmann, J.H., Whaler, K.A., Schofield, N., Jackson, C.A. and Petronis, M.S., 2018. Magma plumbing systems: a geophysical perspective. Journal of Petrology, 59(6): 1217-1251.
Maher, H., Senger, K., Braathen, A., Mulrooney, M.J., Smyrak-Sikora, A., Osmundsen, P.T. and Ogata, K., 2020. Mesozoic-Cenozoic Regional Stress Field Evolution in Svalbard. Tectonics, 39(4): e2018TC005461.
Manceda, R. and Figueroa, D., 1995. Inversion of the Mesozoic Neuquén rift in the Malargüe fold and thrust belt, Mendoza, Argentina. In: A.J. Tankard, S. S. and H.J. Welsink (Editors), Petroleum basins of South America: AAPG Memoir, pp. 369–382.
Mark, N., Schofield, N., Pugliese, S., Watson, D., Holford, S., Muirhead, D., Brown, R. and Healy, D., 2018. Igneous intrusions in the Faroe Shetland basin and their implications for hydrocarbon exploration; new insights from well and seismic data. Marine and Petroleum Geology, 92: 733-753.
Mazzini, A., Svensen, H., Akhmanov, G., Aloisi, G., Planke, S., Malthe-Sørenssen, A. and Istadi, B., 2007. Triggering and dynamic evolution of the LUSI mud volcano, Indonesia. Earth and Planetary Science Letters, 261(3-4): 375-388.
McCaffrey, K.J.W., Sleight, J.M., Pugliese, S. and Holdsworth, R.E., 2003. Fracture formation and evolution in crystalline rocks: Insights from attribute analysis. Geological Society, London, Special Publications, 214(1): 109-124.
Menand, T., 2011. Physical controls and depth of emplacement of igneous bodies: A review. Tectonophysics, 500(1-4): 11-19.
Mordensky, S.P., Villeneuve, M.C., Kennedy, B.M., Heap, M.J., Gravley, D.M., Farquharson, J.I. and Reuschlé, T., 2018. Physical and mechanical property relationships of a shallow intrusion and volcanic host rock, Pinnacle Ridge, Mt. Ruapehu, New Zealand. Journal of Volcanology and Geothermal Research, 359: 1-20.
Muirhead, D.K., Bowden, S.A., Parnell, J. and Schofield, N., 2017. Source rock maturation owing to igneous intrusion in rifted margin petroleum systems. Journal of the Geological Society.
Müller, G., 1998. Starch columns: Analog model for basalt columns. Journal of Geophysical Research: Solid Earth, 103(B7): 15239-15253.
Ogata, K., Senger, K., Braathen, A., Tveranger, J. and Olaussen, S., 2014. Fracture systems and mesoscale structural patterns in the siliciclastic Mesozoic reservoir-caprock succession of the Longyearbyen CO 2 Lab project: Implications for geological CO 2 sequestration in Central Spitsbergen, Svalbard. Norwegian Journal of Geology/Norsk Geologisk Forening, 94.
Panahi, H., Kobchenko, M., Meakin, P., Dysthe, D.K. and Renard, F., 2018. In-situ imaging of fracture development during maturation of an organic-rich shale: Effects of heating rate and confinement. Marine and Petroleum Geology, 95: 314-327.
Panahi, H., Kobchenko, M., Meakin, P., Dysthe, D.K. and Renard, F., 2019. Fluid expulsion and microfracturing during the pyrolysis of an organic rich shale. Fuel, 235: 1-16.
Perea, D., Schluma, M. and Viloso, J., 1984. Las rocas igneas como reservorio de hidrocarburos, IX Congreso Geológico Argentino, pp. 20-38.

Petford, N., 2003. Controls on primary porosity and permeability development in igneous rocks. Hydrocarbons in Crystalline Rocks, 214(1): 93-107.
Planke, S., Rabbel, O., Galland, O., Millett, J.M., Manton, B., Jerram, D.A., Palma, O.J. and Spacapan, J.B., 2018. Seismic imaging and petroleum implications of igneous intrusions in sedimentary basins constrained by outcrop analogues and seismic data from the Neuquen Basin and the NE Atlantic.
Planke, S., Rasmussen, T., Rey, S.S. and Myklebust, R., 2005. Seismic characteristics and distribution of volcanic intrusions and hydrothermal vent complexes in the Vøring and Møre basins. Geological Society, London, Petroleum Geology Conference series, 6: 833-844.
Planke, S., Svensen, H., Myklebust, R., Bannister, S., Manton, B. and Lorenz, L., 2015. Geophysics and Remote Sensing. In: C. Breitkreuz and S. Rocchi (Editors), Advances in Volcanology. Springer Berlin Heidelberg, pp. 1-16.
Price, L.C., 1983. Geologic time as a parameter in organic metamorphism and vitrinite reflectance as an absolute paleogeothermometer. Journal of Petroleum Geology, 6(1): 5-37.
Pytte, A. and Reynolds, R., 1989. The thermal transformation of smectite to illite, Thermal history of sedimentary basins. Springer, pp. 133-140.
Rassmuss, J., 1923. Breves apuntes geológicos sobre la parte del territorio del Neuquén entre Auca Mahuida y El Tromen. Dirección General de Minas, Geología e Hidrogeología Serie F (informe Prel. y Comunicaciones), Boletín, 6: 15-20.
Rateau, R., Schofield, N. and Smith, M., 2013. The potential role of igneous intrusions on hydrocarbon migration, West of Shetland. Petroleum Geoscience, 19(3): 259-272.
Rodriguez Monreal, F., Villar, H.J., Baudino, R., Delpino, D. and Zencich, S., 2009. Modeling an atypical petroleum system: A case study of hydrocarbon generation, migration and accumulation related to igneous intrusions in the Neuquen Basin, Argentina. Marine and Petroleum Geology, 26(4): 590-605.
Rohrman, M., 2007. Prospectivity of volcanic basins: Trap delineation and acreage de-risking. AAPG bulletin, 91(6): 915-939.
Schiuma, M.F., 1994. Intrusivos del valle del Río Grande, provincia de Mendoza, su importancia como productores de hidrocarburos, Universidad Nacional de La Plata.
Schmiedel, T., Kjoberg, S., Planke, S., Magee, C., Galland, O., Schofield, N., Jackson, C. and Jerram, D., 2017. Mechanisms of overburden deformation associated with the emplacement of the Tulipan sill, mid-Norwegian margin. Interpretation: SK23-SK38.
Schofield, N., Heaton, L., Holford, S.P., Archer, S.G., Jackson, C.A.-L. and Jolley, D.W., 2012. Seismic imaging of 'broken bridges': linking seismic to outcrop-scale investigations of intrusive magma lobes. Journal of the Geological Society, 169(4): 421-426.
Schofield, N., Holford, S., Edwards, A., Mark, N. and Pugliese, S., 2020. Overpressure transmission through interconnected igneous intrusions. AAPG Bulletin, 104(2): 285-303.
Schofield, N., Holford, S., Millett, J., Brown, D., Jolley, D., Passey, S.R., Muirhead, D., Grove, C., Magee, C., Murray, J., Hole, M., Jackson, C.A.-L. and Stevenson, C., 2015. Regional magma plumbing and emplacement mechanisms of the Faroe-Shetland Sill Complex: implications for magma transport and petroleum systems within sedimentary basins. Basin Research: 1-23.
Schofield, N., Stevenson, C. and Reston, T., 2010. Magma fingers and host rock fluidization in the emplacement of sills. Geology, 38(1): 63-66.

Schutter, S.R., 2003. Hydrocarbon occurrence and exploration in and around igneous rocks. In: N. Petford and K.J.W. McCaffrey (Editors), Hydrocarbons in Crystalline Rocks. Geological Society, London, Special Publications, pp. 7-33.

Senger, K., Buckley, S.J., Chevallier, L., Fagereng, Å., Galland, O., Kurz, T.H., Ogata, K., Planke, S. and Tveranger, J., 2015. Fracturing of doleritic intrusions and associated contact zones: Implications for fluid flow in volcanic basins. Journal of African Earth Sciences, 102(0): 70-85.

Senger, K., Millett, J., Planke, S., Ogata, K., Eide, C., Festøy, M., Galland, O. and Jerram, D.A., 2017. Effects of igneous intrusions on the petroleum system: a review. First Break, 35.6: 47-56.

Sidney, P. and Clapp, F.G., 1932. Nature and origin of occurrences of oil, gas, and bitumen in igneous and metamorphic rocks. AAPG Bulletin, 16(8): 719-726.

Silvestro, J. and Atencio, M., 2009. La cuenca cenozoica del río Grande y Palauco: edad, evolución y control estructural, faja plegada de Malargüe. Revista de la Asociación Geológica Argentina, 65(1): 154-169.

Simoneit, B.R.T., Brenner, S., Peters, K.E. and Kaplan, I.R., 1978. Thermal alteration of Cretaceous black shale by basaltic intrusions in the Eastern Atlantic. Nature, 273(5663): 501-504.

Smallwood, J.R. and Maresh, J., 2002. The properties, morphology and distribution of igneous sills: modelling, borehole data and 3D seismic from the Faroe-Shetland area. In: D.W. Jolley and B.R. Bell (Editors), The North Atlantic Igneous Province: Stratigraphy, Tectonic, Volcanic and Magmatic Processes. Geological Society, London, Special Publications, pp. 271-306.

Spacapan, J., Palma, J., Galland, O., Manceda, R., Rocha, E., D'Odorico, A. and Leanza, H., 2018. Thermal impact of igneous sill-complexes on organic-rich formations and implications for petroleum systems: A case study in the northern Neuquén Basin, Argentina. Marine and Petroleum Geology, 91: 519-531.

Spacapan, J.B., D'Odorico, A., Palma, O., Galland, O., Rojas Vera, E., Ruiz, R., Leanza, H.A., Medialdea, A. and Manceda, R., 2020a. Igneous petroleum systems in the Malargüe fold and thrust belt, Río Grande Valley area, Neuquén Basin, Argentina. Marine and Petroleum Geology, 111: 309-331.

Spacapan, J.B., D´Odorico, A., Palma, O., Galland, O., Senger, K., Ruiz, R., Manceda, R. and Leanza, H.A., 2019. Low resistivity zones at contacts of igneous intrusions emplaced in organic-rich formations and their implications on fluid flow and petroleum systems: A case study in the northern Neuquén Basin, Argentina. Basin Research(0).

Spacapan, J.B., Ruiz, R., Manceda, R., D'Odorico, A., Rocha, E., Vera, E.R., Medialdea, A., Cattaneo, D., Palma, O. and Leanza, H.A., 2020b. Oil production from a sill complex within the Vaca Muerta Formation.

Sun, Q., Wu, S., Cartwright, J., Wang, S., Lu, Y., Chen, D. and Dong, D., 2014. Neogene igneous intrusions in the northern South China Sea: Evidence from high-resolution three dimensional seismic data. Marine and Petroleum Geology, 54: 83-95.

Svensen, H., Aarnes, I., Podladchikov, Y.Y., Jettestuen, E., Harstad, C.H. and Planke, S., 2010. Sandstone dikes in dolerite sills: Evidence for high-pressure gradients and sediment mobilization during solidification of magmatic sheet intrusions in sedimentary basins. Geosphere, 6(3): 211-224.

Svensen, H., Corfu, F., Polteau, S., Hammer, Ø. and Planke, S., 2012. Rapid magma emplacement in the Karoo Large Igneous Province. Earth and Planetary Science Letters, 325–326: 1-9.

Svensen, H., Planke, S., Malthe-Sørenssen, A., Jamtveit, B., Myklebust, R., Rasmussen Eidem, T. and Rey, S.S., 2004. Release of methane from a volcanic basin as a mechanism for initial Eocene global warming. Nature, 429(6991): 542-545.
Sydnes, M., Fjeldskaar, W., Løtveit, I.F., Grunnaleite, I. and Cardozo, N., 2018. The importance of sill thickness and timing of sill emplacement on hydrocarbon maturation. Marine and Petroleum Geology, 89: 500-514.
Teixeira, M.G., Donzé, F., Renard, F., Panahi, H., Papachristos, E. and Scholtès, L., 2017. Microfracturing during primary migration in shales. Tectonophysics, 694: 268-279.
Teske, A., Lizarralde, D., Höfig, T., Aiello, I., Ash, J., Bojanova, D., Buatier, M., Edgcomb, V., Galerne, C. and Gontharet, S., 2020. Expedition 385 Preliminary Report: Guaymas Basin Tectonics and Biosphere. IODP Preliminary Report.
Townsend, M.R., 2018. Modeling Thermal Pressurization Around Shallow Dikes Using Temperature-Dependent Hydraulic Properties: Implications for Deformation Around Intrusions. Journal of Geophysical Research: Solid Earth, 123(1): 311-323.
Vega, B., Yang, J., Tchelepi, H.A. and Kovscek, A.R., 2018. Investigation of Stress Field and Fracture Development During Shale Maturation Using Analog Rock Systems, SPE Annual Technical Conference and Exhibition. Society of Petroleum Engineers.
Witte, J., Bonora, M., Carbone, C. and Oncken, O., 2012. Fracture evolution in oil-producing sills of the Rio Grande Valley, northern Neuquen Basin, Argentina. AAPG Bulletin, 96(7): 1253-1277.
Zanella, A., Cobbold, P.R., Ruffet, G. and Leanza, H.A., 2015. Geological evidence for fluid overpressure, hydraulic fracturing and strong heating during maturation and migration of hydrocarbons in Mesozoic rocks of the northern Neuquén Basin, Mendoza Province, Argentina. Journal of South American Earth Sciences, 62: 229-242.
Zeeb, C., Gomez-Rivas, E., Bons, P.D. and Blum, P., 2013. Evaluation of sampling methods for fracture network characterization using outcrops. AAPG Bulletin, 97(9): 1545-1566.
Zhang, W., Wang, Q., Ye, J. and Zhou, J., 2017. Fracture development and fluid pathways in shales during granite intrusion. International Journal of Coal Geology.
Zou, C., 2013. Volcanic reservoirs in petroleum exploration. Newnes.

Appendix: Scientific manuscripts

A.1 Manuscript 1

I

Ole Rabbel, Palma, J. O., Mair, K., Galland, O., Spacapan, J. B., Senger, K.
Fracture networks in shale-hosted igneous intrusions:
Processes, distribution, and implications for igneous petroleum systems.
Journal of Structural Geology (in press; published online on 21.06.2021)

Fracture networks in shale-hosted igneous intrusions: Processes, distribution, and implications for igneous petroleum systems

Ole Rabbel[a,*], Octavio Palma[b], Karen Mair[a], Olivier Galland[a], Juan B. Spacapan[b], Kim Senger[c]

[a] Physics of Geological Processes, The NJORD Centre, Department of Geosciences, University of Oslo, Box 1047, Blindern, 0316, Oslo, Norway
[b] YTEC, Av. Del Petroleo s/n – 129 y 143, 1925 Berisso–Buenos Aires, Argentina
[c] Department of Arctic Geology, University Centre in Svalbard, Box 156, 9171 Longyearbyen, Norway

*corresponding author: ole.rabbel@geo.uio.no

Keywords: Igneous intrusions, fracture network characterization, petroleum systems, fractured reservoirs, fluid migration, Neuquén Basin

Abstract

Igneous intrusions in sedimentary basins can influence basin-scale fluid flow and petroleum systems in various ways. They may act as barriers, preferential pathways or even reservoirs for fluids. The fracture networks of intrusions usually represent the main control of their hydraulic properties. However, our understanding of different fracturing mechanisms and their quantitative effect on fracture network properties remains limited, and good field examples are sparse. Here, we present a comprehensive field study from the Neuquén Basin, Argentina, using a reservoir-scale outcrop of a sill complex emplaced in organic-rich shale, which constitutes a direct analogue of oil-producing fractured igneous reservoirs. We provide field evidence of various fracturing mechanisms affecting the fracture network, including cooling joints, bituminous dykes, hydrothermal veins, and tectonic faults. Using high-resolution digital fracture network quantification, we then tie these fracture mechanisms to spatial variations of fracture orientation, intensity, and connectivity. Our results indicate that all observed fracture types are involved in hydrocarbon migration and/or storage. Bitumen of very high thermal grade within the intrusions implies migration of hydrocarbons into the sills in a destructive high-temperature environment. Importantly, bitumen dykes and faults locally alter the fracture network, creating zones of strongly increased fracture intensity and connectivity and therefore improved reservoir properties.

1. Introduction

Igneous intrusions are present in many sedimentary basins around the world. Their potential effects on geological processes and properties in the subsurface are widely recognized both on the local and regional scale. These effects include for instance accelerated chemical reactions (e.g. organic matter maturation) in the surrounding metamorphosed host rock and altered hydraulic properties, with consequences for groundwater exploration, CO2 sequestration and petroleum systems (Schutter, 2003; Senger et al., 2017), but also global climate change in the geological past (Iyer et al., 2017; Svensen et al., 2004).

With respect to fluid flow, igneous intrusions may act as barriers (Rateau et al., 2013), or alternatively, preferred pathways or even reservoirs (Mao et al., 2020; Rodriguez Monreal et al., 2009; Senger et al., 2015; Spacapan et al., 2020), and may thus be of great importance for basin-scale flow patterns and hydrocarbon accumulations. Due to the typically low primary porosity of intrusions, fracturing represents a key factor controlling the overall hydraulic properties of igneous intrusions (Heap and Kennedy, 2016; Senger et al., 2017; Witte et al., 2012). Specifically for igneous intrusions acting as hydrocarbon reservoirs, fracture networks represent the main contributors to both porosity and permeability that allow storage and production in the first place (Delpino and Bermúdez, 2009; Senger et al. 2017). However, there is no consensus on the relative importance of different fracturing mechanisms for establishing pathways or storage capacity for fluids, or their effect on quantifiable fracture network properties.

Cooling joints constitute the most obvious element of the fracture network in igneous intrusions and are commonly believed to provide most of the fracture porosity and permeability in intrusions (Delpino and Bermúdez, 2009; Gudmundsson and Løtveit, 2014; Witte et al., 2012). Additionally, qualitative fracture evolution models often propose that fault-related fracturing and re-opening of cooling joints, as well as hydrothermal veins may enhance permeability (Spacapan et al., 2020; Witte et al., 2012). Hydraulic fracturing due to fast maturation of organic-rich shales surrounding igneous intrusions is a well-recognized process (Aarnes et al., 2012; Zanella et al., 2015), but the potential fracturing of the intrusions themselves has been largely ignored. Although these existing models generally seem reasonable, there is an acute lack of published observational evidence of the specific fracturing mechanisms at play, and particularly their involvement in the hydrocarbon-bearing fracture porosity of igneous reservoirs.

Volcanological outcrop studies on cooling joints in intrusions propose a characteristic joint size depending on cooling rate, magma chemistry and intrusion geometry (Goehring and Morris, 2008; Hetényi et al., 2012). Others suggest power-law (i.e., scale-independent) behavior for several fracture parameters (length, aperture, orientation) for outcrop analogues of oil-bearing sills and assume laterally consistent fracture network properties (Witte et al., 2012). Connectivity is often believed to be high in cooling-joint networks, but this statement is frequently provided without quantitative evidence, particularly in the context of igneous reservoirs (Delpino and Bermúdez, 2009; Gudmundsson and Løtveit, 2014; Witte et al.,

2012). Significantly, the existing models fail to address the strongly varying effect of igneous intrusions on fluid flow and storage. This has been reported both on the global scale (barrier vs. pathway, Senger et al., 2017) and locally, e.g., for intrusions acting as hydrocarbon reservoirs in the northern Neuquén Basin, Argentina, which exhibit strong lateral variations in their hydraulic properties (Spacapan et al., 2020, A. Medialdea, pers. comm.). Thus, additional work is required to quantify fracture network properties in igneous intrusions and document lateral variations. Specifically, there is a pressing need to link this quantification to the underlying fracturing processes in order to improve our understanding of the fracture network evolution and potential causes of the observed hydraulic property variations of igneous intrusions.

Here, we present a comprehensive field study from the Neuquén Basin, Argentina, using a reservoir-scale outcrop of a sill complex emplaced in organic-rich shale, which constitutes a direct analogue of oil-producing fractured igneous sills. We show explicit field evidence of the wide spectrum of fracture types and mechanisms affecting the fracture network of an igneous intrusion emplaced in organic rich shale and combine this with high-resolution digital fracture network quantification over more than 200 meters. Our aims are (1) to provide sound evidence for the broad range of fracture types contributing to the accessible fracture network of igneous sills potentially acting as reservoirs, and (2) to quantify local variability in the fracture network parameters arising from the presence, or absence, of these fracture mechanisms. Thereby, we aim at providing new insight into fracture network evolution within igneous intrusions, with a specific focus on settings where the host rock is organic-rich shale.

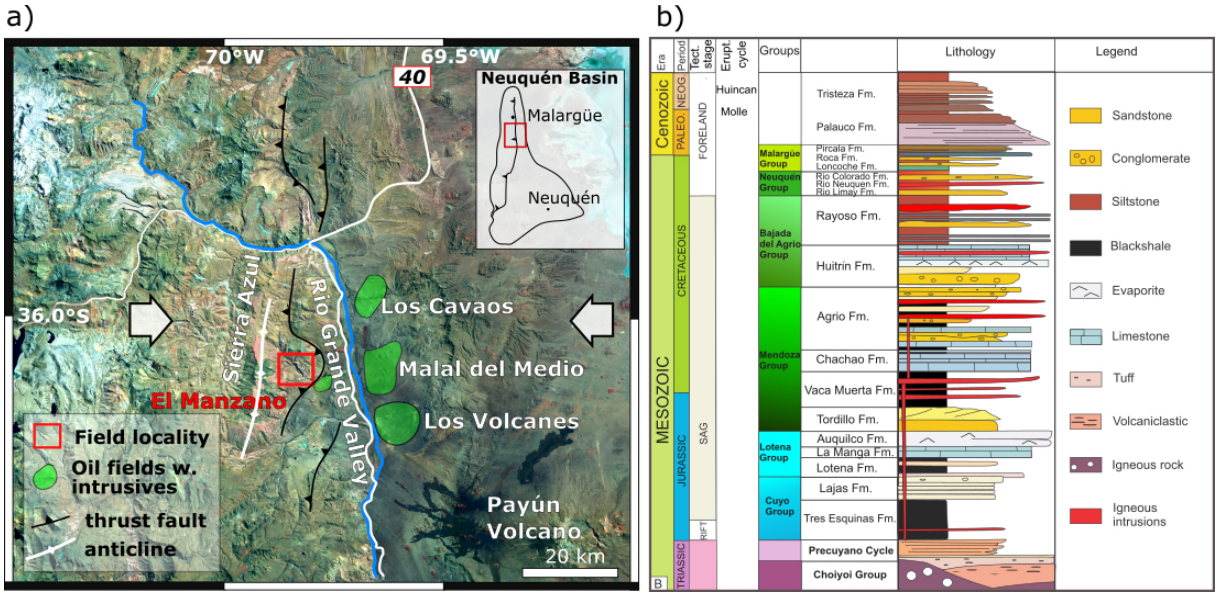

Figure 1. (a) Satellite image of the study area in the Sierra Azul range, adjacent to the producing fractured igneous reservoirs of Rio Grande Valley, with indicated Andean E-W compressive stress regime. (b) Regional tectono-stratigraphic framework (modified from Spacapan et al., 2020).

2. Geological setting

The study area is located in the Sierra Azul range in the northern Neuquén Basin, Argentina, around 70 km south of the town Malargüe (Figure 1a). The Neuquén Basin represents one of the Andean foreland basins and comprises a prolific hydrocarbon province with various proven hydrocarbon plays, including commercial oil production from fractured andesitic sills emplaced in organic-rich shales (Howell et al., 2005; Spacapan et al., 2020).

The geodynamic evolution of the basin comprises three main phases (Figure 1b). Initiation of the basin started in the Triassic-Jurassic as a series of elongated rifts forming isolated depocentres (Howell et al., 2005; Yagupsky et al., 2008). During the early Jurassic period, it subsequently transformed into a back-arc basin dominated by regional thermal subsidence following the onset of the Andean subduction. This phase lead to formation of the marine sediments of the Mendoza group, which include organic-rich shales of the Vaca Muerta and Agrio formations (Bettini and Vasquez, 1979; Manceda and Figueroa, 1995) that constitute two of the main source rocks of the basin. In the late Cretaceous, the tectonic regime changed to compressive, initiating the foreland basin phase. This stage created a series of fold- and thrust belts including the Malargüe fold-thrust belt through reactivation and inversion of the Rift-related normal faults as well as older basement faults (Manceda and Figueroa, 1995). The outcropping El Manzano sill complex described on this study was brought to surface during this phase and is located adjacent to one of these inverted halfgrabens, the El Manzano-Liu Cullín lineament (Yagupsky et al., 2008).

During the foreland basin stage, particularly the northern part of the Neuquén Basin experienced two main pulses (late Oligocene to Miocene; late Miocene to Pliocene) of extensive volcanism and magmatic intrusion of the sedimentary succession (Combina and Nullo, 2011; Kay et al., 2006). This magmatism profoundly affected the petroleum systems in several ways. First, it provided the necessary heat to generate hydrocarbons from the Vaca Muerta and Agrio formations, which are mainly immature in the study area as shown by thermal modeling and geochemical analysis (Spacapan et al., 2018). Secondly, it generated intrusions that themselves act as naturally fractured reservoirs, constituting atypical petroleum systems such as the Rio Grande Valley (RGV) oil fields (Witte et al. 2012; Spacapan et al., 2020). The El Manzano sill complex presented in this study represents a direct outcrop analogue of the RGV petroleum system, as it is located just 10 km west of the oil fields, separated by a major thrust fault (Figure 1a). The El Manzano outcrop features an exposed seismic-scale sill complex emplaced within the Agrio and Vaca Muerta formations, with interconnected andesitic intrusions of 1-20m thickness (Figure 2). Ar-Ar dating yields an age of 14 Ma for one of the sills at El Manzano (see supplementary data). This outcrop is spectacular not only due to its function as a direct analogue outcrop, but because it's continuous high-quality exposure for several kilometers allows studies ranging from the scale of seismic surveys (e.g., Rabbel et al., 2018) to detailed outcrop investigations.

Some 5 km from the El Manzano sill complex, Borello (1944) first described outcrops of solid bitumen. Dykes and sills of bitumen (also termed "asphaltene") are common in the northern Neuquén Basin and have been mined extensively (e.g., Cobbold et al. 1999). Their

formation is linked to fracturing and short-distance migration in response to fluid overpressure (Parnell and Carey 1995). The causes of overpressure formation have been debated for decades and are still uncertain, but strong heating pulses during phases of volcanism have repeatedly been proposed, because bitumen occurrence clusters around volcanic centers and the heat may trigger fast maturation and overpressure build-up (Rassmuss, 1923; Cobbolt et al., 2014; Zanella et al., 2015).

3. Data and Methods

3.1. Field documentation, samples and geochemical analyses

The observations and data presented in this study where obtained during two campaigns totaling six weeks of fieldwork at the El Manzano outcrop, including exploration as well as detailed sampling (Figure 2). In addition to the overall architecture of the sill complex, we focused on documenting the wide range of fracture types observed throughout the locality. This included drone surveys (DJI Phantom 3), field photographs, manual structural measurements of fault, fracture and bedding planes. We also collected 27 samples of different types of veins for hand sample and thin section descriptions, as well as Raman spectroscopy and qualitative conductivity measurements using a handheld multimeter setup to constrain the thermal alteration of organic matter in terms of potential graphitization (sample locations indicated in Figure 2). Since solid, low-maturity bitumen is an insulator but graphite is an excellent conductor, any measurable conductivity in dry samples should indicate significant graphitization. Raman spectroscopy includes analysis of the positions and intensities of the spectral peaks at 1345 cm^{-1} and 1585 cm^{-1}, termed D ("disorder") and G ("graphite") peaks, respectively (Potgieter-Vermaak et al., 2011). For samples undergoing initial thermal alteration (prior to long-term thermal metamorphism), the G peak narrows and shifts towards 1615 cm^{-1} with increasing alteration but shifts back to ca. 1598 cm^{-1} if graphite is formed (Muirhead et al., 2012). Experimental investigations of short, intense heating of meteorite and immature bitumen samples indicate a rise in the peak intensity ratio I_D/I_G from around 0.6 to around 1, which may be used to investigate settings involving local heating due to igneous intrusions (Muirhead et al., 2012; Zhou et al., 2014).

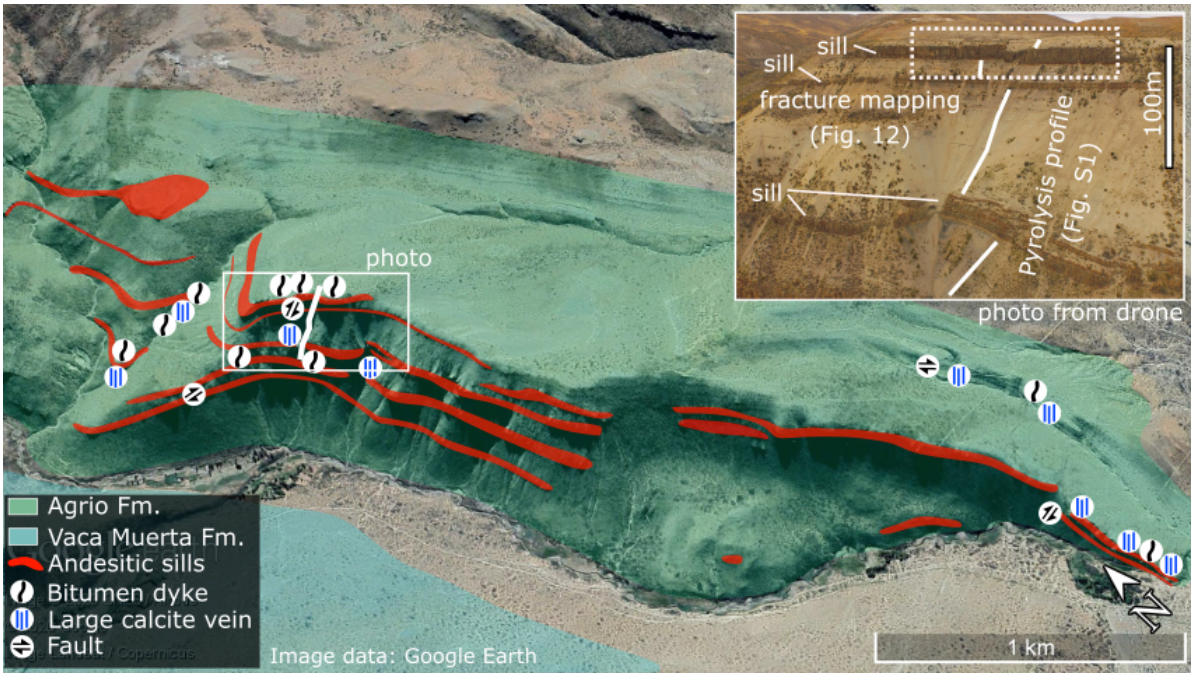

Figure 2. 3D view of the El Manzano sill complex (intrusions indicated in red), along with a wide-angle drone photograph (insert), demonstrating the outcrop scale and relevant locations of data presented in this study. Apparent clustering of features and absence in parts of the outcrop results from targeted field campaigns.

Along a sub-vertical section through the main outcrop cliff (white lines in Figure 2), we analyzed 16 shale samples using Rock-Eval pyrolysis. This is a standard tool to evaluate the realized and overall hydrocarbon generation potential of source rocks, and thus routinely used in the petroleum industry (e.g., Lafargue et al., 1998). RockEval serves as an indicator of thermal maturity and type of organic matter and is commonly used to quantify the maturation effect of igneous intrusions on organic-rich shale (Aarnes et al., 2011; Einsele et al., 1980; Spacapan et al., 2018). During pyrolysis, samples are heated to several hundred degrees in a stepwise process to identify the amount of free hydrocarbons (S1 peak), the remaining hydrocarbon potential (S2 peak), oxygen index (OI), total organic carbon (TOC) and hydrocarbon index (HI) (Espitalié et al., 1985). HI is calculated as S2 / TOC x 100, yielding milligrams of hydrocarbons per gram of organic matter. Assuming initial HI from immature samples or literature values, this is used to calculate the transformation ratio (TR) of organic matter into hydrocarbons.

3.2. Fracture network quantification

This study aims to quantify potential lateral changes in fracture network parameters in response to the evidence of different fracture processes observed in the field. In addition to manual 1D scanlines for ground-truthing (Guerriero et al., 2010), we collected drone-based and handheld imagery to obtain high-resolution 3D digital outcrop models and orthophotographs from a selected outcrop location (Figure 2) using structure-from-motion (e.g., Westoby et al., 2012). Augmenting the previously created large-scale, decimeter-resolution 3D model to interpret large-scale sill geometries (presented in Rabbel et al., 2018), the new 3D model allows mapping of fractures down to the sub-cm scale over a 230 x 20 m outcrop section. The model was georeferenced relative to the existing differential GPS-referenced large-scale model, leading to an integrated digital outcrop dataset across the scales.

In addition to collecting manual data, we extracted 3D plane orientation data of fracture planes along digital scanlines using the Lime software package (Buckley et al., 2019). Scanlines run both parallel and orthogonal to the intrusion boundary in order to minimize scanline orientation bias. This also exemplifies the benefit of digital outcrops in fracture mapping, as manual collection of fracture plane data from the inaccessible cliff in the intrusion center was not feasible. Note that for digital plane measurements, we used models with significantly higher mesh resolution compared to standard visualization purposes to avoid erroneous measurements resulting from smoothing of the digital outcrop surface. All fracture plane orientations were corrected for local dip of the surrounding sedimentary layers.

As a key element of the fracture network characterization, we generated an ultra-high resolution (down to 3 mm/pixel) orthorectified photograph of a 230 m outcrop section with exceptional outcrop quality and with many observations evidencing the presence of different fracturing processes (Figure 2). We used the orthophotograph to manually pick 2D fracture trace maps, which subsequently served as input for automated fracture network analysis using the FracPaQ Matlab toolbox (Healy et al., 2017). This software provides comprehensive measurements and estimates of fracture network properties, including fracture density and intensity, connectivity, trace and segment length distributions, as well as 2D orientation distribution of the fracture network. 2D fracture density and intensity, commonly termed P20 and P21 (e.g., Zeeb et al., 2013), represent number of fractures and length of fractures per unit area, respectively, and are measured here using the circular estimator method (Healy et al., 2017). Similar to the P10 value for 1D fracture intensity, commonly obtained from scanlines, P21, in particular, serves as an estimate for the fracture area per unit volume (P32), which is a critical input in fracture network modeling controlling the number of fractures in a model.

Connectivity of fracture networks is quantified using the network topology in terms of relative abundance of node types, i.e. crossing (X-node), abutting (Y-node) and isolated termination (I-node). Note that any 2D mapping of fractures aimed at quantifying connectivity therefore needs to take care to correctly map fracture connections corresponding to the observed node types. For a given number N of X-,Y- and I-nodes, we get the average number of connections per line as $C_L = \frac{4*(N_X+N_Y)}{N_I+N_Y}$ (Sanderson and Nixon, 2018). We calculated C_L along a moving window of 35 m width that was shifted by 15 m, yielding a continuous curve of 15 connectivity values along the outcrop, each allocated to the position of the center of the window.

Finally, the FracPaQ provides a Maximum-Likelihood-Estimator (MLE) test to assess the likelihood of observed trace lengths being drawn from a (i) power-law, (ii) log-normal or (iii) exponential distribution (Rizzo et al., 2017). Thereby we aim to (1) avoid misleading results for length distribution characteristics from a wrong initial assumption, and (2) gain insight into how different fracture processes may alter the fracture length distribution. We performed this analysis in three manually selected subsets of the fracture network, according to outcrop-based observations of distinct processes, i.e., we separated the central area affected by a fault and bitumen dykes from the outer areas dominated by cooling joints. In order to account for potential truncation bias when fitting a power-law, we applied a lower cutoff according to the

recommendations of Bonnet et al. (2001), while we did not apply an upper cutoff, because the intrusion gives a natural upper length limit through its size.

As a trade-off between data size and quality, we integrated two different drone surveys conducted from slightly varying distance to outcrop, resulting in different resolutions of 3 and 12 mm/pixel, respectively. This can be problematic, as the recorded number of fractures is often subject to resolution bias (Zeeb et al., 2013). However, we justify our approach by comparing digital results to manual scanlines (ground-truthing) and considering on-site outcrop observations (cf. supplement S1). Comparison of manual fracture density measurements with values from digital data in areas of lower resolution found the values to be identical, i.e. we do not expect significant resolution bias at the lower end of the scale. These areas show no signs of tectonic deformation or natural hydraulic fracturing, with small-scale fracturing absent upon inspection in the field. Where these processes are in fact present, we have high-resolution data available and are thus able to map smaller fractures, but without compromising comparability of the overall fracture data.

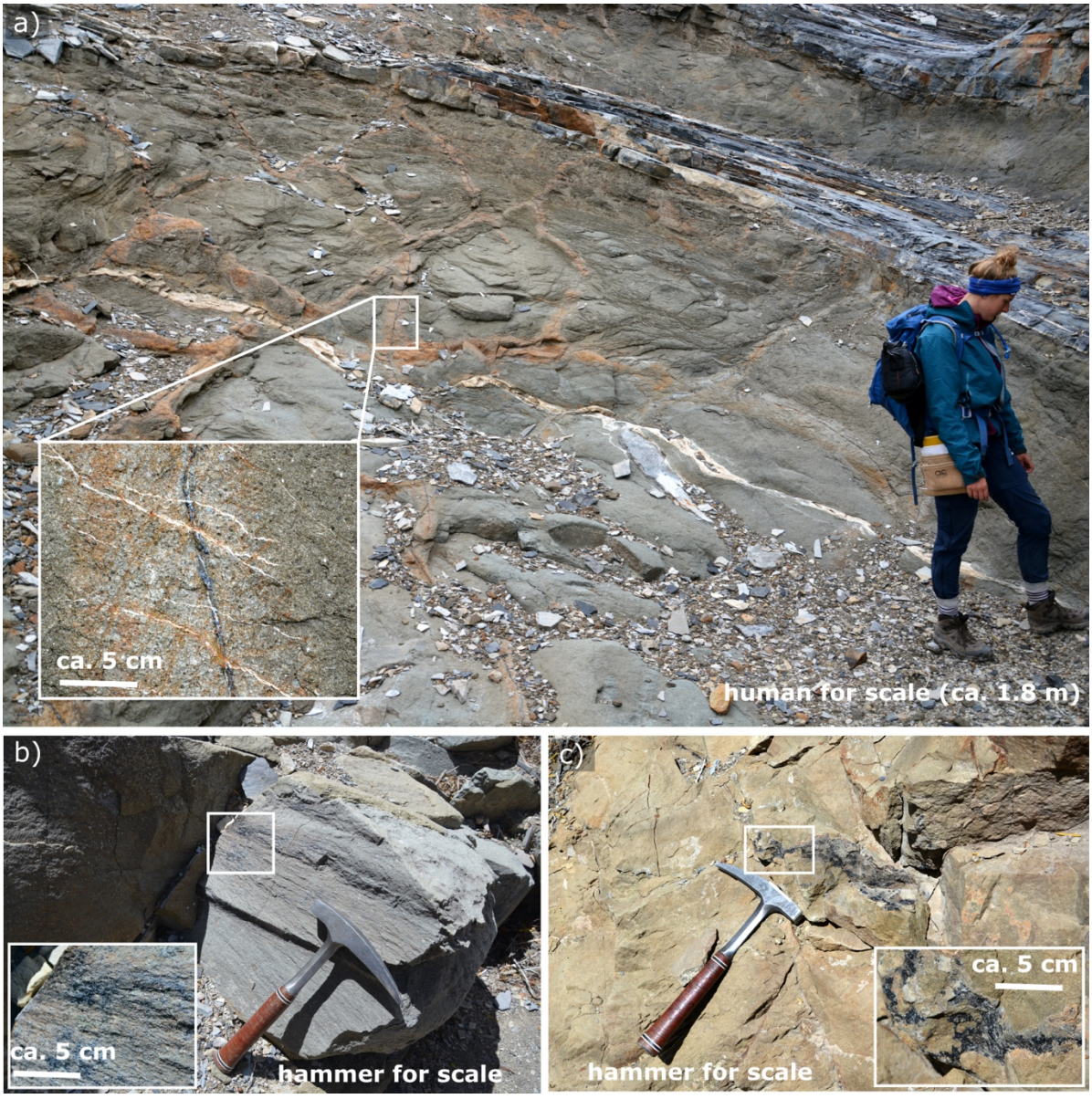

Figure 3. Examples of cooling joints within intrusions. (a) intrusion roof with polygonal joint arrangement (see red weathering along surfaces), with fractures showing alteration and black and white fill (calcite and bitumen, see close-up). (b) Joint surface with plumose structure impregnated with shiny bituminous material, (c) irregular joint surface with bitumen.

4. Results

4.1. Fracture types

4.1.1. Cooling joints

As can be expected for thin sheet intrusions within a fold-thrust belt, we observe that the intrusions display strong, though not homogenous, jointing. Note that without additional observations (e.g., polygonal arrangement or orientation relative to intrusion-host contact), it is inherently difficult to distinguish cooling joints from tectonic joints. Therefore, some of the observed jointing may be of tectonic nature or at least may have formed in a stage of active

compressive tectonics. However, since some additional observations are available and cooling joints represent a ubiquitous feature of igneous sheet intrusions, we refer to the observed joints as cooling joints.

Figure 3 shows examples of cooling joints with bitumen filling or impregnation of their fracture surfaces. This is frequently found within intrusions at El Manzano. We occasionally observe polygonal joint arrangement typical of cooling joints, especially in places where the roof of an intrusion is exposed (Figure 3a). In addition, the polygonal fracture planes are filled with a mixture of black and white material, identified as solid organic matter and calcite, respectively (Figure 3a, close-up). In some cases, the joints exhibit plumose structures (Figure 3b). The solid bitumen filling shows no evidence of leftover volatiles and instead appears as either a shiny black powder or bitumen (Figure 3b, c).

4.1.2. Bituminous injection structures

Throughout the El Manzano sill complex, we observe large structures of injected bitumen or bituminous material within and around intrusions (Figures 4 and 5; see Figure 2 for sampled localities). Note that throughout this work, we use the term "bitumen" if veins or joints are filled or impregnated with pure bitumen, while "bituminous" describes observations where such fillings are impure (e.g. mixed with shale) or we are unsure of the exact nature of the organic matter. These injection structures occur in the form (1) arrays of pure bitumen dykes with observed individual sizes of up to ca 20 m height and 50 cm width (Figure 4a, b), or (2) areas of intense and chaotic fracturing, where fractures are filled with a mixture of bitumen, shaly material and/or calcite (Figure 5). These spectacular features are localized around the sills and originate in the aureoles from where they may extend far into the igneous bodies (Figure 4a). We do not observe such dykes outside of the direct vicinity of an intrusion or its aureole, i.e. they do not seem to cut the stratigraphy over more than 10-20 meters. On closer inspection, the dykes consist not of a single mass, but several branches, which may also cut across each other (Figure 4b, c). In other cases, the dykes can mingle with thick calcite veins (see section 4.2.3), typically without a clear crosscutting relationship (Figure 4d, e). While we did not find an exposed root of a pure bitumen dyke, the shale-bitumen filled fractures displayed in Figure 5 appear to originate directly from the contact zone, where we observe meter-scale cavities due to missing host rock (Figure 5a, b).

The zones around such injection structures are intensely fractured and host large amounts of mobilized organic matter. While the fractured intrusive rock around the injection structure hosting bitumen-shale mixture disintegrates so readily that sampling is impossible (Figure 5c), we were able to collect several samples of the more solid bitumen dykes (e.g. Figure 4d, f, g). The hand sample shown in Figure 4d displays mingling of cm-scale calcite and bitumen veins within intrusion. In addition, we observe that the bituminous material in many of the dykes has a shiny, fibrous, crystalline-looking appearance (Figure 4f). In some of the samples, we found shale fragments and calcite crystals of millimeter to centimeter size in the bituminous matrix of such dykes (Figure 4g). Note that due to the crosscutting of different types of veins, it is not always possible to keep the description of these features fully separated.

Figure 4. Photographs of bitumen dykes from field and hand samples. (a) Large bitumen dyke crosscutting the intrusion-host rock contact and branching within the intrusion. (b) Bitumen dyke array within a metamorphic aureole. (c) Internal structure of the dyke shown in (a) with multiple fibrous dykelets. (d, e) Intermingling calcite and bitumen veins in a hand sample and at outcrop scale, respectively. (f) Fibrous, shiny sample of a bitumen dyke. (g) Calcite crystals and shale pieces entrained in the matrix of a bitumen dyke sample.

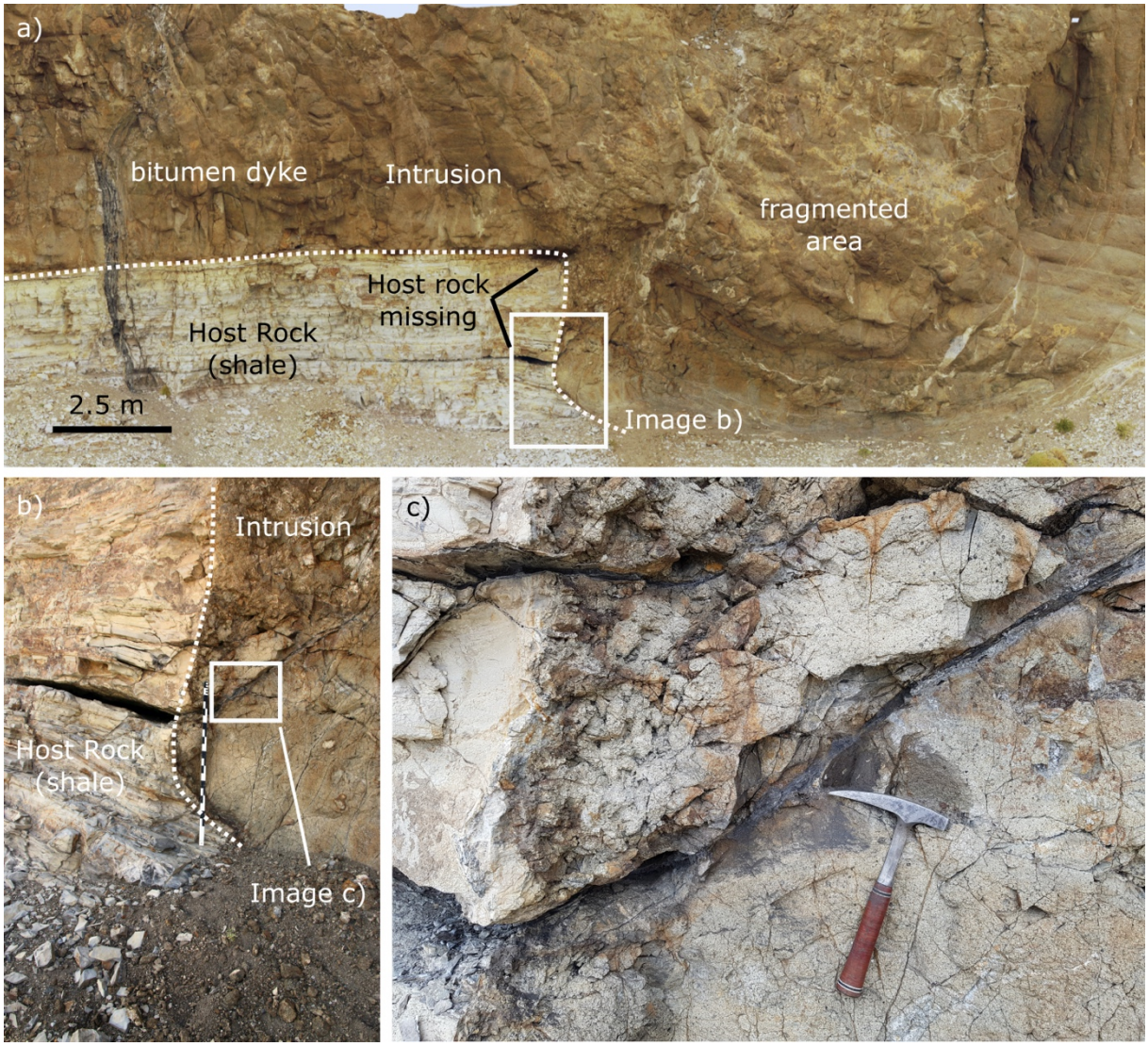

Figure 5. Bituminous shale injection structure. (a) Drone-based virtual model showing the sill geometry and spatial relation of the fractures and holes in the host rock. (b,c) Field photographs illustrating the missing host rock as the apparent origin of a large fracture filled with black material, surrounded by an intensely fractured zone.

Figure 6 depicts Raman spectra of three bitumen samples collected from intermingling bitumen and calcite veins in the southern part of El Manzano. All spectra show clear disorder and graphite peaks, of which the graphite peaks at around 1585 cm^{-1} are particularly well developed. Peak intensity ratios I_D/I_G lie between 0.85-0.93. In addition, qualitative conductivity measurements indicate that dry bitumen samples with fibrous and shiny appearance conduct electrical currents.

RockEval pyrolysis provides results for thermal maturity of the Agrio formation at the El Manzano outcrop (Figure 7). Assuming initial HI of 538 mg/g corresponding to the observed maximum value, our analysis indicates 0-20% transformation of organic matter in the parts of the section that are least affected igneous sills, while the aureole of the sills clearly shows increased transformation of up to 99% close to the sills, where injection structures are found.

Note that other authors report lower initial HI in the area (e.g., Spacapan et al., 2018), which would lead to even smaller TR, especially in the less affected regions.

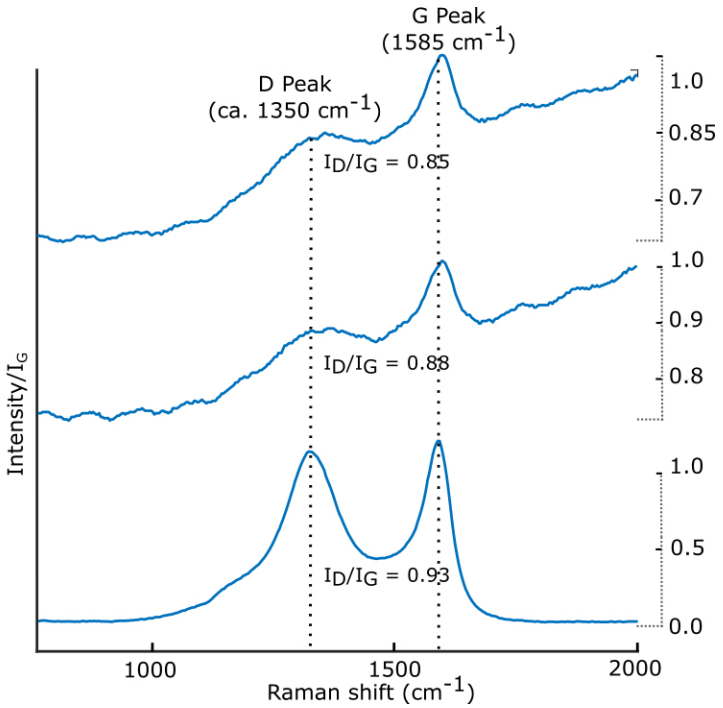

Figure 6. Raman spectra of bitumen obtained from samples of intermingling calcite and bitumen veins within the sills in the southern part of the outcrop (cf. Fig. 2).

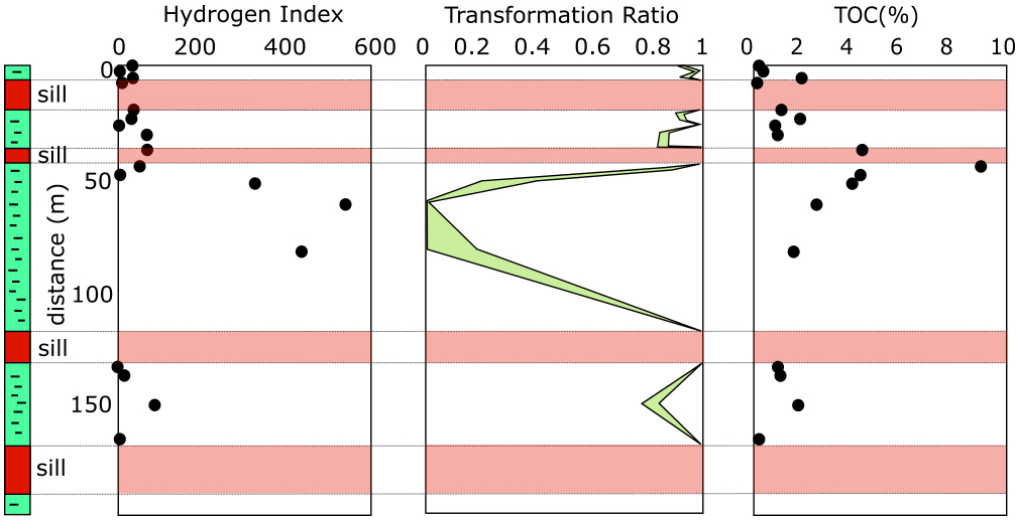

Figure 7. Hydrogen index (HI), transformation ratio (TR) and TOC profile from Pyrolysis transect through the intruded Agrio formation. Green area represents lower and upper TR estimates based on reference values from Spacapan et al. (2018) and local maximum as the initial HI, respectively.

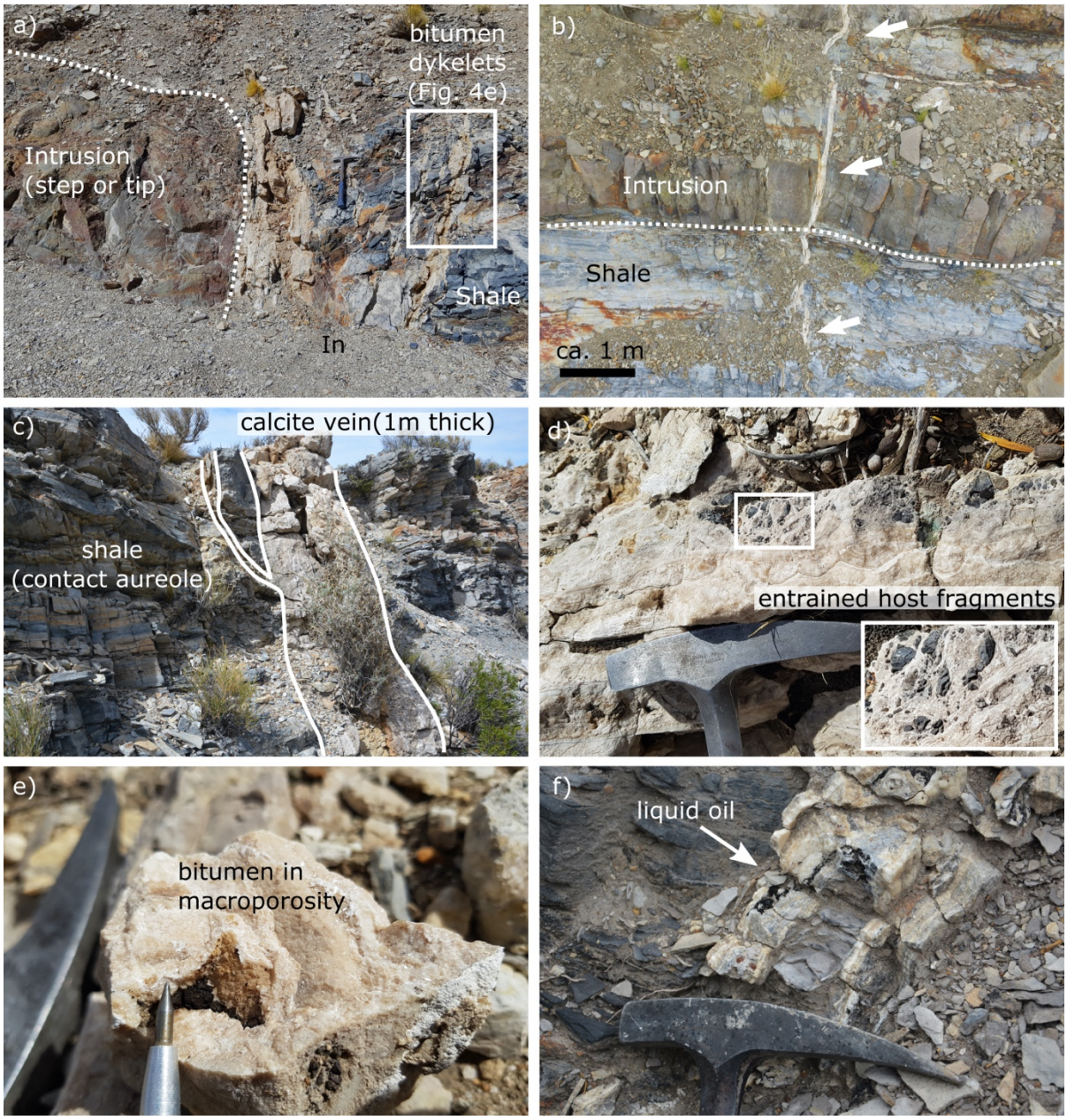

Figure 8. Large calcite veins in the field. (a) Intermingling calcite veins and bitumen dykelets at an exposed intrusion tip. (b) Drone based photograph showing a ca. 10 cm thick calcite vein cutting through aureole and sill. (c, d) Large, 1 m thick vein cutting the contact aureole of a sill with entrained host rock pieces. (e) Sample of a vein with bitumen occupying a cm-scale pore. (f) Calcite vein containing oil stains.

4.1.3. Hydrothermal calcite veins

Throughout the outcrop, we find many large carbonate veins cutting through both aureole and sills, that are distinctly different from calcite-filled cooling joints, and also show no signs of shear displacement (Figure 8). The veins occur both at sill tips, and along the more central part of sills and may crosscut, or be crosscut by, bitumen dykes (Figure 8a, b, also Figure 5e). Commonly, these features are several centimeters to a meter wide, tens to hundreds of meters long, and include arrays of branching veins (Figure 8a, c), and carry fragments of host rock

(Figure 8d). Millimeter- to centimeter-scale macropores like the one displayed in Figure 8e are very common and often filled with bitumen, and release a strong hydrocarbon smell when broken up. Fluid inclusions with CO2 were identified using Raman spectroscopy (supplement S2). Occasionally, we find stains of highly viscous oil within the veins (Figure 8f).

4.1.4. Faults and associated damage zones

Although the El Manzano outcrop is located in the hanging wall of the major thrust front of Sierra Azul range, faulting within the outcropping sill complex is limited to small-scale strike-slip and thrust faults cross-cutting the sills, as summarized in Figure 9. Displacement along these faults typically is on the centimeter to meter range and locally causes enhanced fracturing in the form of damage zones. These damage zones commonly feature fractures filled with solid bitumen and low-viscosity, strongly degraded oil as well as calcite veins (Figure 9b-d). Figure 9c shows an example of a bitumen-filled fracture cross-cutting an amygdale partly filling primary vesicular porosity. Figure 9e presents an example of a small-scale thrust fault cutting a sill and the surrounding sediments, which also contain bedding-parallel calcite veins. Despite the small extent of this fault, its core hosts a damage-zone filled with massive calcite veins that (1) show striations indicating shear movement and (2) release strong hydrocarbon odor when broken up.

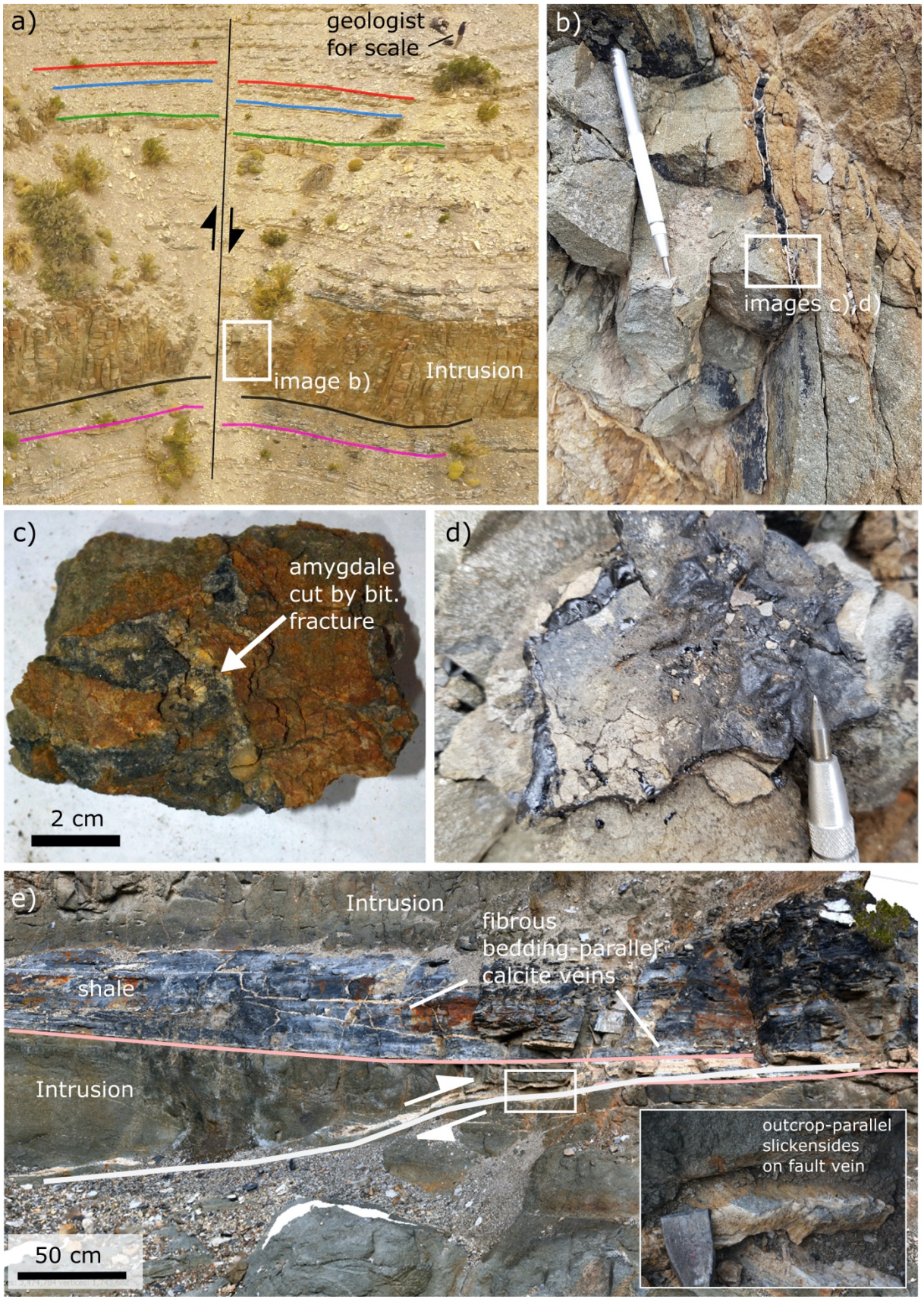

Figure 9. Examples of faults and associated damage zones observed at El Manzano. (a) Oblique strike-slip fault evident in a drone-based virtual outcrop model. (b) Field photograph of the damage zone associated with the fault displayed in image (a). (c, d) Hand samples showing bitumen and oil-filled fractures in the same damage zone. (e) Small thrust in a sill comprising a damage zone with thick calcite veins. Note also bedding-parallel calcite veins in the shale between the two intrusions.

4.2. Lateral variability of the fracture network

4.2.1. Orientation patterns of fracture types

As the first step of a quantitative description of the variability of fracture types and their distribution, we provide dip-corrected plane orientations of different fracture types collected throughout the El Manzano sill complex (Figure 10). Cooling joint data show predominantly vertical to subvertical planes. Despite a generally large spread in azimuths, there exists some agreement with the orientation of the main tectonic structures of the Sierra Azul range in the form of one E-W striking set and two conjugate NE-SW / NW-SE striking sets. Fault plane orientations show a NNE-SSW striking reverse fault and two ESE-WNW striking strike-slip faults, of which one is slightly oblique and has a reverse-fault component (cf. Fig 9a). Bitumen dykes are characterized by vertical to subvertical dip and a pronounced preferred orientation in N-S and E-W direction, and thus with the large-scale tectonic structures. Orientations of the predominantly vertical hydrothermal calcite veins comprise one strong E-W striking set, but the remaining plane measurements spread over a wide range of orientations.

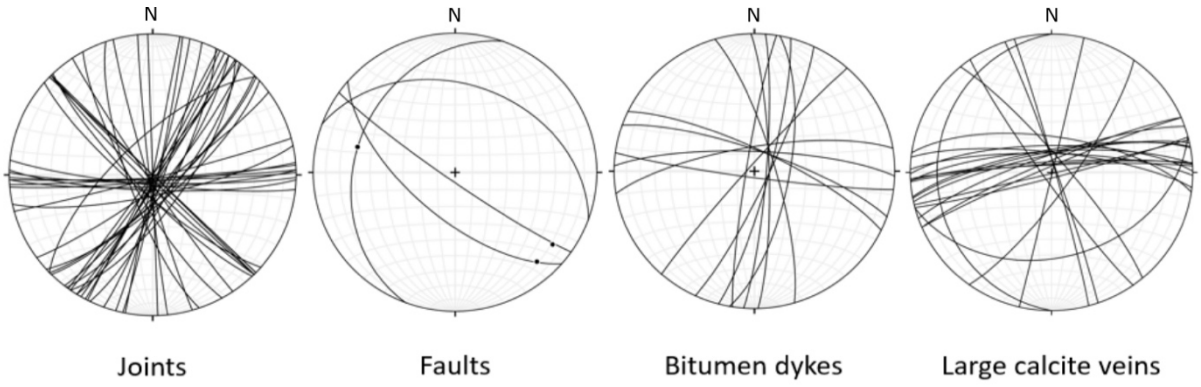

Figure 10. Dip-corrected orientation data of fracture and fault planes sorted by fracture type (Schmidt equal-area projection).

4.2.2. Influence of sill architecture and structural features

Overall, we observe that fracture patterns change notably with sill architecture and geometry. Although a full documentation of the sill complex architecture and geometries found at El Manzano and their influence on the fracture network is beyond the scope of this work, the example in Figure 11 qualitatively illustrates some key effects. The digital outcrop model illustrated in Figure 11 is located in the northern part of the outcrop and comprises amalgamated and stacked sills of varying thickness. The massive sill in the lower left of Figure 11 is approximately 11 m thick and terminates in this location, where the sill tip is visible. It comprises few, long subvertical joints as well as radial joints, which are characteristic for sill tips (see e.g., Galland et al., 2019). On the other hand, the even thicker sill on the right side consists of four stacked intrusions, which are distinguished through different weathering colour, clear horizontal contacts, and occasionally even thin lenses of

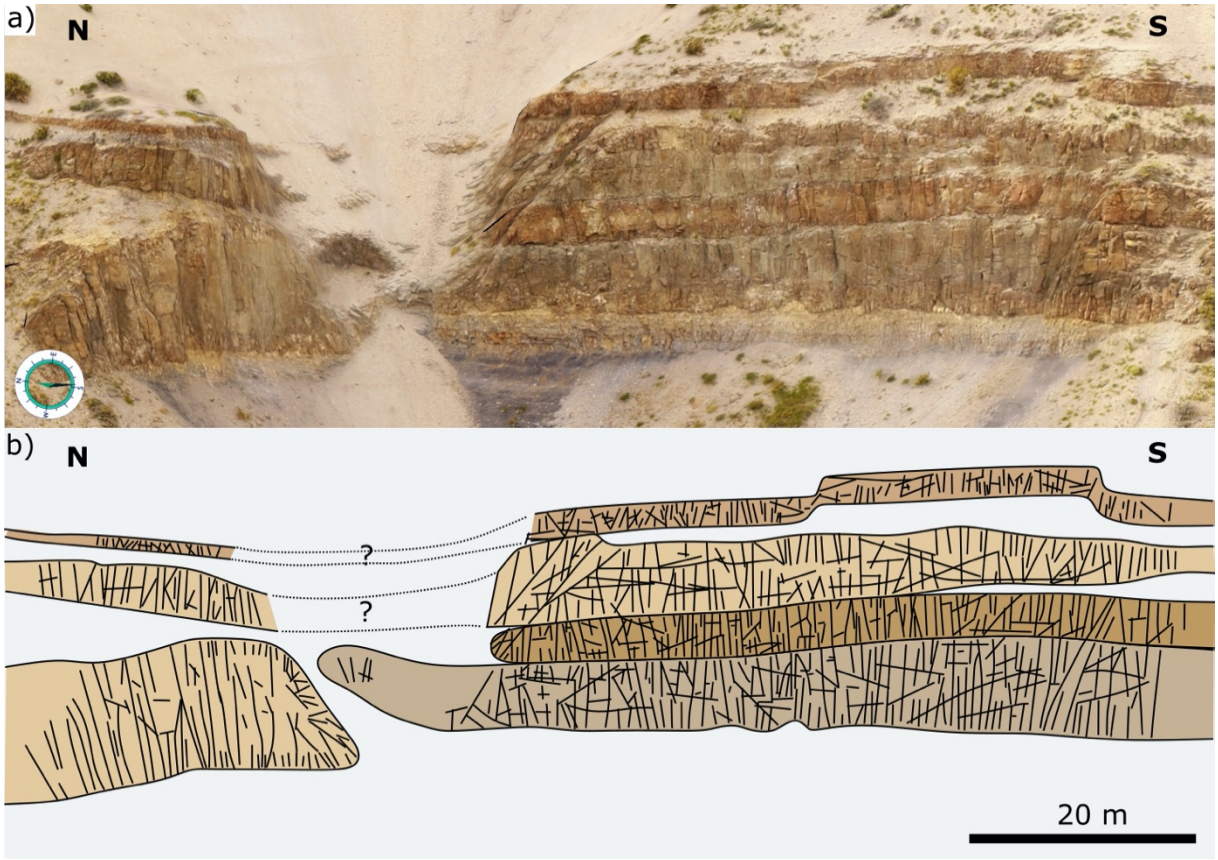

Figure 11. (a) Digital outcrop model showing several amalgamated and stacked intrusive bodies. (b) Interpretation of the different intrusive bodies and layers based on the model and outcrop observations, with brown colours representing igneous bodies, and the grey background representing sedimentary host rock.

host rock between them. Here, we find more, but shorter fractures mostly confined to one of the thin intrusion layers.

The fracture orientation and P21 fracture intensity distribution (Figure 12c, d) vary considerably along the mapped outcrop section (Figure 12 a,b, inset in Figure 2). The outer domains (0-90 m and 160-230 m, respectively) comprise P21 values of 0-2.5 m^{-1}, averaging 1.2 m^{-1}. Here, fractures are predominantly subvertical or subhorizontal. Contrastingly, we find nearly random fracture orientations and higher intensity values in the central domain between 90-160 m, which includes the fault as well as the bitumen dyke, injection structure and intrusion step. Here, average P21 is 2.0 m^{-1}, with minimum values of around 1m^{-1} and local maximum values of up to 3 and 6 m^{-1} around the fault and injection structures, respectively.

Finally, Figure 12e illustrates the connectivity variations along the outcrop section in terms of average connections per line (C_L). We include theoretical thresholds for onset of initial fracture connectivity (C_L = 2, red line) as well as percolation (C_L = 3.57, green dashed line) for reference. Again, we identify that connectivity in the two outer domains differs markedly from the central domain. In the outer domains, we obtain connectivity values of 1.47-2.47 and 2.12-2.44, respectively, i.e. partly below the threshold for a connected network. In the central domain, values vary between 3.25-4.02 average connections per line, i.e., the network is well connected and partly percolating

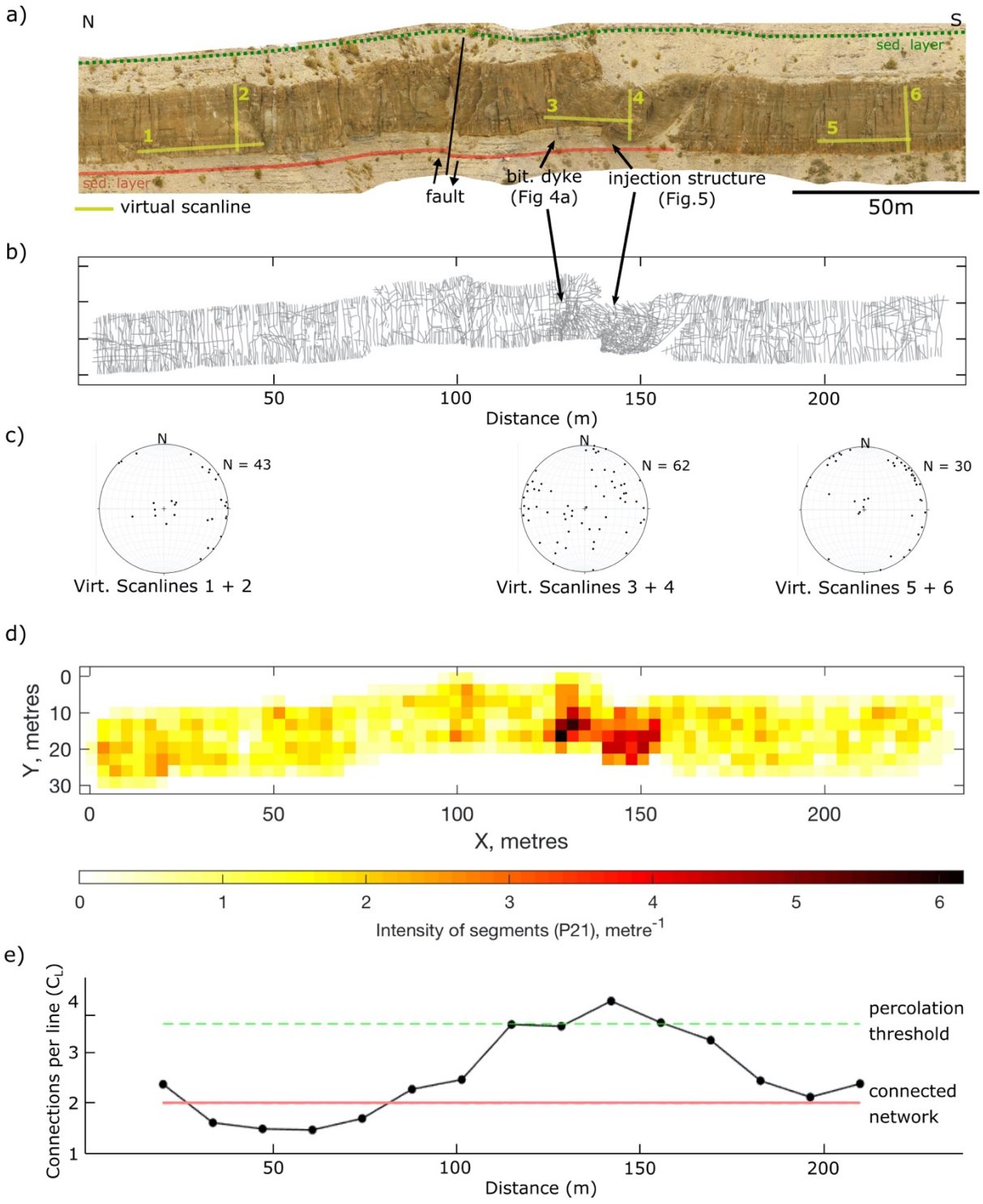

Figure 12. Fracture network quantification using a high-resolution digital outcrop model. (a) Orthophotograph indicating main geological features and scanline locations. (b) 2D fracture map of the outcrop. (c) Stereograms with poles of fracture planes measured along virtual scanlines on the 3D model. (d) Map of fracture intensity (P21). (e) Connectivity along outcrop based on fracture network topology.

4.2.3. Trace length statistics and MLE results

Statistical analysis results of the fracture trace length are presented in Figure 13. For a qualitative overview, we display the fracture trace map color-coded by length Figure 13a. It is already possible to see that the left and right domains (0-90 m, 160-230 m) are dominated by fewer, longer fractures compared to the central domain comprising fault and injection structures in addition to cooling joints (90-160 m). Also, we generally observe more and shorter fractures close to the contacts compared to the center. The overall trace length histogram indicates that small fractures dominate the mapped population with a peak at approximately at 0.4 m, and more than 80% smaller than 3 m. Interestingly, there is a small second peak at around 17 m, leading to a strongly asymmetric bimodal distribution.

We aim to quantify the lateral variability of the length distribution and assess the best mathematical description. Therefore, we present results of MLE fitting for power-law (Figure 13c-e) and log-normal distributions (Figure 13f-h) organized in three columns corresponding to the left, center and right parts of the outcrop, respectively, with a lower cutoff applied to account for truncation effects (red dotted line, supplement S3 for details). Table 1 summarizes the estimated likelihood for both distributions as well as exponential distribution, both with and without a cutoff. As a reminder, the MLE method estimates the likelihood that a population of values is drawn from a specific distribution.

For a power-law as well as exponential distribution, irrespective of an applied correction for truncation effects, the result is zero or near-zero percent likelihood (Table 1). For the power-law analysis shown in Figure 13c-e, this is reflected in a visibly poor fit in all three domains of the outcrop. We also observe a clear “kink” resulting from a change in slope for fractures large than around 15 m, especially in the outer domains where cooling joints dominate (Figure 13 c, e). Note in general that only the central domain data still stretch significantly more than one magnitude if a possible truncation bias is accounted for.

The MLE results for log-normal distributions yield ≥ 99 percent likelihood for the left, central and right domains of the outcrop, respectively, if no cut-off is applied to the observations (Table 1). Although generally applying a cutoff decreases the MLE likelihood, the domains are affected differently. While outer domains still reach values of 75 and 95 percent, respectively, the central domain drops to less than 5 percent likelihood, essentially ruling out a log-normal distribution. The generally better fit of log-normal distributions to our trace length data is visible in Figure 13 f-h. Note again that in the left and right outcrop domains, the largest fractures (ca. 15-20) m produce a local deviation from the trend, leading to underestimation by log-normal distributions (Figure 13f, h). Exponential distributions score near-zero percentages in all MLE analysis.

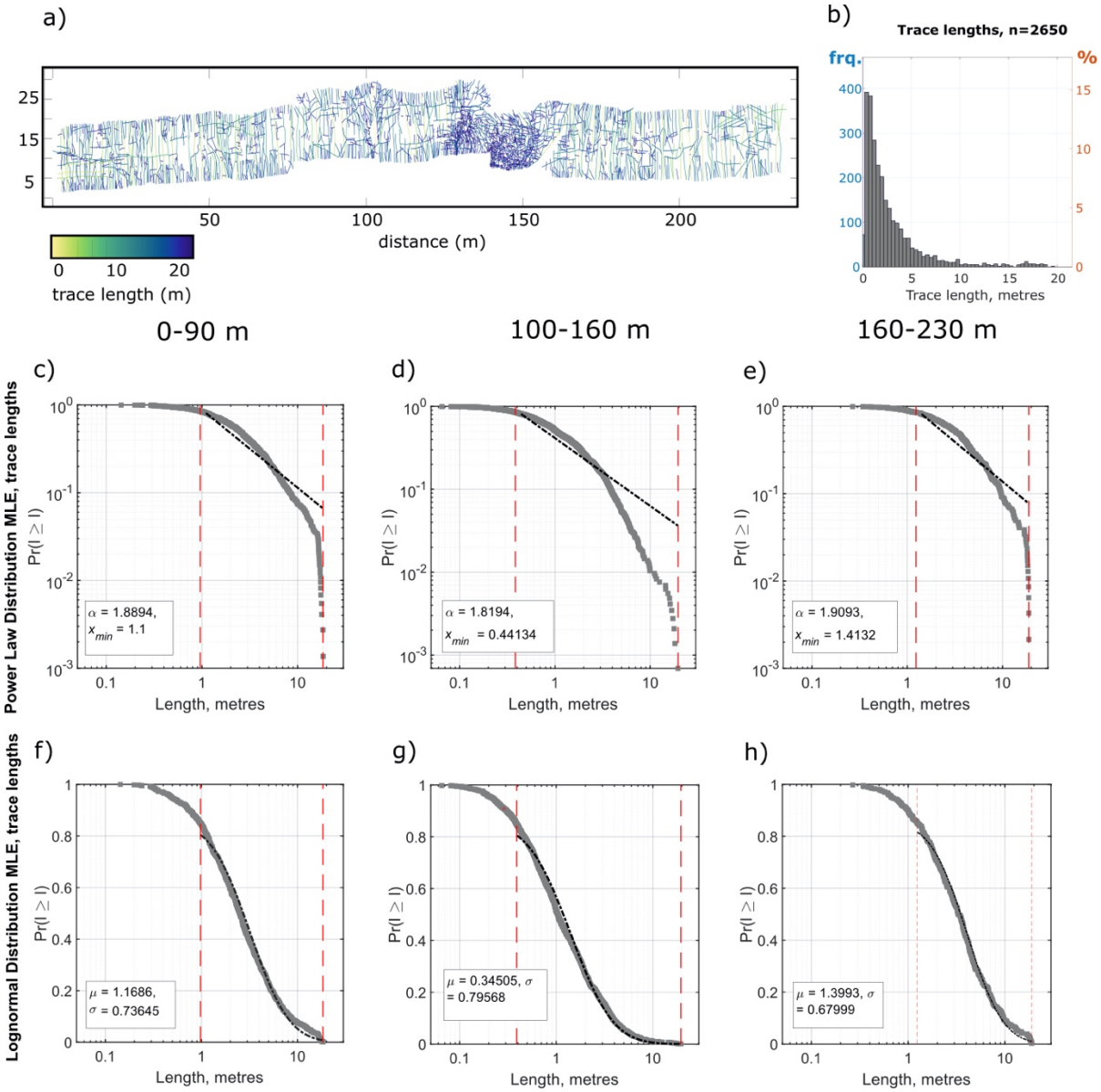

Figure 13. Fracture trace length statistics. (a) Fracture map colored by trace length. (b) Overall trace length histogram. (c-e) probability density functions plotted in double-logarithmic, along with MLE best fit for a power-law distribution (black stippled line). (f-h) probability density functions plotted in semi-logarithmic, along with MLE best fit lines for log-normal distribution. Red stippled lines indicate data range if cut-off is applied to account for potential truncation bias.

Table 1. MLE percentage likelihoods sorted by outcrop spatial domain and tested distribution type.

	Left domain	Center domain	Right domain
Power law	0 / 0	0 / 0	0 / 0
Log-normal	99.6 / 74.6	99.7 / 4.56	99.0/94.5
Exponential	0.5 / 0	0.56 / 0	1.5 / 0

5. Interpretation

5.1. Fracture network evolution

Our field observations show that, in the same geological setting, a wide range of fracture types can occur in the fracture network of igneous intrusions. We find bitumen and/or dead oil in all four identified fracture types within the sills at El Manzano (Figure 3a, b; Figure 4; Figure 5b, c; Figure 8e, f; Figure 9b-d), demonstrating that all fracture types may be accessible as pathways or even storage for hydrocarbons, but also fluids in general. Although most fracture types are directly related to the intrusion event, the underlying physical mechanisms of their formation are fundamentally different, resulting in a complex evolution of a laterally heterogenous fracture network.

Except for tectonic fractures, the fracture system in the sills is established within the period of cooling of the intrusion. While cooling joints form due to thermal stresses as the intrusion solidifies and contracts, the case of injection structures and large calcite veins are less obvious. However, the generally high thermal grade of the bitumen dykes in a geological setting with low burial-related temperatures and nearly no maturation (Figure 7), as well as entrainment of host rock pieces in intermingling bitumen and calcite veins (Figures 4e and 8d) strongly suggests that these features formed in the high-temperature environment with substantial fluid-overpressure surrounding the intrusions.

The driving processes for early fracture formation in the intrusions are thus not tectonic but related to thermally controlled processes around and within the intrusion, such as cooling-related contraction, hydrothermalism and metamorphic reactions including organic matter maturation in the surrounding host rock. However, these processes occur within tectonic far-field stresses, which is reflected in the alignment with the tectonic structures and inferred E-W maximum compressive stress for all fracture types (Figure 10). We will provide a more detailed interpretation of the individual fracture types in separate paragraphs.

Tectonically driven fracturing represents the only fracture mechanisms independent of the intrusion-related thermally controlled processes. Although overprinting due to faults is limited in the case of El Manzano, both qualitative and quantitative results show that faults may locally alter the initial fracture network and affect multiple intrusions (Figure 9, Figure 12). The exact timing of faulting after emplacement remains unclear in this case. It is only constrained by the time of sill solidification and the end of tectonic activity in the Sierra Azul range, which are both Miocene. However, due to the short time required for the relative thin

intrusions to cool (tens to hundreds of years), we generally regard faulting as a post-emplacement process.

5.2. Controlling factors of thermally driven fracture types

5.2.1. Cooling joints

Cooling joints are ubiquitous features throughout the field area and comprise bitumen filling in many locations (Figure 3). Their distribution and characteristics within the intrusions of the sill complex are quite variable and depend on several factors, including intrusion thickness, architecture and geometry. Figure 11 illustrates the relationship between these factors and the cooling joint distribution. Thick, massive intrusions emplaced as a single body tend to develop fewer, but longer cooling joints compared to the many small fractures seen intrusions that may be of similar overall thickness, but consist of multiple, partly disconnected branches. This is most likely the result of different cooling rates in the two scenarios, since higher cooling rates produce smaller joints (Hetényi et al., 2012). Even within intrusions the spatial distribution may vary, as we often observe more small cooling joints along the intrusion contact compared to the interior (Figure 12b). This could be related to a similar effect of faster cooling of the intrusion boundary in the initial phase after emplacement, when temperature gradients are still large. Since cooling joints propagate perpendicular to the intrusion surface, any curvature induces a change in local orientation distribution, e.g. at sill terminations or steps (Figure 11, Figure 12). All of the above leads us to the interpretation that the emplacement mechanism and its controlling factors play a major role in the final cooling joint distribution, as it controls the shape and architecture of intrusions and thus defines the boundary conditions for joint formation. In addition, far-field stresses may lead to preferential alignment of the cooling joints with the prevailing stress field (e.g., Maher 2020), as the confining stresses are likely anisotropic (Figure 10).

Due to the impregnation of joint surfaces with organic matter interpreted as high-grade bitumen (Figure 3a, b), we suggest that cooling joints may act as fluid pathways for hydrocarbons when the intrusion is still in the cooling phase. Any fluids flowing through newly formed cooling joints would be heated to temperatures of several hundred degrees, likely leading to combustion of all volatile hydrocarbons, leaving solid leftovers in the form of bitumen.

5.2.2. Bituminous injection structures

The bitumen dykes and injection structures (Figures 4 and 5) are perhaps the most spectacular fracture type observed in this study. We interpret them to result from strong heating and subsequent fast hydrocarbon generation in the metamorphic aureole of the sill intrusions, causing hydrofracturing within the shale due to fluid overpressure, sometimes up to the point of disintegration of the sediments. We base this interpretation on a combination of several observations. The very low background maturity level (TR = 0-20%) of the Agrio formation shale only increases to high values towards the intrusion contacts, where essentially all

organic matter has been transformed to hydrocarbons (Figure 7). Consequently, mobilization of hydrocarbons in the amounts necessary to form up to meter-thick bitumen dykes (Figure 3) requires the heat input provided by the intruding magma. In the high-temperature environment of thermal aureoles, maturation takes place over very short periods (hours to years, e. g. Iyer et al. 2017, Panahi et al. 2019), which can be regarded as geologically instantaneous. This would not allow for flow-driven overpressure relaxation within the practically impermeable shale formations, leading to propagation of fractures.

Strong additional fracturing of the intrusions, thinning and branching fractures, as well as partially missing host rock next to injection structures near the contact evidence propagation of the hydrofractures from the aureole into the intrusions (Figures 4, 5, and 12a, b). Mutual cross-cutting of bitumen dykes or calcite veins shows that new fractures were repeatedly generated with enough pressure to propagate through the previous generation in a "crack-seal" fashion (Figure 4c, e). Although previously formed cooling joints may have been exploited in some places, the propagation of bitumen dykes through the host rock and into the sill (Figures 4a, b and 5) must be related to hydraulic fracturing.

Both Raman spectrograms (Figure 6) and electrical conductivity of the bituminous material in the injection structures evidence strong thermal alteration and graphitization. This indicates formation of the injection structures shortly after solidification of the sill intrusions because this was the only period when temperatures required to form graphite were present at El Manzano (potentially >400°C for hydrothermal graphite, cf. Buseck and Beyssac, 2014).

Since the bitumen dykes commonly consist of several branches that may also crosscut each other, we suggest that the dykes formed in a series of pulses (Figure 4a-e). In addition, mutual cross-cutting of calcite veins and bitumen as well as calcite crystals entrained in bitumen dykes (Figure 4d-g, Figure 8a) point to (1) a repeated, violent fracturing process in accordance with the hydrofracturing model and (2) involvement of both hydrocarbon and other hydrothermal fluids. the calcite crystals in Figure 4g as entrained rather than grown in-situ because of their random orientations within the bitumen dyke (as opposed to e.g. fibrous growth) and the pieces of shale visible in the same dykes, which are clearly not in-situ. The two sets of orientations of bitumen dykes (N-S and E-W, see Figure 10) may indicate that the hydrofracturing occurred within the far-field stresses related to E-W Andean compression that created the Sierra Azul range. The relatively wide spread of orientations within the sets could be due to exploitation of, or interaction with, existing cooling joints, which show a wide scatter of orientations (Figure 10).

5.2.3. Hydrothermal calcite veins

Due to their frequent occurrence and size, the large calcite veins observed throughout the El Manzano outcrop represent another important type of fractures present in the igneous intrusions (Figure 8). The calcite veins observed within and at the tip of intrusions show (1) no indication of shearing and (2) mutual cross-cutting with the graphitic bitumen dykes (Figures 4d, e and 8a). They are therefore not fault-related, and likely formed contemporaneously with the bitumen dykes in a hydrothermal environment. Samples from

calcite veins show inclusions of CO2 within the calcite crystals, which could have been provided either by the intrusion itself, or by degradation of hydrocarbons (supplement S2). Overpressure-driven hydrofracturing during intrusion-related hydrothermalism may be a potential cause of vein formation, since pieces of host rock are commonly entrained in the calcite veins, pointing to a process violent enough to break up the host rock and transport the pieces over some distance (Figure 8d). Additionally, the observation of bedding-parallel fibrous calcite veins may indicate overpressure in the metamorphic aureole (Figure 9e). Since the calcite veins often crosscut intrusions (with single veins occasionally crosscutting several intrusions) and can reach many decimeters in thickness, we infer that they are the result of vertical movement of hydrothermal fluids at the scale of tens or even hundreds of meters.

5.3. Fracture types vs. fracture network properties

Quantitative fracture network characterization along a 230 m long outcrop section reveals strong parameter variations caused by local interaction of several fracture types and mechanisms (Figures 12 and 13). The mapped outcrop shown in Figure 12 has three domains which comprise different fracture types and features. While the outer domains (0-90 m, 160-230 m, Figure 12a) are dominated by cooling joints, the central domain (90-160 m) includes a fault and two injection structures, as well as a primary step in the intrusion geometry. The step is identified by offset in the sill, but an absence of offset in the sedimentary layer above. While the properties are similar in the outer domains with cooling joints only, the addition of other fracture types in the central domain leads to an increase in density, a wider spread in orientations, and much higher connectivity (Figure 12b-e). We suggest that the interaction of fracture types other than cooling joints does not only simply add more fractures, but leads to a wider orientation distribution, since faults and injection structures do not necessarily follow paths perpendicular to the intrusion contact like cooling joints. As increasing connectivity requires not just more fractures, but also fracture intersections, the addition of oblique fractures by injection structures and faults is vital for an actual connectivity increase. Importantly, the step in the intrusion geometry introduces inclined cooling joints, which further diversifies the fracture orientations.

Additionally, the lateral variability in the presence of different fracture types also manifests itself in the fracture length statistics (Figure 13). The qualitative impression from the colored fracture map is that smaller fractures are concentrated in the central domain (Figure 13a). Thus, instead of focusing on the overall length distribution for the entire outcrop (displayed as a histogram in Figure 13b), we analyze the length distribution per domain. Here, it becomes clear that the outer domains with mainly cooling joints show very similar characteristics. The distributions comprise fractures between ca. 0.2 and 20 m, with few small and large joints, that fit well with log-normal distributions according to MLE analysis (Figure 13c, e, Table 1), but not power laws or exponential distributions (Figure 13f, h, Table 1). We interpret this result in the light of the existence of a characteristic length scale for cooling joints that depends on cooling rates and the size of the intrusion, especially since other fracture types that may alter the distribution are absent. From this perspective the poor fit with a power law is unsurprising since power-laws imply scale-independent distributions. It is noteworthy that the largest joints spanning the entire intrusion thickness (15-20 m) create a “kink” in the

distributions that leads to underrepresentation in the log-normal distribution. This indicates that a log-normal distribution also does not fully capture the geological process.

On the other hand, the results from the central domain are more difficult to capture in terms of mathematical descriptions. Despite a striking increase in smaller fractures due to faulting and injection structures, MLE analysis yields a poor fit with a power-law even for bias-corrected data, which is also obvious from a qualitative comparison of the best fit and the data (Figure 13g, Table 1). However, MLE only favors a log-normal distribution if no lower cutoff is applied, and in fact discards a log-normal distribution otherwise (Figure 13d, Table 1). Based on outcrop observations, we believe that truncation bias of some extent exists in this area, suggesting that not all fractures are represented even in the high-resolution models and a correction should be applied. Consequently, we interpret the lack of any reasonable fit with standard mathematical models common in fracture length description to be a result of interacting fracture processes with very different underlying physics. The blend of cooling joints, a fault-related damage zone and two injection structures creates a highly heterogenous local fracture population which markedly increases fracture density and connectivity but does not seem to follow any unified fracture length distribution.

6. **Discussion**

6.1. Fracture network evolution

Establishing the fracture evolution within the igneous intrusions at El Manzano is an important step towards understanding fracturing of igneous intrusions in organic-rich shales in general. In addition, it provides further insight into the igneous petroleum system evolution of producing igneous sill reservoirs, such as those in the Neuquén Basin. Our multi-disciplinary methodology allows us to constrain timing and temperature conditions during fracture formation and demonstrate the quantitative manifestation of the wide spectrum of fracture processes in the form of laterally varying fracture parameters over hundreds of meters. In the following paragraphs, we will utilize our results to critically evaluate the existing conceptual model of thermal impact and fracture evolution in the igneous petroleum systems in the Rio Grande Valley (Spacapan et al., 2020; Witte et al., 2012). Based on this evaluation, we present a more process-oriented model focused on fracturing mechanisms that honors both previous knowledge and the plentiful field evidence provided in this article (Figure 14).

6.1.1. Thermal phase: Hydro-thermo-mechanical interaction

The existing models emphasize the importance of intrusion-related processes. Spacapan et al. (2020) distinguish two phases: The initial “thermal stage” is dominated by temperature-driven metamorphic reactions in the aureole and fluid migration away from the intrusion due to local pressure gradients. During the subsequent “cooling stage” a cooling joint network is established and hydrothermally driven hydraulic fracturing occurs in the host rock, leading to a first pulse of fluid and hydrocarbon migration into the intrusions due to a reversed fluid

pressure gradient (Witte et al., 2012). This model implies a clear temporal sequence of fluid generation in high temperature environment, followed by fracturing and migration in a cooler environment.

However, from our observations, a key characteristic of the early phase after magma emplacement is that processes appear to take place simultaneously, and chemical reactions, fracturing and migration have an immediate causal relationship. The occurrence of injection structures showing strong thermal alteration (graphitization) and evidence of forceful injection (Figure 4 - Figure 7), as well as bitumen impregnating cooling joints (Figure 3) and hydrothermal veins carrying host rock pieces and intermingling with bitumen dykes (Figure 8) demonstrate that hydrocarbon-bearing fluids entered the intrusion at temperatures of several hundred degrees. The intense modification of the fracture network (Figures 12 and 13) we observe within intrusions through interaction of bituminous injection structures and cooling joints shortly after emplacement represents a novel result that is not included in previous models.

Our interpretation of emplacement of injection structures in distinct pulses fits well with results from field studies, laboratory models and numerical studies of maturation-related fracture networks, where repeated pressure build-up and release is observed (Kobchenko et al., 2014; Panahi et al., 2019; Rabbel et al., 2020). Previous field studies reported on extensive bitumen dykes in the northern Neuquén basin and suggested a connection to volcanic activity based on general proximity of the dykes to volcanic bodies and radial bitumen dyke orientations around volcanic centers (Rassmuss, 1923; Cobbold et al., 2014; Zanella et al., 2015). Our study demonstrates this connection and, at least in the study area, clearly establishes that the bitumen dykes formed before the intrusion has fully cooled down. Note, however, that both the thermal maturity and proximity to volcanic structures of bitumen dykes across the basin varies greatly. Different modes of formation have been suggested and their evolutional model requires a case-by-case evaluation (Parnell and Carey 1995).

Our interpretation agrees with observations from other studies of sediment-intrusion interactions focusing on pressure evolution in these systems. From the moment of emplacement, the intrusion cools down and shrinks, progressively generating primary porosity in the form of cooling joints and vesicles as well as strong fluid underpressure even before complete solidification (Aarnes et al., 2008). At the same time, temperatures in the organic-rich shales rise. The resulting fast hydrocarbon generation, mineral dehydration and thermal fluid expansion causes a drastic rise in pore fluid pressure in the impermeable shale, leading to hydraulic fracturing (Aarnes et al., 2012). The occurrence of bedding-parallel fibrous veins (Figure 9e) in the contact aureole as well as bitumen dykes at El Manzano (Figure 4, Figure 5) matches well with previous work from the Neuquén Basin that related these features to strong heating and hydraulic fracturing in shales, possibly due to volcanic activity (Zanella et al., 2015). Thus, a situation arises in which different fracturing processes within sediments and intrusions are ongoing, and fluid flow of newly created fluids or fluidized sediments into the intrusion (c.f. Figure 14 a-e) is facilitated by an inward-directed fluid pressure gradient (Svensen et al., 2010). Importantly, the intrusion temperature at this time is still at several hundred degrees, causing thermal alteration of the incoming material.

Overall, the dynamic period directly after emplacement appears to be defining for the formation of the initial fracture distribution in intrusions emplaced in organic-rich shales. Despite the comfort afforded by a model displaying the clear distinction of phases by timing and processes, we argue that a more accurate description of the "thermal phase" of an evolutionary model should comprise simultaneous, interacting processes leading to an initially heterogeneous fracture network, as depicted in Figure 14. Tectonic overprinting after the intrusion has cooled down may further alter this fracture network, potentially also establishing connections to previously isolated primary pores (Figure 9c and 14).

6.2. Implications for the petroleum system

6.2.1. Fracture network properties of igneous reservoirs

Our field observations indicating direct evidence for bitumen and/or dead oil occurring in each fracture type demonstrate that all types of fractures found in the igneous intrusions can be involved in hosting hydrocarbons (Figure 14). This complements previous conceptual studies based on well data and modeling, which focus on the contribution of cooling joints to the fracture porosity of igneous reservoirs (e.g., Delpino and Bermúdez, 2009; Gudmundsson and Løtveit, 2014). We present an easily accessible, world-class locality where geologists can observe the role of different fracture types in the petroleum system firsthand.

High lateral variability of fracture intensity and connectivity (Figure 12) implies strong changes in fluid storage capacity as well as fracture permeability over short distances. In this context, interaction of multiple fracture types appears to enhance reservoir quality locally. Additionally, our results highlight laterally varying fracture length statistics and render power-law behavior for fracture length in igneous intrusions unlikely (Figure 13, Table 1). Among the available choices evaluated using the MLE method, a log-normal distribution with laterally varying parameters provides the best results, although in intensely fractured areas affected by multiple fracturing mechanisms this model fails to accurately reflect the entire fracture network. This may be explained by an overprinting of fracture populations associated with the different fracturing processes, some of which (e.g., tectonic fracturing) may create a power law distribution, while others (e.g. cooling joints) have characteristic length scales related to intrusion geometry and boundary conditions of the cooling process (Goehring and Morris, 2008; Hetényi et al., 2012). Overall, the striking lateral variability of the fracture network over 10s to 100s of meters contrasts with previous findings by Witte et al. (2012), who stated that fracture networks and therefore permeability should be relatively constant over such distances. We therefore advise that any attempt to model the fracture networks of intrusions in a petroleum system should include careful evaluation of evidence for lateral heterogeneity of the fracture network.

Production data from oil fields close to El Manzano (Figure 1) were published by Spacapan et al. (2020), showing high initial production rates followed by a sharp drop, sometimes only after a couple of months. They related this to initial drainage of the hydrocarbons in the fracture network, followed by a much smaller mixed matrix-fracture production. As the El Manzano sill complex represents a direct outcrop analogue for the adjacent subsurface

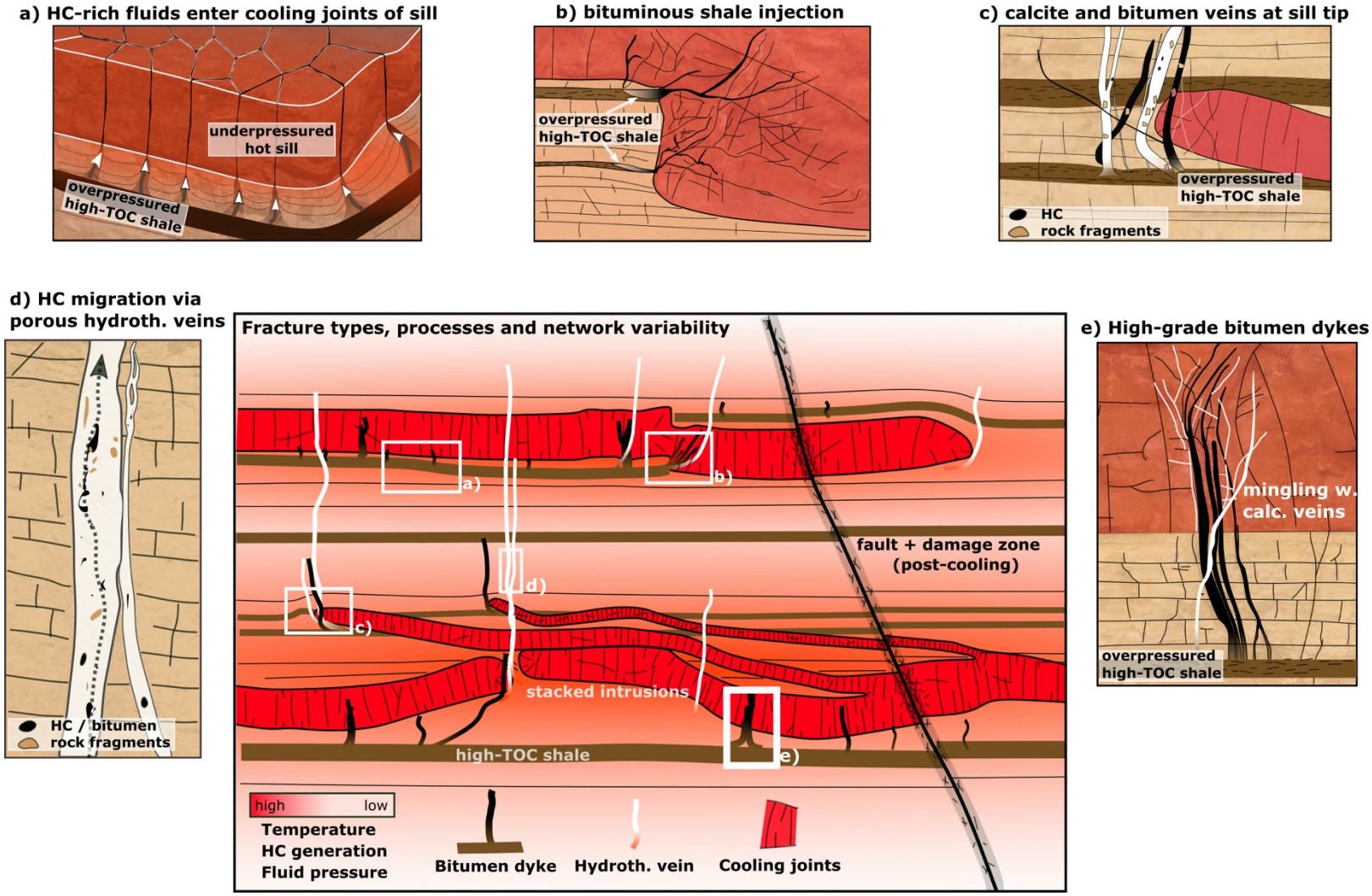

Figure 14. Schematic summary of fracture types, underlying mechanisms and fracture network variations interpreted from field evidence presented in this paper. Central image visualizes the large-scale features, including intrusion architecture and its relation to spatial fracture network variations. Insets (a-f) highlight specific fracture types and potential implications for igneous reservoirs.

systems of the Rio Grande Valley comprising comparable extent and intrusion sizes, the outcrops may serve to develop a better understanding of the subsurface fracture systems holding the producible hydrocarbons.

Perhaps, the local areas of extreme fracture density seen at El Manzano (Figure 12) represent the pockets of high fracture density that are drained in the initial phase of production. However, previous research pointed out the existence of so-called cavity zones that may not always be related to fracturing but could also be due to large vesicles form by late-stage volatiles (Bermúdez and Delpino, 2008; Witte et al., 2012). A promising next step would be to utilize the quantitative outcrop observations to conduct fluid flow and production simulations for comparison.

6.2.2. Hydrocarbon generation and migration

The thermal effect of intrusions in terms of a metamorphic aureole with rapid hydrocarbon maturation is well established through case studies around the world (Aarnes et al., 2010; Muirhead et al., 2017; Rodriguez Monreal et al., 2009; Spacapan et al., 2018). In the case of El Manzano, this effect is an overall positive one, since previously immature source rocks show elevated transformation ratios around the intrusions (Figure 7). However, the discovery of graphitic bitumen dykes and bitumen within intrusions and their aureoles is an important discovery because it provides evidence for mobilization and migration of hydrocarbon-bearing fluids into the intrusions while the temperatures are sufficient for substantial thermal alteration. Although our thermal methods are qualitative and cannot assess the exact temperature, the observed graphitization indicates that the hydrocarbon-rich fluids experienced “in-situ combustion” at several hundred degrees.

Considering the impressive size of some the observed bitumen dykes, a significant part of the petroleum potential around the intrusions may be lost in the first pulse of local fluid generation and migration, which has previously been proposed as a charge mechanism for oil into the intrusions (Spacapan et al., 2020; Witte et al., 2012). It is important to note that the bitumen dykes observed in the outcrops are always proximal to intrusions and do not extend far from the contacts, making them very localized migration features. Assuming a penny-shape for the bitumen dyke shown in Figure 4a as lower boundary, this feature alone comprises around 160 m^3 (ca. 1000 barrels) of solid bitumen. Further investigation should explore this migration pulse in more detail to quantify the hydrocarbon volume that may survive. It seems reasonable to assume that for liquid hydrocarbons to survive and be produced, migration into the fractured intrusions must take place after the intrusion has fully or nearly cooled down to ambient temperatures.

Furthermore, our observations agree with the suggestion of Spacapan et al. (2020) that both the faults and hydrothermal calcite veins may connect different levels of sill intrusions and facilitate vertical migration of hydrocarbons from lower stratigraphic levels, in this case the Vaca Muerta Fm (Figure 14). At El Manzano, both features commonly intersect and thus connect several intrusions, and show evidence of hydrocarbons occupying their porosity (Figure 8e, f, 9c and d). These features may therefore control local fluid flow patterns and should be included in reservoir-scale flow modeling.

6.2.3. Implications for geophysical properties

Finally, our results may reveal some of the geological mechanisms responsible for the large variations in geophysical properties observed in well data from the intrusive reservoirs near the study area (Rabbel et al., 2018; Spacapan et al., 2019, Witte et al., 2012). In addition to mineral composition (both primary and secondary), porosity and fracturing strongly control seismic velocity changes in igneous rocks (e.g., Berge et al., 1992; Mark et al., 2018). Although we do not provide measurements or modeling of potential fracture-related velocity changes in the intrusions investigated in this study, the drastic increase in fracture density as well as the associated alteration should be capable of reducing seismic velocities of intrusions significantly. In fact, the El Manzano field locality previously served as a site for outcrop-based seismic modeling of a sill complex investigating the effects of velocity variations on seismic imaging of intrusions and found marked dimming of reflections if velocities are at the lower end of the spectrum (Rabbel et al., 2018). In addition, increased fracturing due to metamorphic reactions in the aureole as well as the occurrence of graphite may contribute to the low-resistivity zones around sills documented by Spacapan et al. (2019). Thus, the presented field study may give applied geophysicists a more practical understanding of the geological features they are dealing with and illustrate potential causes of the wide spectrum of seismic responses that are possible in igneous intrusions.

7. Conclusions

We present an interdisciplinary field study of the fracture network in an igneous sill complex emplaced in organic-rich shale in the northern Neuquén Basin, Argentina. Our observations including drone and ground based photogrammetry and geochemical data demonstrate that a wide spectrum of fracturing mechanisms can affect the fracture network of intrusions. We employ digital fracture mapping on high-resolution digital outcrop models to quantify the effect of these processes on fracture network properties. Based on the results, we draw the following conclusions:

- We identify four different fracture types present in sills, driven by a broad spectrum of physical processes. These include (1) cooling joints created by thermal contraction, (2) faults and associated tectonic fractures, (3) bitumen dykes and bituminous shale injection structures, and (4) hydrothermal veins, likely due to hydrofracturing initiated in the metamorphic aureole.

- Except for tectonic fractures, the fracture network is established during the early phase dominated by a high-temperature environment. Evidence suggests that in this phase, hydrocarbons generated may be mobilized and migrate into the intrusion and experience temperatures of several hundred degrees, where in-situ combustion of volatiles and graphitization of solid bitumen takes place.

- We observe the different fracture types throughout the outcrop, but they do not occur spatially homogenous. Instead, the fracture network properties exhibit strong lateral changes on the scale of some tens to hundreds of meters, depending on the number and intensity of processes involved. Such changes involve locally increased fracture density, wider orientation distribution, higher connectivity, and a variable length distribution.

- Comparison of different mathematical distributions shows that fracture lengths are best represented through a spatially varying log-normal distribution, although even this is not overall satisfactory. Our analysis also demonstrates that previously suggested power-law behavior is very unlikely and difficult to justify considering the various physical processes at work.
- Strong variations in fracture network properties imply similar heterogeneities for petrophysical and geophysical properties, such as locally enhanced storage capacity and fracture permeability or reduced seismic velocities.

Overall, this study extends our understanding of fracture networks in igneous intrusions acting as petroleum reservoirs and provides numerous field examples and quantitative data. The El Manzano field analogue can thus be used help geoscientists of all disciplines to better constrain modeling efforts and develop a more practical understanding of subsurface igneous petroleum systems.

Acknowledgements

We thank our colleagues Hector Leanza, Adrian Medialdea, Diego Cattaneo and Federico Soto for their hospitality, invaluable help in the field and insightful discussions. The authors are thankful for the constructive reviews from Alain Zanella, an anonymous reviewer, and editor Virginia Toy.

Funding

For this work we received funding by through several grants of the University of Oslo (Universitetet i Oslo) and the Research Council of Norway: Earthflows initiative (grant no. 267775), DIPS project (grant no. 240467), and DEEP Research School (249040/F60). YPF and YPF Technologia (Y-TEC) provided additional funding.

References

Aarnes, I., Podladchikov, Y., Svensen, H., 2012. Devolatilization-induced pressure build-up: Implications for reaction front movement and breccia pipe formation. Geofluids 12, 265-279.

Aarnes, I., Podladchikov, Y.Y., Neumann, E.-R., 2008. Post-emplacement melt flow induced by thermal stresses: Implications for differentiation in sills. Earth and Planetary Science Letters 276, 152-166.

Aarnes, I., Svensen, H., Connolly, J.A.D., Podladchikov, Y.Y., 2010. How contact metamorphism can trigger global climate changes: Modeling gas generation around igneous sills in sedimentary basins. Geochimica et Cosmochimica Acta 74, 7179-7195.

Aarnes, I., Svensen, H., Polteau, S., Planke, S., 2011. Contact metamorphic devolatilization of shales in the Karoo Basin, South Africa, and the effects of multiple sill intrusions. Chemical Geology 281, 181-194.

Berge, P.A., Fryer, G.J., Wilkens, R.H., 1992. Velocity-porosity relationships in the upper oceanic crust: Theoretical considerations. Journal of Geophysical Research: Solid Earth 97, 15239-15254.

Bermúdez, A., Delpino, D.H., 2008. Concentric and radial joint systems within basic sills and their associated porosity enhancement, Neuquén Basin, Argentina. Geological Society, London, Special Publications 302, 185-198.

Bettini, F., Vasquez, J., 1979. Geologia de la Sierra Azul, Rio Grande y Sector Occidental de La Siera de Palauco. Yacimientos Petrolíferos Fiscales (internal report) Buenos Aires.

Bonnet, E., Bour, O., Odling, N.E., Davy, P., Main, I., Cowie, P., Berkowitz, B., 2001. Scaling of fracture systems in geological media. Reviews of Geophysics 39, 347-383.

Borello, A.V. 1944. Sobre el estado actual de los Yacimientos de Asfaltita del Sud de Menzoda. Yacimientos Carboniferos Fiscales, pp. 1-20. unpublished report.

Buckley, S.J., Ringdal, K., Naumann, N., Dolva, B., Kurz, T.H., Howell, J.A., Dewez, T.J., 2019. LIME: Software for 3-D visualization, interpretation, and communication of virtual geoscience models. Geosphere 15, 222-235.

Buseck, P.R., Beyssac, O., 2014. From organic matter to graphite: Graphitization. Elements 10, 421-426.

Cobbold, P.R., Ruffet, G., Leith, L., Loseth, H., Rodrigues, N., Leanza, H.A., Zanella, A., 2014. Radial patterns of bitumen dykes around Quaternary volcanoes, provinces of northern Neuquén and southernmost Mendoza, Argentina. Journal of South American Earth Sciences 56, 454-467.

Combina, A.M., Nullo, F., 2011. Ciclos tectónicos, volcánicos y sedimentarios del Cenozoico del sur de Mendoza-Argentina (35°-37° S y 69° 30'W). Andean Geol. 38, 198–218.

Delpino, D., Bermúdez, A., 2009. Petroleum systems including unconventional reservoirs in intrusive igneous rocks (sills and laccoliths). The Leading Edge 28, 804-811.

Einsele, G., Gieskes, J.M., Curray, J., Moore, D.M., Aguayo, E., Aubry, M.-P., Fornari, D., Guerrero, J., Kastner, M., Kelts, K., Lyle, M., Matoba, Y., Molina-Cruz, A., Niemitz, J., Rueda, J., Saunders, A., Schrader, H., Simoneit, B., Vacquier, V., 1980. Intrusion of basaltic sills into highly porous sediments, and resulting hydrothermal activity. Nature 283, 441-445.

Espitalié, J., Deroo, G., Marquis, F., 1985. La pyrolyse Rock-Eval et ses applications. Revue de l'Institut français du pétrole 40, 563-579.

Galland, O., Spacapan, J.B., Rabbel, O., Mair, K., Soto, F.G., Eiken, T., Schiuma, M. and Leanza, H.A., 2019. Structure, emplacement mechanism and magma-flow significance of igneous fingers–Implications for sill emplacement in sedimentary basins. Journal of Structural Geology, 124: 120-135.

Goehring, L., Morris, S.W., 2008. Scaling of columnar joints in basalt. Journal of Geophysical Research: Solid Earth 113.

Gudmundsson, A., Løtveit, I.F., 2014. Sills as fractured hydrocarbon reservoirs: examples and models. Geological Society, London, Special Publications 374, 251-271.

Guerriero, V., Iannace, A., Mazzoli, S., Parente, M., Vitale, S., & Giorgioni, M. (2010). Quantifying uncertainties in multi-scale studies of fractured reservoir analogues: Implemented statistical analysis of scan line data from carbonate rocks. Journal of Structural Geology, 32(9), 1271-1278.

Healy, D., Rizzo, R.E., Cornwell, D.G., Farrell, N.J., Watkins, H., Timms, N.E., Gomez-Rivas, E., Smith, M., 2017. FracPaQ: A MATLAB™ toolbox for the quantification of fracture patterns. Journal of Structural Geology 95, 1-16.

Heap, M.J., Kennedy, B.M., 2016. Exploring the scale-dependent permeability of fractured andesite. Earth and Planetary Science Letters 447, 139-150.

HeténYi, G., Taisne, B., Garel, F., Médard, É., Bosshard, S., Mattsson, H.B., 2012. Scales of columnar jointing in igneous rocks: field measurements and controlling factors. Bulletin of Volcanology 74, 457-482.

Howell, J.A., Schwarz, E., Spalletti, L.A., Veiga, G.D., 2005. The Neuquén Basin: an overview, in: Veiga, G.D., Spalletti, L.A., Howell, J.A., Schwarz, E. (Eds.), Geological Society, London, Special Publications, pp. 1-14.

Iyer, K., Schmid, D.W., Planke, S., Millett, J., 2017. Modelling hydrothermal venting in volcanic sedimentary basins: Impact on hydrocarbon maturation and paleoclimate. Earth and Planetary Science Letters 467, 30-42.

Kay, S.M., Burns, W.M., Copeland, P., Mancilla, O., 2006. Upper Cretaceous to Holocene magmatism and evidence for transient Miocene shallowing of the Andean subduction zone under the northern Neuquén Basin. Geological Society of America Special Papers 407, 19-60.

Kobchenko, M., Hafver, A., Jettestuen, E., Renard, F., Galland, O., Jamtveit, B., Meakin, P., Dysthe, D.K., 2014. Evolution of a fracture network in an elastic medium with internal fluid generation and expulsion. Physical Review E 90, 052801.

Lafargue, E., F. Marquis, and D. Pillot. "Rock-Eval 6 applications in hydrocarbon exploration, production, and soil contamination studies." Revue de l'institut français du pétrole 53.4 (1998): 421-437.

Manceda, R., Figueroa, D., 1995. Inversion of the Mesozoic Neuquén rift in the Malargüe fold and thrust belt, Mendoza, Argentina, in: Tankard, A.J., S., S., Welsink, H.J. (Eds.), Petroleum basins of South America: AAPG Memoir, pp. 369–382.

Mao, A., Zheng, H., Sun, X., 2020. Microstructure Investigation of Oil-Bearing Rhyolites: A Case Study from the Hailar Basin, NE China. Minerals 10, 699.

Mark, N., Schofield, N., Pugliese, S., Watson, D., Holford, S., Muirhead, D., Brown, R., Healy, D., 2018. Igneous intrusions in the Faroe Shetland basin and their implications for hydrocarbon exploration; new insights from well and seismic data. Marine and Petroleum Geology 92, 733-753.

Muirhead, D.K., Bowden, S.A., Parnell, J., Schofield, N., 2017. Source rock maturation owing to igneous intrusion in rifted margin petroleum systems. Journal of the Geological Society.

Muirhead, D.K., Parnell, J., Taylor, C., Bowden, S.A., 2012. A kinetic model for the thermal evolution of sedimentary and meteoritic organic carbon using Raman spectroscopy. Journal of Analytical and Applied Pyrolysis 96, 153-161.

Panahi, H., Kobchenko, M., Meakin, P., Dysthe, D.K., Renard, F., 2019. Fluid expulsion and microfracturing during the pyrolysis of an organic rich shale. Fuel 235, 1-16.

Parnell, J., & Carey, P. F. (1995). Emplacement of bitumen (asphaltite) veins in the Neuquén Basin, Argentina. AAPG bulletin, 79(12), 1798-1816.

Potgieter-Vermaak, S., Maledi, N., Wagner, N., Van Heerden, J., Van Grieken, R., Potgieter, J., 2011. Raman spectroscopy for the analysis of coal: a review. Journal of Raman Spectroscopy 42, 123-129.

Rabbel, O., Galland, O., Mair, K., Lecomte, I., Senger, K., Spacapan, J.B., Manceda, R., 2018. From field analogues to realistic seismic modelling: a case study of an oil-producing andesitic sill complex in the Neuquén Basin, Argentina. Journal of the Geological Society 175, 580-593.

Rabbel, O., Mair, K., Galland, O., Grühser, C., Meier, T., 2020. Numerical modeling of fracture network evolution in organic-rich shale with rapid internal fluid generation. Journal of Geophysical Research: Solid Earth 125, e2020JB019445.

Rassmuss, J. (1923). Breves apuntes geológicos sobre la parte del territorio del Neuquén entre Auca Mahuida y El Tromen. Dirección General de Minas, Geología e Hidrogeología Serie F (informe Prel. y Comunicaciones), Boletín, 6, 15-20.

Rateau, R., Schofield, N., Smith, M., 2013. The potential role of igneous intrusions on hydrocarbon migration, West of Shetland. Petroleum Geoscience 19, 259-272.

Rizzo, R.E., Healy, D., De Siena, L., 2017. Benefits of maximum likelihood estimators for fracture attribute analysis: Implications for permeability and up-scaling. Journal of Structural Geology 95, 17-31.

Rodriguez Monreal, F., Villar, H.J., Baudino, R., Delpino, D., Zencich, S., 2009. Modeling an atypical petroleum system: A case study of hydrocarbon generation, migration and accumulation related to igneous intrusions in the Neuquen Basin, Argentina. Marine and Petroleum Geology 26, 590-605.

Sanderson, D.J., Nixon, C.W., 2018. Topology, connectivity and percolation in fracture networks. Journal of Structural Geology 115, 167-177.

Schutter, S.R., 2003. Hydrocarbon occurrence and exploration in and around igneous rocks, in: Petford, N., McCaffrey, K.J.W. (Eds.), Hydrocarbons in Crystalline Rocks. Geological Society, London, Special Publications, pp. 7-33.

Senger, K., Buckley, S.J., Chevallier, L., Fagereng, Å., Galland, O., Kurz, T.H., Ogata, K., Planke, S., Tveranger, J., 2015. Fracturing of doleritic intrusions and associated contact zones: Implications for fluid flow in volcanic basins. Journal of African Earth Sciences 102, 70-85.

Senger, K., Millett, J., Planke, S., Ogata, K., Eide, C., Festøy, M., Galland, O., Jerram, D., 2017. Effects of igneous intrusions on the petroleum system: a review. First Break 35, 10.

Spacapan, J., Palma, J., Galland, O., Manceda, R., Rocha, E., D'Odorico, A., Leanza, H., 2018. Thermal impact of igneous sill-complexes on organic-rich formations and implications for petroleum systems: A case study in the northern Neuquén Basin, Argentina. Marine and Petroleum Geology 91, 519-531.

Spacapan, J.B., D'Odorico, A., Palma, O., Galland, O., Rojas Vera, E., Ruiz, R., Leanza, H.A., Medialdea, A., Manceda, R., 2020. Igneous petroleum systems in the Malargüe fold and thrust belt, Río Grande Valley area, Neuquén Basin, Argentina. Marine and Petroleum Geology 111, 309-331.

Svensen, H., Aarnes, I., Podladchikov, Y.Y., Jettestuen, E., Harstad, C.H., Planke, S., 2010. Sandstone dikes in dolerite sills: Evidence for high-pressure gradients and sediment mobilization during solidification of magmatic sheet intrusions in sedimentary basins. Geosphere 6, 211-224.

Svensen, H., Planke, S., Malthe-Sørenssen, A., Jamtveit, B., Myklebust, R., Rasmussen Eidem, T., Rey, S.S., 2004. Release of methane from a volcanic basin as a mechanism for initial Eocene global warming. Nature 429, 542-545.

Westoby, M., Brasington, J., Glasser, N., Hambrey, M. & Reynolds, J. 2012: 'Structure-from-Motion'photogrammetry: A low-cost, effective tool for geoscience applications. Geomorphology 179, 300-314.

Witte, J., Bonora, M., Carbone, C., Oncken, O., 2012. Fracture evolution in oil-producing sills of the Rio Grande Valley, northern Neuquen Basin, Argentina. AAPG Bulletin 96, 1253-1277.

Yagupsky, D.L., Cristallini, E.O., Fantín, J., Valcarce, G.Z., Bottesi, G., Varadé, R., 2008. Oblique half-graben inversion of the Mesozoic Neuquén Rift in the Malargüe Fold and Thrust Belt, Mendoza, Argentina: New insights from analogue models. Journal of Structural Geology 30, 839-853.

Zanella, A., Cobbold, P.R., Ruffet, G., Leanza, H.A., 2015. Geological evidence for fluid overpressure, hydraulic fracturing and strong heating during maturation and migration of hydrocarbons in Mesozoic rocks of the northern Neuquén Basin, Mendoza Province, Argentina. Journal of South American Earth Sciences 62, 229-242.

Zeeb, C., Gomez-Rivas, E., Bons, P.D., Blum, P., 2013. Evaluation of sampling methods for fracture network characterization using outcrops. AAPG Bulletin 97, 1545-1566.

Zhou, Q., Xiao, X., Pan, L., Tian, H., 2014. The relationship between micro-Raman spectral parameters and reflectance of solid bitumen. International Journal of Coal Geology 121, 19-25.

Supplementary Material for:

Fracture networks in shale-hosted igneous sills: Processes, distribution and implications for igneous petroleum systems

Authors: Ole Rabbel[a,*], Octavio Palma[b], Karen Mair[a], Olivier Galland[a], Juan B. Spacapan[b], Kim Senger[c]

[1] Physics of Geological Processes, The NJORD Centre, Department of Geosciences, University of Oslo, Box 1047, Blindern, 0316, Oslo, Norway

[2] YTEC, Av. Del Petroleo s/n – 129 y 143, 1925 Berisso–Buenos Aires, Argentina

[3]Department of Arctic Geology, University Centre in Svalbard, Box 156, 9171 Longyearbyen, Norway

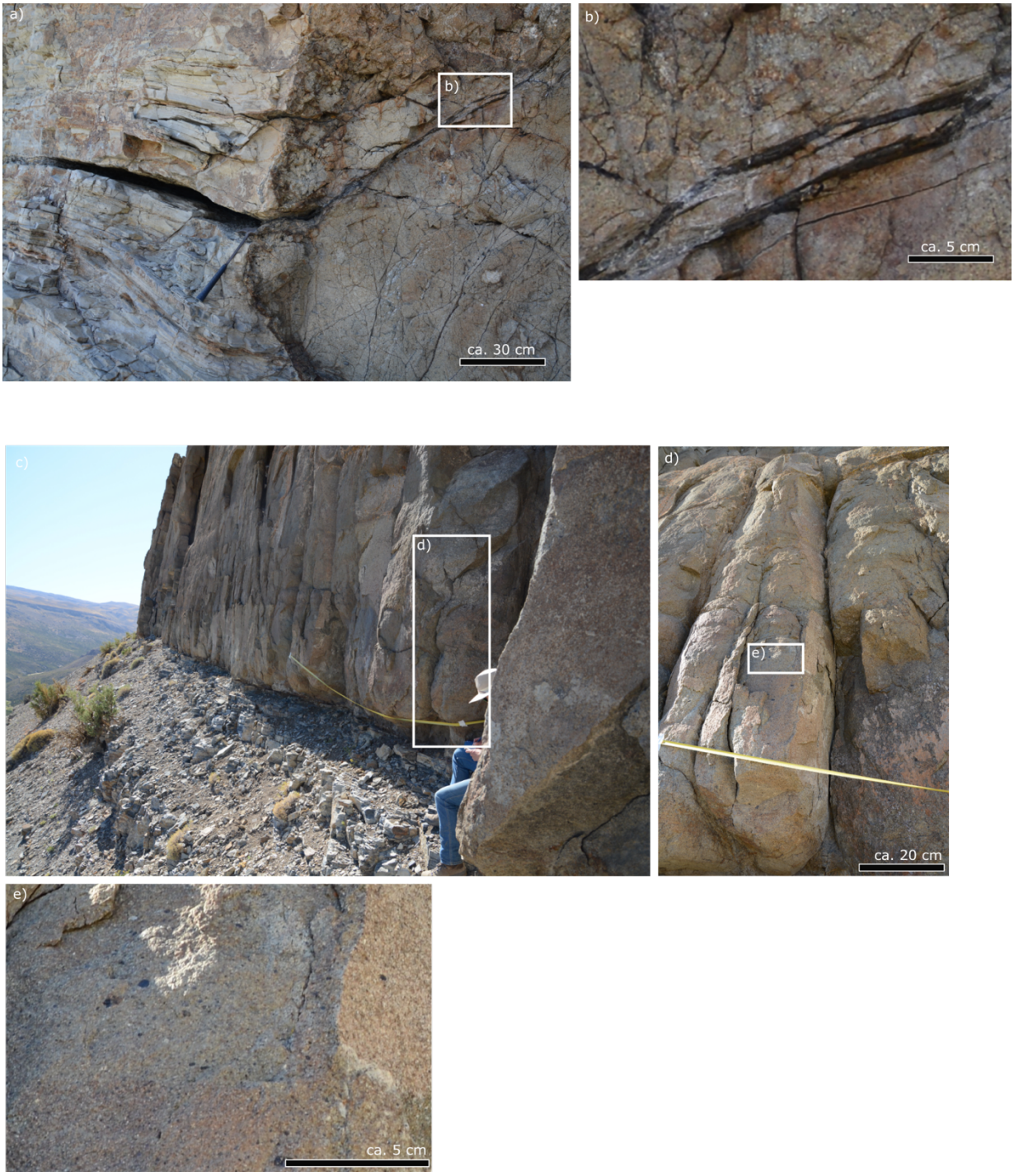

Figure 1. Photographs showing the difference in fracturing between areas affected by hydro-fracturing/injection of liquefied sediments (a,b) and areas with only cooling joints present (c-e). While the former show intense fracturing with calcite and bitumen fill at the cm and sub-cm scale, the latter exhibits intact intrusive rock at the same scale (except weathering-fractures related to so-called "onion-skin" weathering. We use this as an argument that areas dominated by cooling joints will not suffer from significant resolution bias.

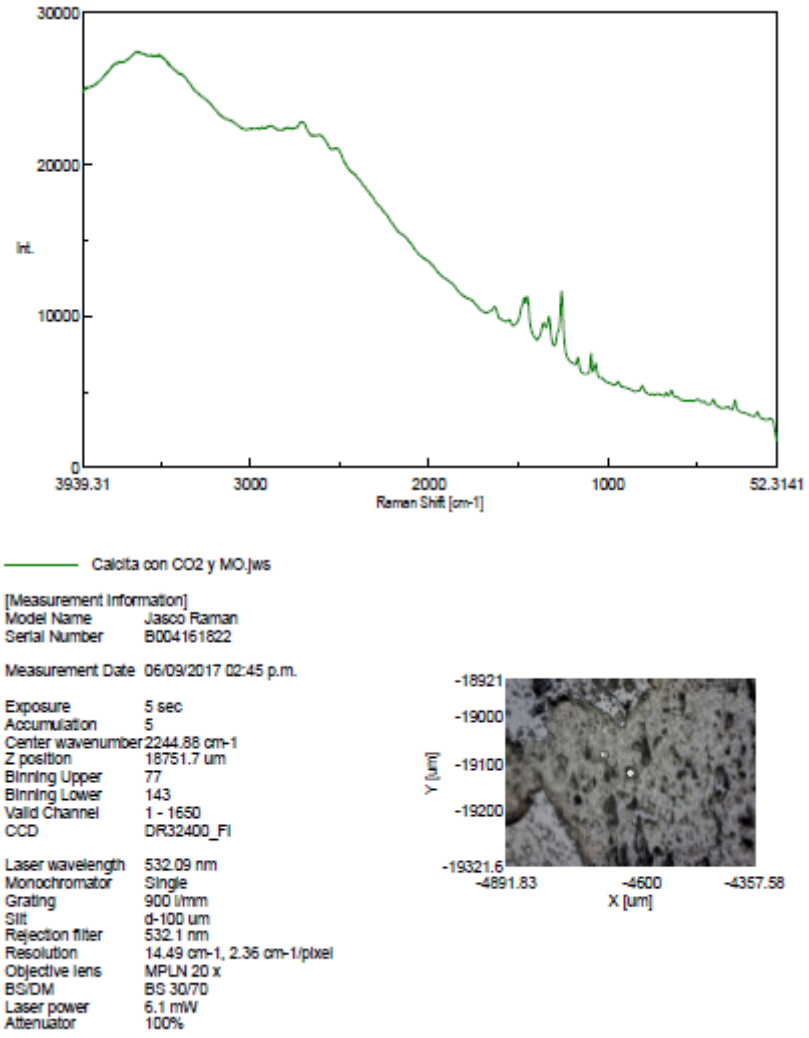

Figure 2. Raman spectrum of a calcite vein sample showing CO2 in fluid inclusions (peaks at ca. 1400 and 1300 cm^{-1}).

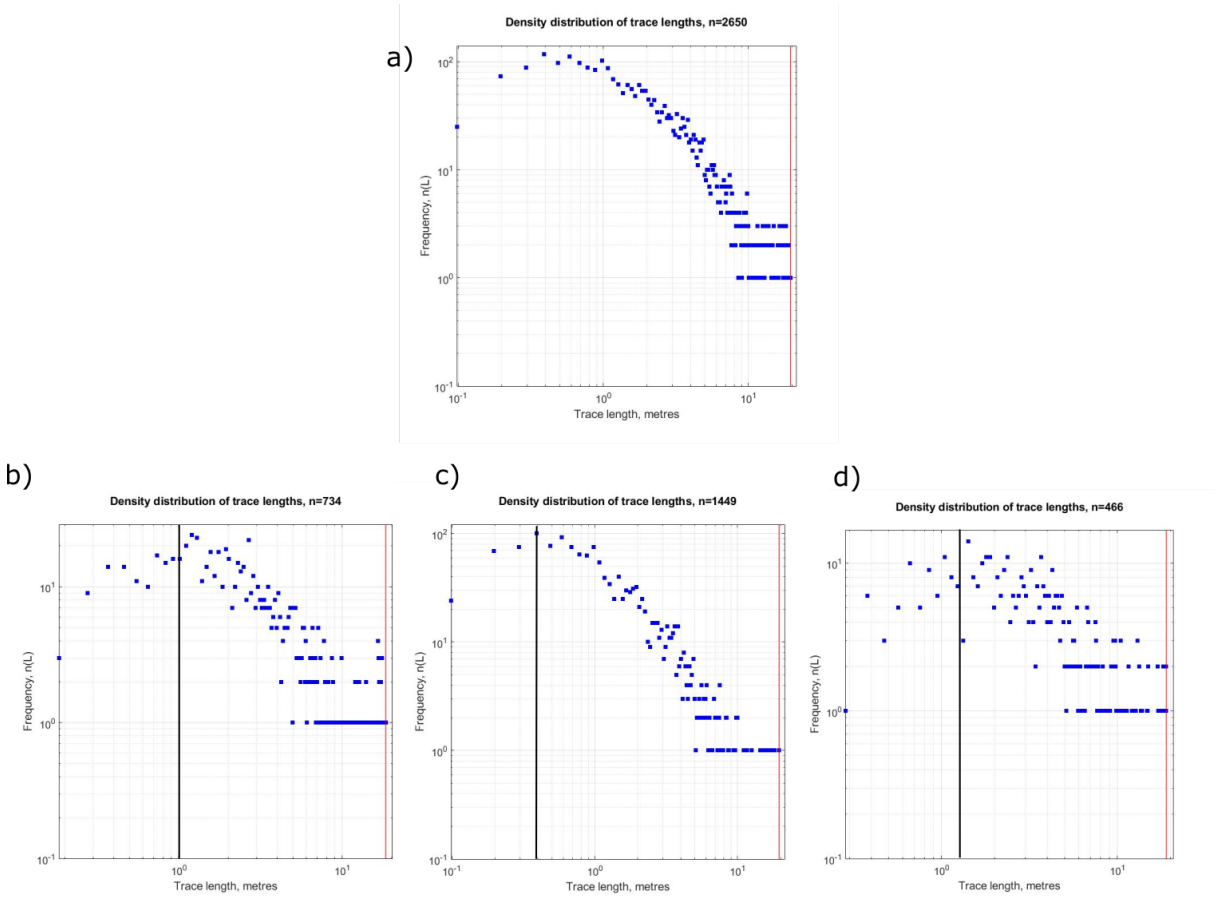

Figure 3. Density distribution of trace length for the fracture population mapped in for quantitative analysis (Fig.12, 13 in the main document). (a) Entire population, (b) left domain 0-90 m, (c) central domain 90-160m, (d) right domain 160-230m. The black horizontal line in (b-d) represents the local maximum, i.e. the length below which the fracture density decreases with decreasing length. This was suggested by Bonnet (2002) as a choice for lower cut-off to correct resolution bias in statistical analysis of trace lengths.

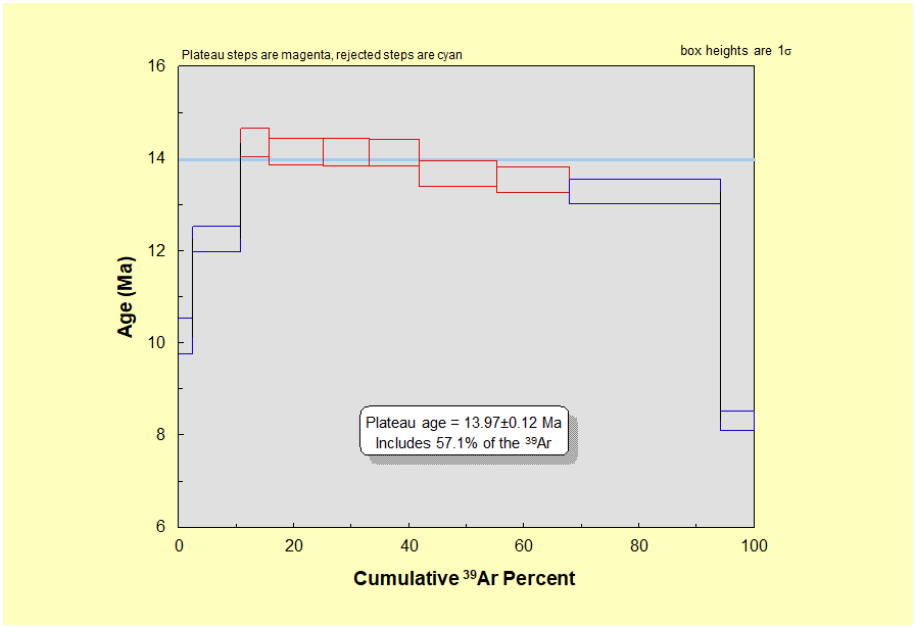

Figure 4. Ar-Ar dating of one of the sills at El Manzano, resulting in an age of 13.97 Ma.

A.3 Manuscript 3

III

Ole Rabbel, Mair, K., Galland, O., Grühser, C., Meier, T.
Numerical modeling of fracture network evolution in organic-rich shale with rapid internal fluid generation.
Journal of Geophysical Research: Solid Earth, 125, e2020JB019445. (2020)

AGU ADVANCING EARTH AND SPACE SCIENCE

JGR Solid Earth

RESEARCH ARTICLE
10.1029/2020JB019445

Numerical Modeling of Fracture Network Evolution in Organic-Rich Shale With Rapid Internal Fluid Generation

Ole Rabbel[1], Karen Mair[1], Olivier Galland[1], Carina Grühser[2], and Tobias Meier[2]

[1]Physics of Geological Processes, The NJORD Centre, Department of Geosciences, University of Oslo, Oslo, Norway, [2]geomecon GmbH, Berlin, Germany

Key Points:
- A propagating network of hydraulic fractures due to internal fluid production is modeled
- Results indicate three phases including (1) individual fracture growth, (2) fracture coalescence, and (3) overpressure relaxation
- External stress anisotropy controls overall orientation, and local stress redistribution controls coalescence

Supporting Information:
- Supporting Information S1

Correspondence to:
O. Rabbel,
ole.rabbel@geo.uio.no

Citation:
Rabbel, O., Mair, K., Galland, O., Grühser, C., & Meier, T. (2020). Numerical modeling of fracture network evolution in organic-rich shale with rapid internal fluid generation. *Journal of Geophysical Research: Solid Earth*, *125*, e2020JB019445. https://doi.org/10.1029/2020JB019445

Received 17 JAN 2020
Accepted 31 MAY 2020
Accepted article online 3 JUN 2020

Abstract When low-permeability and organic-rich rocks such as shale experience sufficient heating, chemical reactions including shale dehydration and maturation of organic matter lead to internal fluid generation. This may cause substantial pore fluid overpressure and fracturing. In the vicinity of igneous intrusions emplaced in organic-rich shales, temperatures of several hundred degrees accelerate these processes and lead to intense fracturing. The resulting fracture network provides hydraulic pathways, which allow fluid expulsion and affect hydrothermal fluid flow patterns. However, the evolution of these complex fracture networks and controls on geometry and connectivity are poorly understood. Here, we perform a numerical modeling study based on the extended finite element method to investigate coupled hydromechanical fracture network evolution due to fast internal fluid generation. We quantify the evolution of different initial fracture networks under varying external stresses by analyzing parameters including fracture length, opening, connectivity, and propagation angles. The results indicate a three-phase process including (1) individual growth, (2) interaction, and (3) expulsion phase. Magnitude of external stress anisotropy and degree of fracture alignment with the largest principal stress correlate with increased fracture opening. We additionally find that although the external stress field controls the overall fracture orientation distribution, local stress interactions may cause significant deviations of fracture paths and control the coalescence characteristics of fractures. Establishing high connectivity in cases with horizontally aligned initial fractures requires stress anisotropy with $\sigma_V > \sigma_H$, while the initial orientation distribution is critical for connectivity if stresses are nearly isotropic.

1. Introduction

Fracturing of rocks usually involves an interplay between external stresses, for example, tectonics far-field stresses, and pore fluid pressure. In the case of low-permeability sedimentary rocks such as shale, various geological processes may cause the buildup of strong pore fluid overpressure, which eventually leads to natural hydraulic fracturing (Bjorlykke, 2010; Cobbold & Rodrigues, 2007). These geological processes commonly include temperature-dependent chemical reactions such as mineral dehydration, generation of hydrocarbons through maturation of organic matter, or precipitation of minerals in the pore space (Aarnes et al., 2012; Kobchenko et al., 2011; Ougier-Simonin et al., 2016; Townsend, 2018). In otherwise impermeable rocks, the resulting fractures constitute pathways for efficient fluid migration. Therefore, these processes are considered essential for primary hydrocarbon migration, as well as hydrothermal fluid circulation in shale formations (Iyer et al., 2017; Ougier-Simonin et al., 2016; Panahi et al., 2019).

In a standard burial scenario, both hydrocarbon generation and mineral dehydration or precipitation are slow processes that can take millions of years, potentially leading to buoyancy driven (Jin & Johnson, 2008) or subcritical fracture propagation (Jin et al., 2010). The reaction rates can become much faster if magmatic intrusions are emplaced in organic-rich shale. The rapid heating leads to strong overpressure buildup and fracturing throughout the rocks surrounding the intrusion within a few years, or possibly even days or hours (Aarnes et al., 2012; Galerne & Hasenclever, 2019; Panahi et al., 2019).

Figure 1 illustrates this scenario, in which fractures may provide migration pathways for large amounts of hydrocarbon liquids and gases. These can be stored in subsurface reservoirs or emitted into the atmosphere through volcanic vents (Iyer et al., 2017; Spacapan et al., 2020). However, the dynamics of fracture network

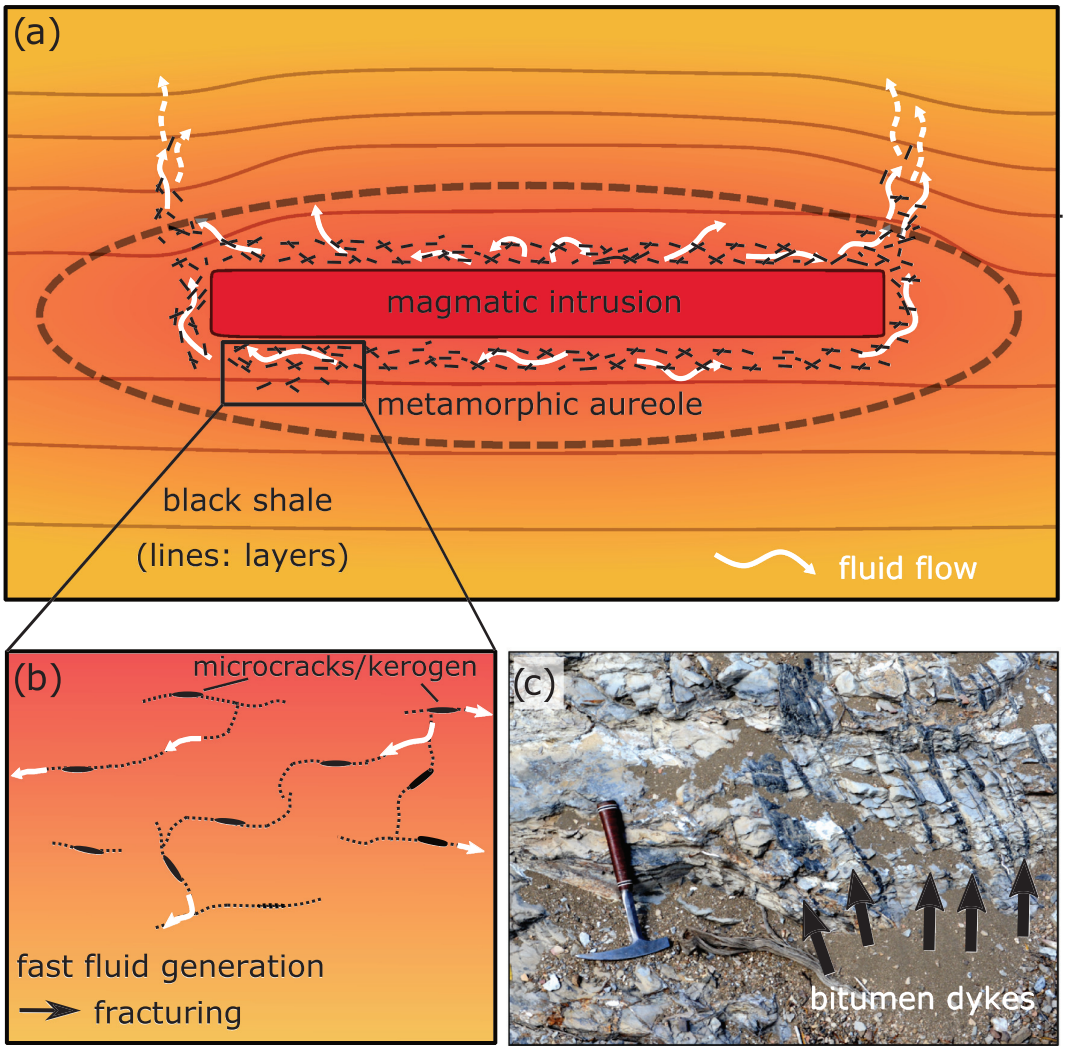

Figure 1. Schematic illustration of the processes related to strong heating of shale due to a magmatic intrusion. (a) Heat from the intrusion creates a metamorphic aureole with high chemical reaction rates. (b) Rapid fluid generation is thought to cause fast overpressure buildup and create a fracture network, which provides migration pathways for fluids. (c) Field example of bitumen dykes in shale matured by magmatic intrusions (Neuquén Basin, Argentina).

growth and its effect on fluid expulsion and transport properties in strongly heated shale are still poorly constrained. Thus, it is crucial to develop a quantitative understanding of the coupling between internal fluid generation and fracture network evolution.

Fractures representing fluid pathways in tight, organic-rich shales are well documented from both field and borehole data in both standard burial and volcanic settings (Marquez & Mountjoy, 1996; Ougier-Simonin et al., 2016; Spacapan et al., 2019; Zanella et al., 2015). However, our current understanding of hydrofracturing due to internal fluid generation stems primarily from laboratory models and a few numerical studies. Typically, the process observed in experiments can be subdivided into three phases, including (1) fracture initiation, (2) growth and coalescence, and (3) expulsion (Kobchenko et al., 2014; Panahi et al., 2018, 2019).

Experiments with heated shale indicate that fracture initiation on the microscale starts from small preexisting flaws that promote stress concentration, such as elliptic pores or kerogen patches in shale (e.g., Figueroa Pilz et al., 2017; Kobchenko et al., 2011; Panahi et al., 2019). Similar fracture initiation mechanisms were observed in analogue experiments using brittle, elastic gelatin-yeast mixtures, where a drainage fracture

network developed from elliptic gas bubbles (Kobchenko et al., 2014; Vega et al., 2018). Fracture propagation is thought to be driven by continuous liquid and gas production, and several factors may influence the propagation direction: (1) initial orientation of kerogen flakes or thin pores, for example, due to sedimentary lamination, (2) external stress field configuration, and (3) internal stress interactions (Kobchenko et al., 2011; Panahi et al., 2018; Vega & Kovscek, 2019; Vernik, 1994). Observations linked to fluid and gas expulsion in laboratory experiments include cyclic fluctuations of fracture apertures, that is, opening and closing, in response to fluid pressure buildup and relaxation due to fluid generation and burst-like expulsion (Kobchenko et al., 2014; Panahi et al., 2018, 2019).

Laboratory experiments are limited by time, scale, and cost. Additionally, quantification of the exact stress state during fracture network evolution remains challenging. Therefore, numerical studies represent an important tool to study complex fracture network evolution due to internal fluid generation in organic-rich rocks. To our knowledge, there are only two numerical studies of this type to date (Teixeira et al., 2017; Vega et al., 2018). Teixeira et al. (2017) focused on the influence of differential stresses and initial spacing and size of kerogen patches on the orientation and potential interconnectivity of newly formed microfractures around the patches. Meanwhile, Vega et al. (2018) presented a phase-field method to model systems similar to the gelatin models, establishing good agreement with the laboratory results and linking fracture network characteristics to the elastic properties of gelatin. However, the *evolution* of a fracture network and its relation to the stress state of a medium with internal fluid production has not been investigated thoroughly. To address this issue, we present a two-dimensional (2-D) numerical model study based on the extended finite element method (XFEM) for hydraulic fracturing, which we use to simulate propagation, coalescence, and drainage of multiple fractures due to internal fluid overpressure.

The main goal of our study is to present a workflow to quantify the evolution of fracture network parameters that can be related to the stress state of the coupled hydromechanical model. In this way, we aim to better understand the processes governing complex fracture propagation in organic-rich shale undergoing fast fluid generation due to strong heating and their potential influence on fluid expulsion and migration.

2. Methods

2.1. Modeling Framework

Numerical investigation of the evolution of a fracture network due to internal fluid generation in a rock requires coupling of mechanical deformation and fluid flow in an elastic solid, as well as fracture propagation, interaction, and coalescence. We therefore employ an existing XFEM-based research and development software (geomecon, 2019). XFEM is a popular numerical method used for modeling hydraulic fracture propagation, because it allows the intersection of a finite element mesh by discontinuities, that is, fractures, without the need for time-consuming remeshing (e.g., Belytschko et al., 2009; Fu et al., 2013; Lecampion et al., 2018). The software utilized in this study has previously been applied to investigate fracture network growth and fracture coalescence at the laboratory scale as well as for geotechnical applications (Backers et al., 2012, 2015; Mischo & Backers, 2012; Stöckhert, 2015). It solves the poroelastic formulation of linear elasticity

$$\nabla \cdot (\sigma(\boldsymbol{u})) + \boldsymbol{f} + \alpha \nabla P_p = 0, \tag{1}$$

where $\sigma(\boldsymbol{u})$ denotes stress, α represents Biot's effective stress coefficient (we use $\alpha = 1$), P_p is pore pressure, and $\boldsymbol{f}$ denotes the body force vector. With the help of Darcy's law, spatiotemporal pore pressure variations due to fluid flow and solid deformation are found by solving

$$\frac{\partial P}{\partial t} = \frac{M}{\mu} \nabla \cdot \left(\mathbf{k} \nabla \left(P_p - \rho_f \mathbf{g} \mathbf{x} \right) \right) + \alpha M \frac{\partial \epsilon_b}{\partial t}, \tag{2}$$

where M is Biot's modulus, μ is fluid viscosity, $\boldsymbol{k}$ denotes the permeability tensor, ρ_f is fluid density, $\boldsymbol{g}$ represents gravitational acceleration, and ϵ_b denotes bulk strain. Equations 1 and 2 provide the governing equations required to solve the coupled problem. Here, modeling is restricted to 2-D problems assuming plain strain.

Fracture propagation is implemented as quasistatic, using a combination of Griffith theory for tensile failure and a Mohr-Coulomb criterion for shear failure. This allows the use of reliable rock mechanical parameters (tensile strength, cohesion, and internal friction angle) that are readily available from published laboratory data (Dietrich, 2015; Schön, 2015). The stresses are evaluated in a semicircle around the crack tip, and if tensile or the Mohr-Coulomb failure envelope is exceeded at one or more points on the semicircle, the crack grows in the direction of the most critical stress value. This most critical value is defined as exceeding the critical stress by the largest percentage. If shear and tensile criteria are exceeded by the same amount, by default, tensile failure is realized.

2.2. Model Setup

Figure 2 illustrates our model setup including boundary conditions and geometry. The model includes a 50×50 cm square representing a vertical section in the subsurface, assuming plane strain conditions. We subdivide the square into two domains, which we refer to as the "model domain" and the "boundary domain," respectively. The model domain is populated with realistic rock properties for low-permeable organic-rich shale as described in Table 1. Note that although we use isotropic elastic properties and rock strength for simplicity, the modeling software in principle allows for anisotropic parameters. Within the boundary domain, we increased the rock strength and permeability to unrealistically high values, to (1) prevent fractures from connecting to the boundary, thus destroying the mesh and (2) allow drainage of overpressured fractures to the boundary domain upon connection. Elastic and fluid properties are identical in both domains. Fluid viscosity represents an order of magnitude estimate based on water to simulate low-viscosity behavior. In elements cut by fractures, we increase permeability by several orders of magnitude to allow for efficient fluid flow along fractures. This approach will not result in realistic fracture flow but mainly ensures that flow is focused in the fractures. At this time, more realistic, aperture-dependent fracture permeability according to cubic law (Witherspoon et al., 1980) is not implemented. However, we attempt to minimize the error of our approach by using a high-resolution mesh along the fractures.

Figure 2 also shows the predefined fractures in the initial state of the model. We added 25 fractures of 1 cm length in an evenly spaced grid throughout the inner model domain, that is, we omit a simulation of the fracture initiation process and assume that initial, small flaws have already formed. Laboratory studies show that such initial microcracks could form from ellipsoid pores or kerogen flakes (Kobchenko et al., 2011, 2014; Vega et al., 2018).

We start each simulation by pumping fluid into the fractures, which constitute internal model boundaries, at a rate of 5×10^{-9} m^3/s until all fractures start growing. Then, six fracture growth steps (4 mm growth per step) alternate with a single, short (1 s) flow step to allow for fluid pressure relaxation as well as drainage if a fracture connects to the boundary domain. There are several criteria to stop a simulation: (1) After a maximum of 105 calculation steps, that is, 15 growth-flow cycles, (2) all fractures are connected to the boundary domain and have been drained, or (3) all fractures cease growing. Note therefore that since different simulations may fulfill one of the criteria after a different number of computation steps, the simulations have a varying number of total steps.

2.3. Parameter Sensitivity Study

One objective of this study is to investigate fracture network evolution for various external stress states and initial fracture orientations. Therefore, we varied the initial orientation of the fractures in three configurations of increasing alignment with the horizontal axis, choosing a random value within 90°, 45°, and 15° from the horizontal axis, respectively. We refer to these three configurations as "random," "semialigned," and "aligned," respectively. In organic-rich shale, stronger alignment of microcracks with the horizontal axis could be a consequence of sedimentary lamination. For each case of the initial fracture geometry, we ran simulations with increasingly anisotropic stress boundary conditions, representing a constant depth of around 2.5 km. This approximately corresponds to the onset of the oil window as well as an intermediate emplacement depth for intrusions that could cause fast maturation of oil and gas (Spacapan et al., 2018, 2019). Starting from applying isotropic stress of 67.5 MPa along all boundaries, we decrease the horizontal stress by 1%, 5%, 10%, and 200%. We apply constant pore pressure of 25 MPa at the outer boundaries of the model. In a geologic sense, this corresponds to an increasingly extensional stress state at a constant depth with hydrostatic fluid pressure except in the fractures. The extreme case of 200% stress anisotropy is based on the

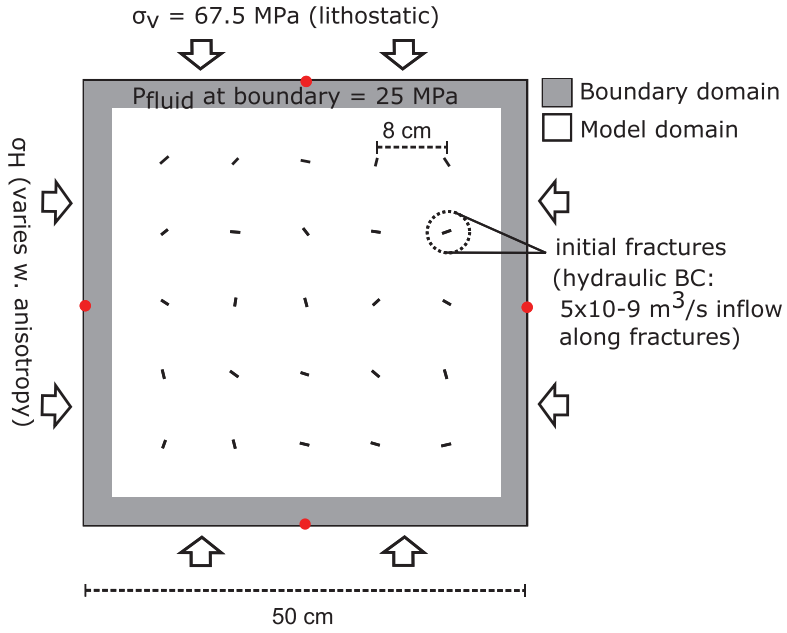

Figure 2. Illustration of the model setup and geometry. Arrows indicate stress boundary conditions, and red dots represent boundary nodes with zero boundary tangential displacement in addition. The inner model domain (white) has realistic physical parameters of shale, while the outer boundary domain (gray) has unrealistically high rock strength and is highly permeable to stop fracture growth and allow drainage.

theoretical consideration of an elastic medium with Poisson ratio of 0.25 under pure vertical compaction with no horizontal strain (e.g., Cobbold & Rodrigues, 2007). Since this case is somewhat unrealistic and mainly designed to give an extreme reference scenario, we mainly focus on the transition from isotropic to a mildly extensional stress state.

2.4. Quantification of Fracture Network Evolution

Presenting an approach to quantify the fracture network evolution and drainage dynamics is another important objective of this work. Accordingly, we extract specific parameters that describe the dynamics of fracture growth and potentially identify different phases, and characterize the connectivity of the final fracture pattern. As illustrated in Figure 3, the parameters include (1) total fracture length of the fracture network, (2) total fracture area, that is, aperture integrated along each fracture, (3) fracture propagation angle with respect to the horizontal, and (4) connections per line. Below, we will describe each parameter in more detail.

Table 1
Rock and Fluid Parameters Used for the Model

Parameter	Value (unit)
Permeability[b]	10^{-20} m^2
Fractures	10^{-12} m^2
Young's modulus[b]	23.9 GPa
Poisson's ratio[b]	0.17
Angle of internal friction[b]	0.543
Cohesion[b]	33.8 MPa
Tensile strength[c]	3 MPa
Biot's modulus[a]	10^{10} MPa
Pore fluid viscosity	10^{-3} Pa·s

Note. Mechanical properties represent averages of literature values, while for permeability, the lowest values were chosen to allow overpressure buildup. [a]Based on Cosenza et al. (2002). [b]Based on Dietrich (2015). [c]Based on Schön (2015).

First, we monitored the total fracture length from each step, which is straightforward using the resulting fracture node coordinates. In addition, we extracted the total fracture area per simulation step to identify trends in opening and closing of fractures during growth and drainage. Since the coordinates of the fracture nodes and the associated displacement on each side of the fracture are known for each calculation step, it is straightforward to construct open fractures as polygons and measure their area, which corresponds to fracture opening (gray area in Figure 3. Thus, we will use the terms fracture area and opening synonymously.

To measure the trends in the evolution of the fracture orientation, such as alignment with external stresses, we measured the median angle of all new crack elements with respect to the horizontal axis for every simulation step (see Figure 3; hereafter referred to as

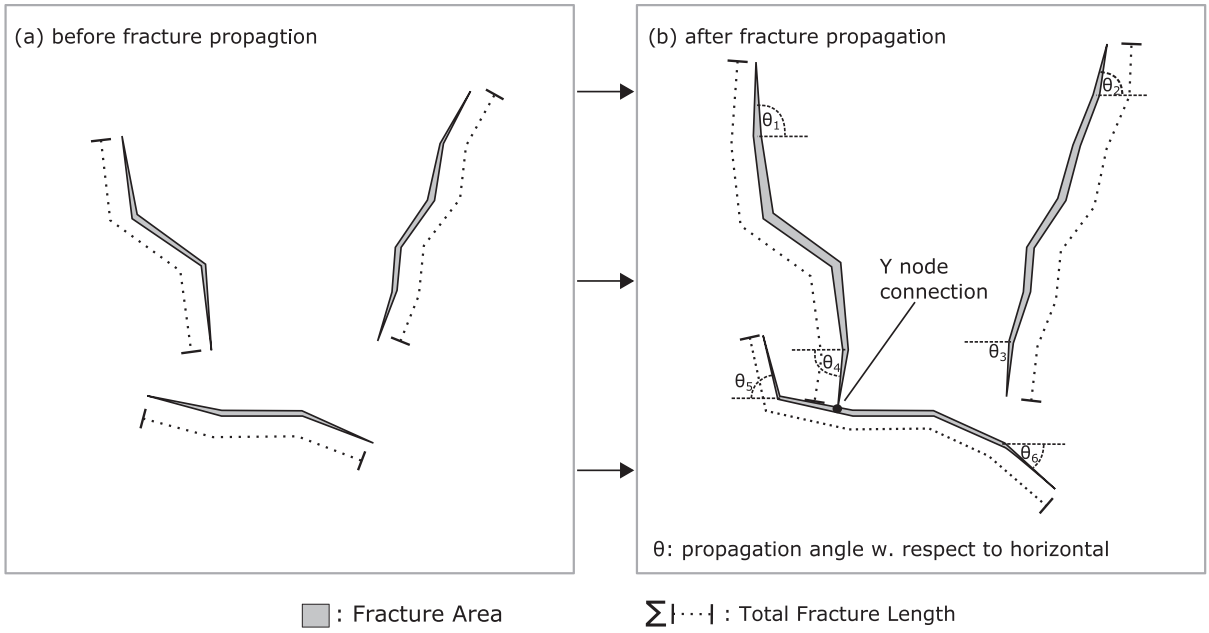

Figure 3. Schematic illustration of the quantities used to characterize fracture network evolution in this study. After each propagation step (from a to b), we calculate the fracture area (gray), total fracture length (sum of all fracture segment lengths), the angles of new fracture segments with respect to the horizontal, and the number of new connection nodes.

"propagation angle"). Due to the relatively small number of fractures in the model, we favor median over arithmetic average, since alignment trends are represented more clearly as median. To relate the evolution of the crack tip orientation to a physically relevant parameter, we plot the propagation angle against ratio of average fracture length to initial fracture spacing (around 8 cm in our case, cf. Figure 2). When this parameter approaches a value of 1, the average fracture length is approximately equal to initial fracture spacing, indicating that fracture interaction may play a role.

The connectivity of the drainage fracture network, in terms of both its evolution and final state, is of particular interest, since even closed fractures could be reopened by renewed pressure buildup as preexisting weaknesses. Here, we use the average number of connections per line C_L to quantify connectivity, which is a dimensionless parameter derived from fracture network topology (Sanderson & Nixon, 2018). C_L is calculated from the number of fracture lines (N_L) connecting nodes between fractures, that is, abutting (N_Y) and crossing (N_X) nodes as

$$C_L = 2(N_X + N_Y)/N_L. \tag{3}$$

While values of $C_L < 2$ indicate a fracture network with limited connectivity, $C_L > 3.57$ has been shown to be the percolation threshold where the entire fracture network is interconnected (Sanderson & Nixon, 2018). Note that in this study, we are analyzing a network with very few fractures and idealized initial positions of the fractures. Therefore, we are mainly interested in the relative connectivity trends of the simulations.

3. Results

3.1. Visualization of the Evolving Fracture Network

Figures 4–6 show time series snapshots for three different modeling cases representing the endmembers of the parameter study. These endmembers include random initial orientation under isotropic external stress (Figure 4), random initial orientation under 10% extensional stress anisotropy (Figure 5), and horizontally aligned initial fractures under 10% extensional stress anisotropy (Figure 6). Each figure consists of four snapshots displaying the state of the fracture network at the same four computation steps, representing various

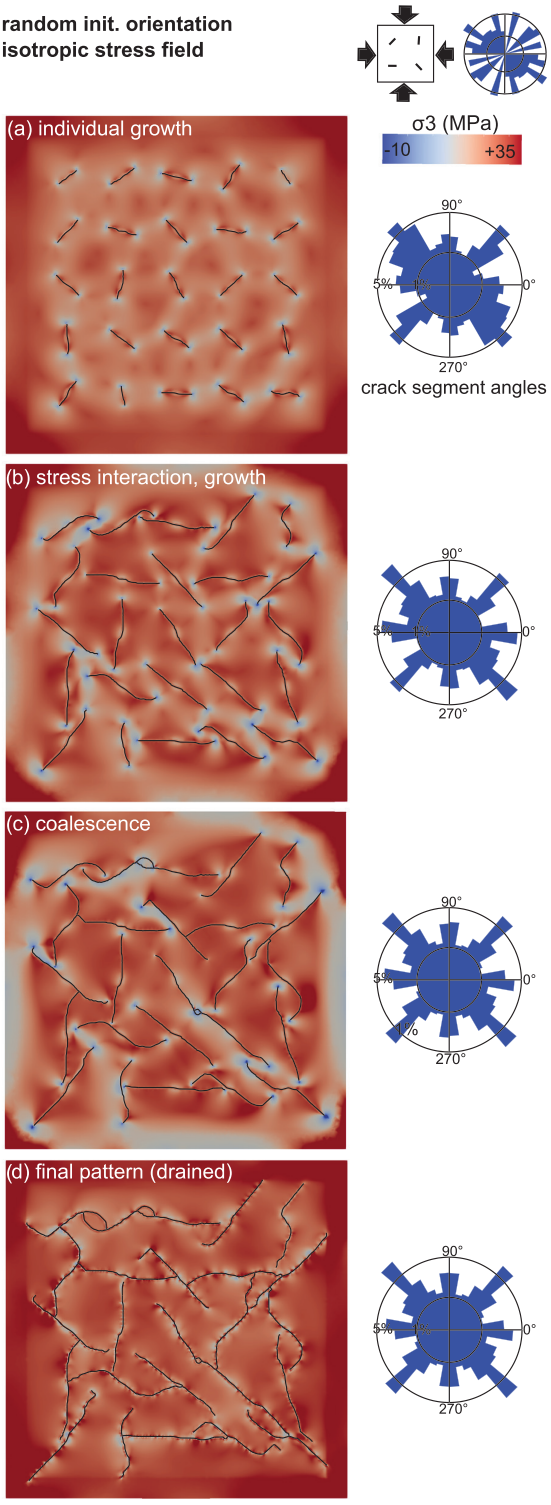

Figure 4. Time series of the fracture network evolution for random initial fracture orientation and isotropic external stress field, along with rose diagrams of all fracture segments for each step. Color code represents the smallest principal stress. Description of the phases (a–d) is given in the text.

development phases. The respective phases include individual (noninteractive) growth, stress interaction, fracture coalescence, and the final fracture pattern at the last computation step. The background color represents the smallest principal stress, with blue color corresponding to tensile stresses and red color corresponding to compressive stresses. For each snapshot, we additionally provide the corresponding orientation distribution of all fracture segments (one segment is defined by two nodes in the mesh) as a rose plot.

For the fracture network with random initial orientation developing under isotropic external stress, we mainly observe growth in the direction of the initial fractures in the individual growth phase (Figure 4a). When stress interactions between the fracture start to become significant, the direction of propagating fracture tips starts to deviate from the earlier paths. In particular, crack tips approaching each other are first deviated to opposite sides and then "embrace" each other, while fracture tips growing toward an open fracture surface deviate following a more orthogonal path toward that surface (Figure 4b). Fractures located near the edges of the model tend to grow toward the edges, which is likely a numerical boundary effect. As the fractures become longer, tensile stresses around their tips intensify. When the fractures start to interconnect in the coalescence phase, the connected tips lose their tensile tip stresses (Figure 4c). However, the stress state of the model is highly heterogeneous, with both highly compressive and tensile areas, especially when compared to the early phase. A visualization of the complexity of coalescence-related stress reconfigurations captured by the model is available in supporting information Figure S1. The final pattern shows a highly interconnected fracture network, which is connected to the boundary domain and therefore drained (Figure 4d). The displayed stress field is much more homogenous and purely compressive. For a better impression of the coupling between fracture drainage, opening/closing, and stress redistribution, we refer to Figure S2.

In the case with random initial orientation and 10% anisotropic extensional stress (Figure 5), we observe some differences compared to the previous case. During the individual growth, most fractures continuously turn toward the vertical direction, which is the direction of maximum externally applied stress (Figure 5a). This trend continues, until the fractures start interacting. We observe that the predominant type of interaction and coalescence is the previously described behavior of fracture tips "embracing" each other upon connection (Figures 5b and 5c). The fracture orientation distribution indicates that the connected fracture network is preferentially aligned in the vertical direction. The connected fracture arrays cause intense stress concentrations around them prior to drainage, creating zones of high compression around them and zones of extension close to the vertical model boundaries. In the final, drained model, the tensile stresses are relaxed and the entire model is under compression (Figure 5d).

The fracture network developing from initially aligned fractures (Figure 6) is characterized by an early growth phase where fractures first grow in an oblique path before turning to the vertical direction (Figure 6a). When the fractures start interacting and finally coalesce, they build fracture pathways that overall connect vertically but appear distinctly more tortuous compared to the previous case (Figures 6b and 6c).

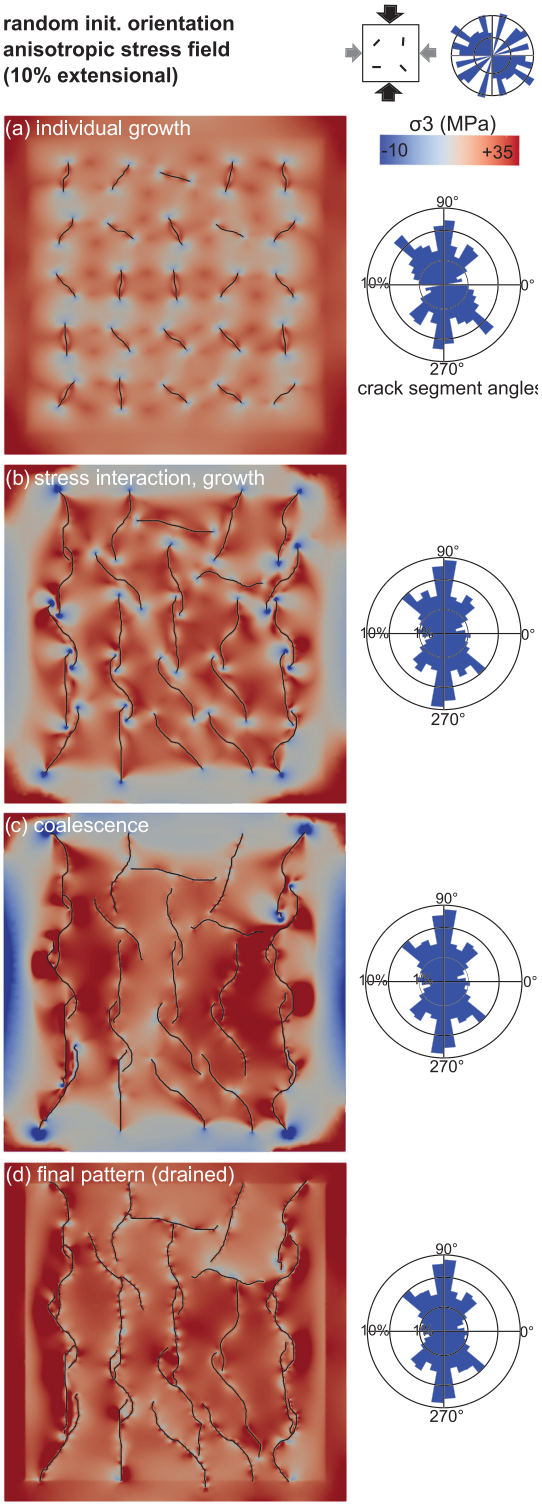

Figure 5. Time series and rose plots of the fracture network evolution for random initial fracture orientation and anisotropic stresses (10% extensional). The color code represents the smallest principal stress. Description of the phases (a–d) is given in the text.

This is expressed in the rose diagrams, which show similar numbers of oblique and vertical fracture segment orientations. Again, tensile stresses due to fluid overpressure disappear after drainage (Figure 6d).

3.2. Quantification of the Fracture Network Evolution

3.2.1. Total Fracture Length

Plotted against computation steps, the total fracture length follows a similar curve in all cases (Figure 7). Starting with linear growth until approximately Computation Steps 35–40 when all fractures propagate at both ends (gray domain, Figure 7), the increase in fracture length is continuously reduced afterwards until almost no growth is visible from around Step 50, when the most fractures have connected to each other or been drained upon connection to the boundary domain (white domain, Figure 7). While both the transition points between fracture growth phases and the values for the total fracture length are very similar for all stress anisotropy values in Figure 7a, we observe that the onset of the late phase of reduced growth is later for stronger initial alignment. Additionally, the final fracture network is characterized by larger total fracture length values for increasing initial alignment (Figure 7b).

3.2.2. Total Fracture Area (Opening)

As illustrated in Figure 8, the total fracture area develops in three distinct phases and additionally shows trends for varying stress anisotropy and initial fracture alignment. Each fracture propagation step usually leads to an increase in the total fracture area, while each decrease of the fracture area corresponds to a flow step associated with some pore pressure relaxation or even complete drainage in the later stages. This makes it easy to identify fluid flow steps in the presented data. Generally, the first phase, up to Computation Step 25, includes mild opening of the fractures during early fracture growth (dark gray background in Figure 8). Until around Calculation Step 40, the curves become increasingly steeper and the evolution of the fracture area diverges clearly for different simulation cases (light gray). In this second phase, we observe first coalescence, boundary domain connection, and drainage events, indicated by the letters C, B, and D in Figure 8. The third phase includes a strong, stepwise decrease in fracture area at each fluid flow step, leading to subsequent drainage and closure of the fractures (white). To illustrate the direct connection between the onset of fluid expulsion and the reduction in fracture area, we refer to a summary of the expulsed fluid volume given in Figure S5.

Although we are able to identify these general phases in all simulations, the individual evolution shows distinctions, particularly in the second and third phases, that is, during phases of fracture coalescence and drainage. For random initial orientation, an isotropic external stress field (black curve in Figure 8a) leads to much smaller growth in total area compared to 5% and 10% stress anisotropy, and the main reduction in open fracture area is distributed over different steps. The case of 10% extensional stress anisotropy is characterized by a very steep increase, and even though the first drainage event happens earlier compared to the other two cases (Calculation Step 36), this drainage step does not lead to a reduction in total fracture area. The second drainage step in this case, however, is associated with a dramatic decrease in fracture area, after which the total opening is actually smaller than in the other cases.

Figure 8b shows the effect of increasing horizontal alignment of the initial fractures. The blue curve is identical to that in Figure 8a, and we observe

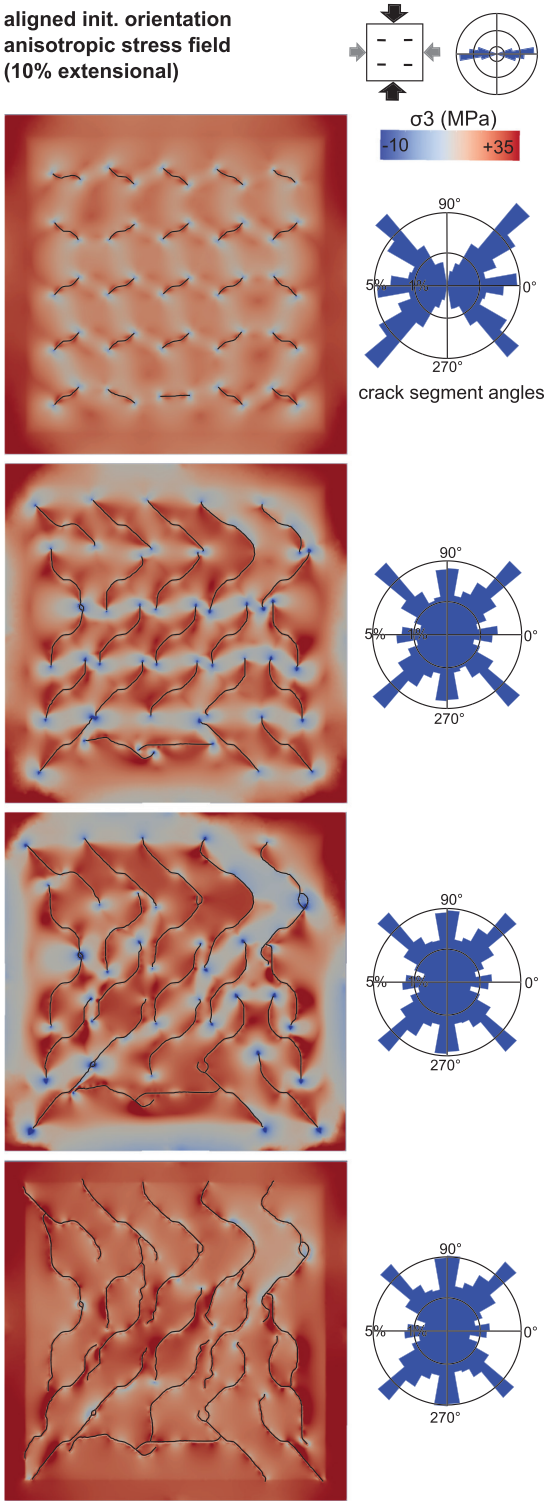

Figure 6. Time series of the fracture network evolution and its orientation distribution for initially aligned fractures in an anisotropic stresses (10% extensional). The color code represents the smallest principal stress. Description of the phases (a–d) is given in the text.

subsequent reduction of the maximum total fracture area with increasing alignment. In the semialigned case (yellow curve), we observe some variations during the phase of strong opening that are related to connecting fractures rather than fluid flow, followed by a strong decrease after the first drainage event. The open fractures of the aligned case (green curve) close over the course of several steps rather than a single event.

3.2.3. Propagation Angles

The evolution of the median angle of propagated fracture segments is illustrated in Figure 9. We display it as a function of the ratio of average fracture length to initial fracture spacing to have a proxy for the distance between fractures. Again, we recognize distinct phases. With the exception of isotropic external stress, the first phase reflects continuous alignment of propagating fractures with the vertical axis, corresponding to the maximum far-field stress direction. The degree of vertical alignment increases from none to a median propagation angle of around 80° when increasing stress anisotropy from 0% to 10% (Figure 9a). For constant 10% stress anisotropy, the median propagation angle reaches around 80° in all cases, but this maximum is reached at a higher average length value (Figure 9b). At a ratio of average length to initial spacing of around 1.1–1.4, the median propagation angle starts to decrease again and reaches values as low as 50°. For increasing initial alignment of the fractures, this minimum value is again shifted toward higher values of average length versus initial spacing. Finally, the curve becomes chaotic and average length does not increase significantly anymore, because of the reduced number of propagating crack tips. Note that Figure S3 provides additional information for all cases in the form of boxplots representing the shape of the propagation angle distribution. We find the observed shift in median angle is in fact an expression of a shift toward more vertical propagation angles for nearly all propagating fractures. In all cases with strongly anisotropic external stress, 75% of the fracture propagates at 60° or larger angles near the maximum of the median propagation angle (Figure S3).

3.2.4. Connectivity (Connections per Line)

We use measurements of average connections per line (C_L) to trace the evolution of connectivity in the fracture networks (Figure 10). In all simulations, the values stay at low values until around Calculation Step 30, when the first individual fractures coalesce. Such connection events cause the vertical steps seen in the connectivity curves.

For initially random fractures, we find that decreasing the differential stress leads to a systematic increase in fracture connectivity (C_L) from 1.2 for 10% stress anisotropy, 1.3 for 5% stress anisotropy, to 1.8 for the isotropic case (Figure 10a). Note that C_L does not capture anisotropy in the connectivity, although we do observe this anisotropy qualitatively (cf. Figures 4d and 5d for visualization of the respective final fracture networks). The isotropic case also exhibits the largest number of connection events.

The sensitivity of connectivity to increasing initial alignment is less obvious in our results (Figure 10b). With 10% stress anisotropy applied, the semialigned case shows highest connectivity ($C_L = 1.6$), while initially random fractures lead to the lowest values. The spread of values is slightly smaller than in Figure 10a). Figure 11 presents a summary of the final connectivity value for all combinations of stress anisotropy and initial fracture orientation tested in this study. For random initial orientation and no or small stress anisotropy (<5%), we observe a peak in fracture

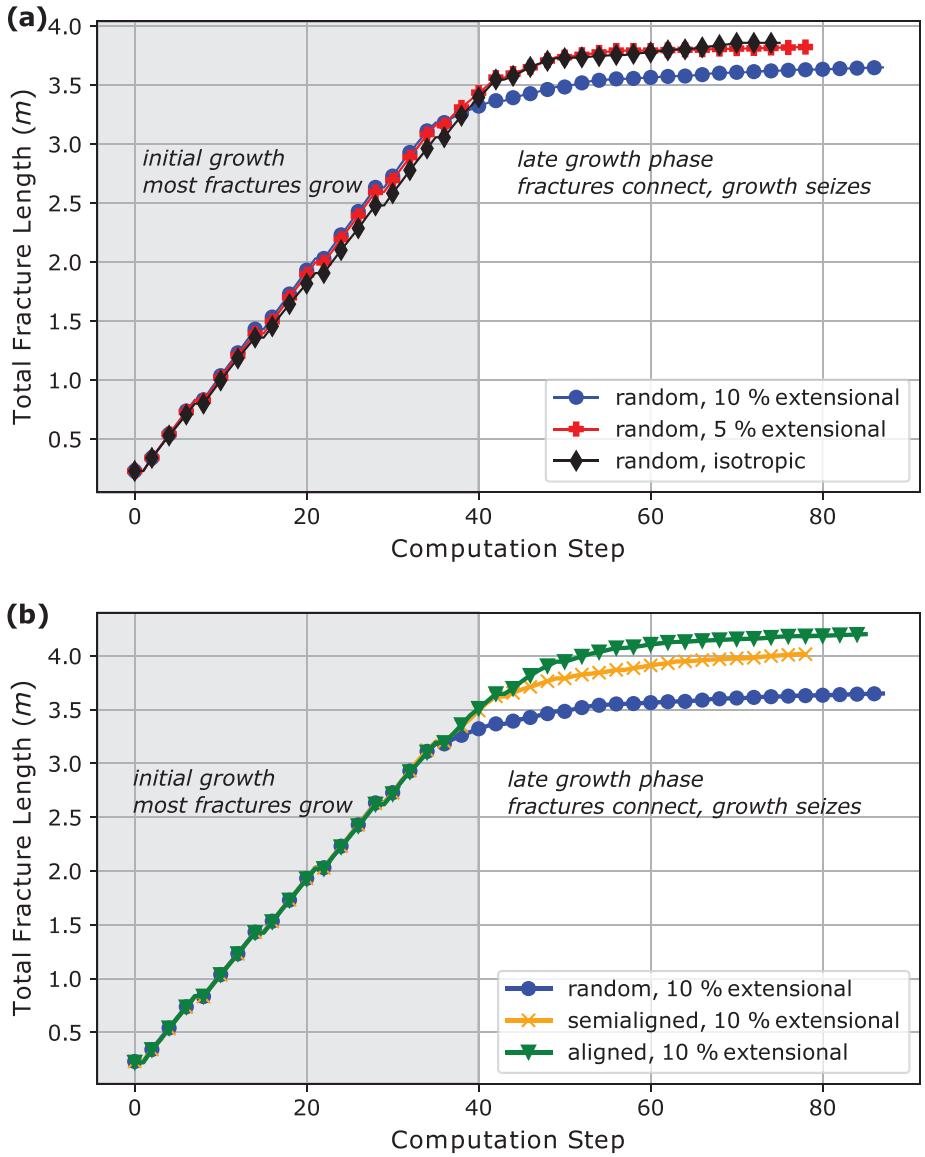

Figure 7. Total length of the fracture network for varying degrees of extensional stress anisotropy for an initially random fracture orientation (a) and varying initial fracture orientations at a given differential stress (10% extensional) (b).

connectivity. Increasing alignment of initial fractures is accompanied by a shift of the maximum value to 5% stress anisotropy, with low connectivity values at both isotropic and strongly anisotropic external stress.

4. Interpretation

4.1. Distinct Phases of the Fracture Network Evolution

We interpret the fracture network evolution in our models to be divided into three phases: (1) early phase of individual fracture growth, (2) intermediate phase of fracture interaction and initial coalescence, and (3) late phase of coalescence, fluid expulsion, and closure of the fractures.

During the early phase (until around Calculation Step 25), the propagation characteristics of individual fractures can be understood using simple fracture mechanics principles. Fluid pressure in all fractures is

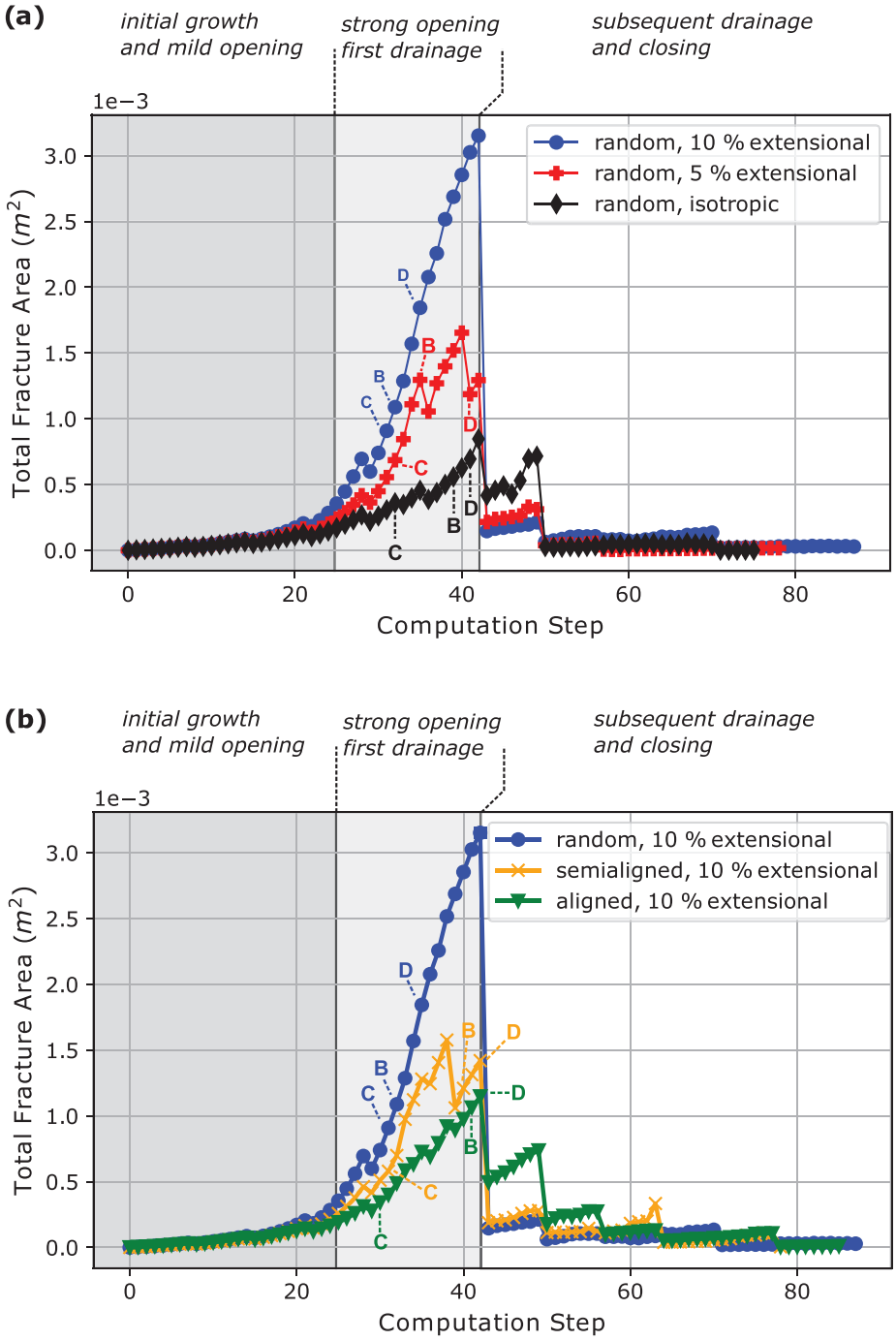

Figure 8. Total fracture area (aperture), for varying degrees of extensional stress anisotropy for an initially random fracture orientation (a) and varying initial fracture orientations at a given differential stress (10% extensional) (b). The letters C, B, and D mark the calculation step number for the first coalescence, boundary domain connection, and drainage event, respectively.

sufficient to cause tensile propagation of all fractures, leading to a linear increase in total fracture length (Figure 7). While the increase in fracture area is small (Figure 8), the early growth phase is the stage in which the dominant orientation of the fractures is established. For low stress anisotropy (<5%), initial

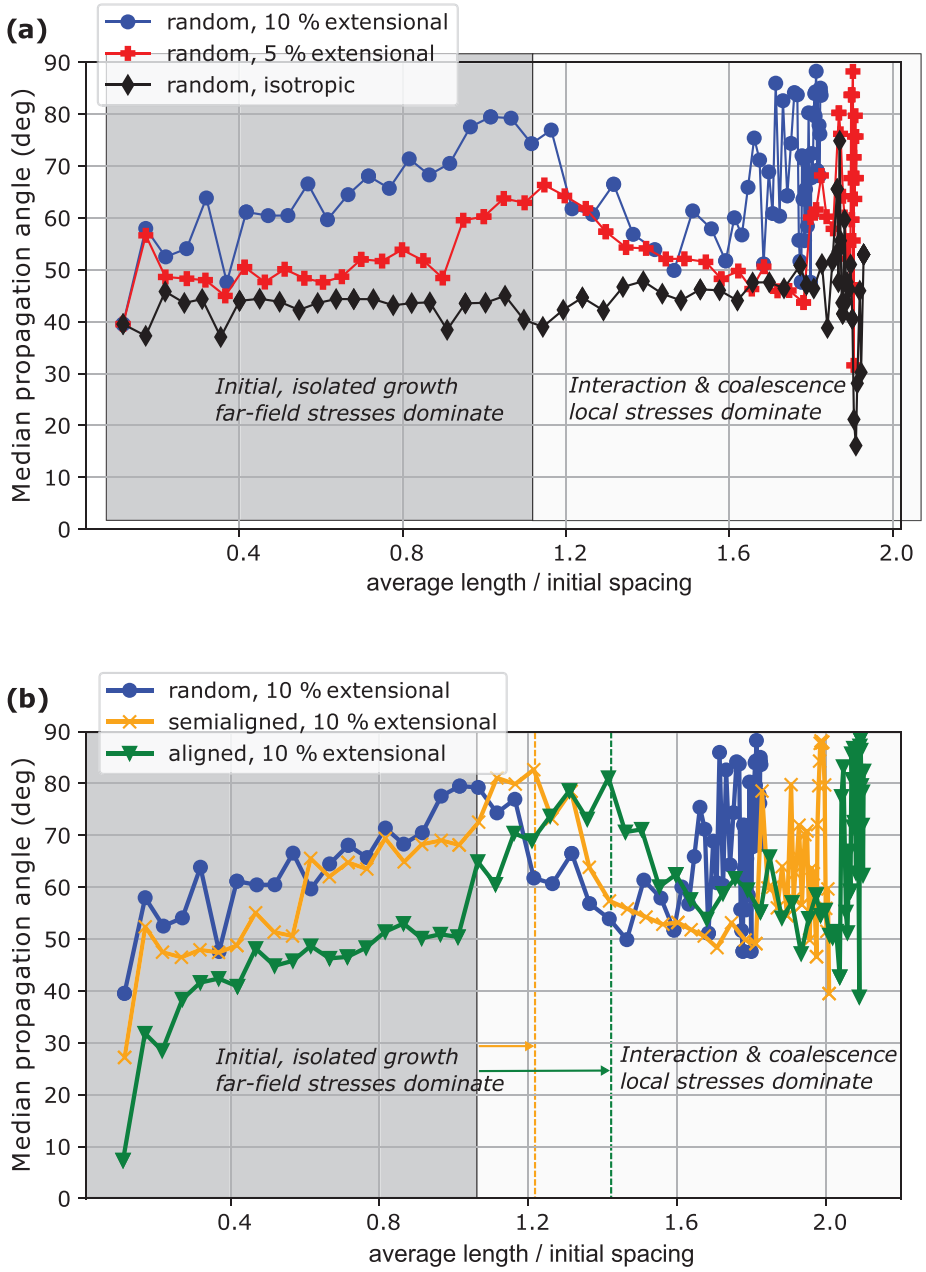

Figure 9. Median propagation angle with respect to the horizontal versus the ratio of average fracture length to the initial spacing. (a) Increasing differential stress from 0% (isotropic) to 10% extensional. (b) Comparison of random, semialigned, and aligned initial crack orientation for a 10% extensional stress configuration.

fracture orientation dominates the orientation of fracture propagation, while increasing differential stress leads to progressive alignment of propagating fractures parallel to the maximum external stress direction (Figures 9 and S3).

The second phase (until approximately Step 40) is characterized by the onset of stress interactions between growing fractures and initial coalescence, as well as a strong increase in fracture area. The interaction of stress fields of different fractures is clearly visible in Figures 4b, 4c, 5b, 5c, 6b, and 6c. Jumps in connectivity indicate coalescence events, because the longest fracture path length increases (Figure 10). The deviation of

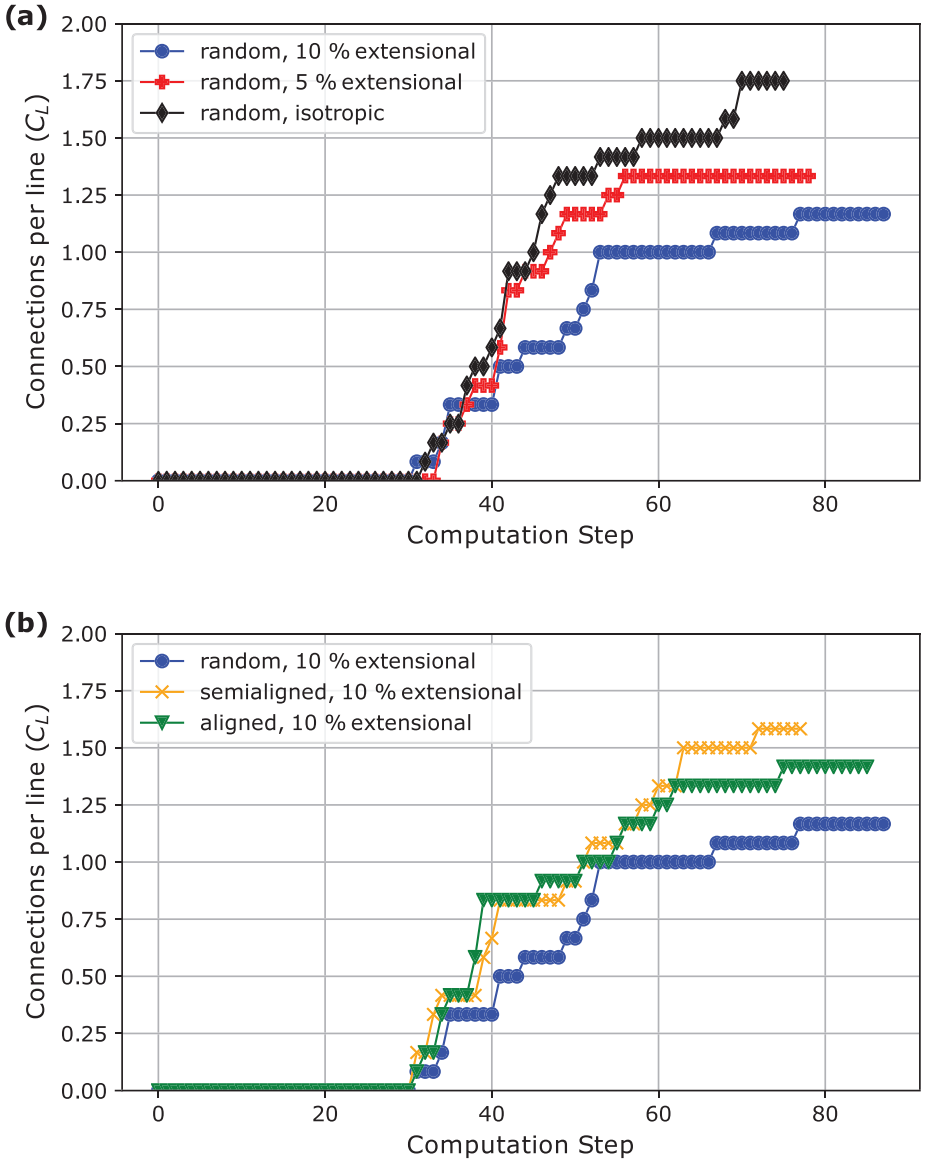

Figure 10. Development of fracture network connectivity (connections per line, C_L). The curves correspond to increasing differential stress (extension) for random initial fracture orientation (a) and increasing initial fracture alignment for an extensional stress field (b). For the random initial configuration, we observe a decrease in connectivity for increasing stress anisotropy (a), while variations in initial alignment do not show a clear trend (b).

propagation angles from their initial trend of alignment with maximum stress direction correlates with the ratio of fracture to initial spacing becoming significantly larger than 1 (Figure 9). Since this ratio expresses a high fracture density and indicates that fractures are likely approaching each other, we argue that the shift in the propagation angle trend is caused by the dominance of local stress interactions over far-field stresses. As an additional identifier, the fracture area increases along a much steeper curve compared to the previous phase, and the curves for the various cases of stress anisotropy start to diverge significantly (Figure 8). We will address the controls on fracture area for the various cases in a later section. Note that the total fracture length (Figure 7) is largely insensitive to this part of the fracture network evolution, highlighting the need for utilizing different parameters.

The final stage comprises further coalescence events that establish the final connectivity as well as the drainage and closure of the fractures. The combination of drainage-related stress relaxation and coalescence

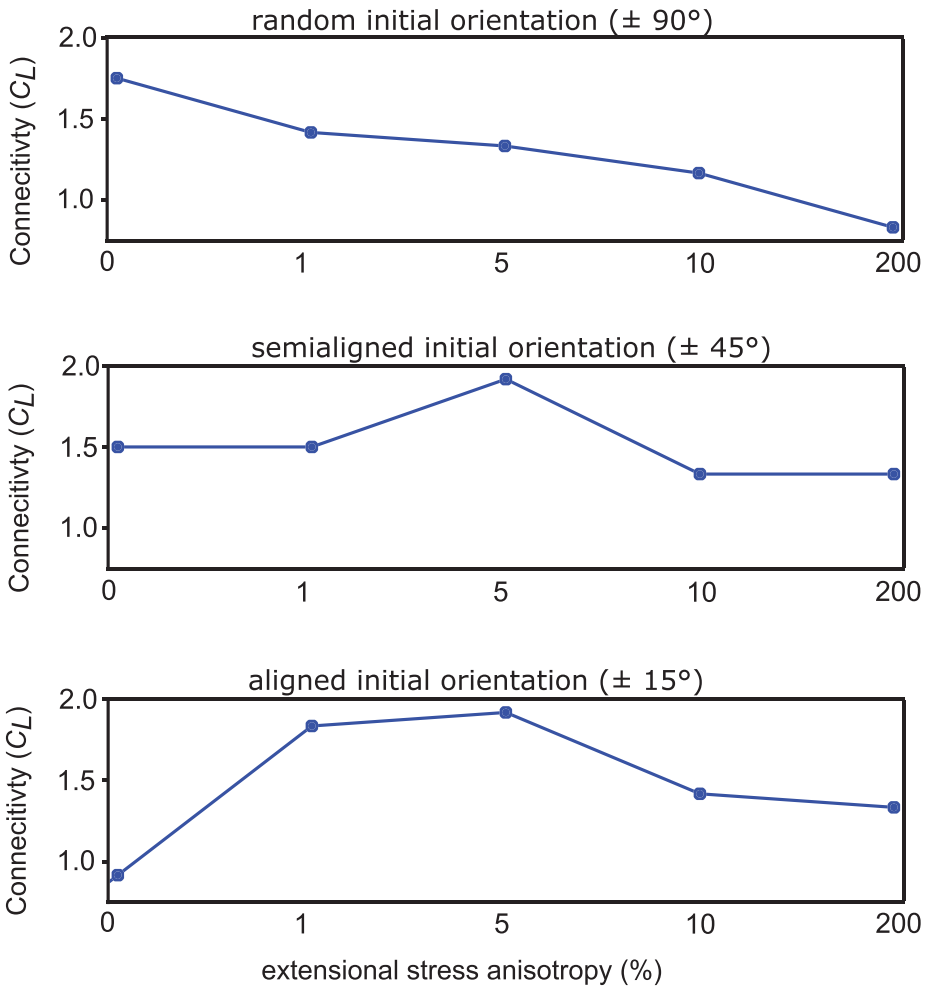

Figure 11. Summary of final connectivity in terms of average connections per line (C_L) for all initial orientations and stress states. For a random initial orientation, increasing extensional stress anisotropy results in subsequently lower connectivity. A connectivity peak at 5% stress anisotropy characterizes the semialigned and aligned cases.

events (steps visible in Figure 10) leads to a strongly decelerated growth in total fracture length (Figure 7), since fewer fracture tips are available for propagation. Due to the decreasing number of propagating fracture tips, the statistics of propagation angles become highly chaotic (Figures 9 and S3). The strong, stepwise reduction of fracture area during flow calculation steps is a result of drainage events resulting from connection of fractures to the boundary domain. The onset of fluid flow through the boundary of the model domain supports this interpretation (Figures S4 and S5). By the end of each simulation, the fracture area has returned to its initial value, implying that all excess fluid pressure has been released from the fractures (Figure 8). This also explains the transition to an entirely compressional and relatively homogenous stress state throughout the model (Figures 4c, 4d, 5c, 5d, 6c, and 6d). Note that due to the permanently established high-permeability connection of fractures to the boundary domain, renewed pressure buildup and fracture opening is not possible.

To sum up, we interpret each simulation to represent a cycle encompassing initial fracture growth, followed by subsequent interaction and coalescence, and finally fluid overpressure relaxation (expulsion) and fracture closure. The interpretation and relation to the stress state of the model is only possible through a combination of various parameters and visualization of the stress state of the model.

4.2. Factors Affecting Fracture Area (Opening)

One of the measured parameters presented in this study that goes beyond typically presented fracture network characteristics is the fracture area, or opening. Since the width of an open fracture severely affects its transport properties, this parameter is particularly interesting. Figure 8 shows two clear trends for the relative scaling of fracture areas during the main phase of fracture growth, especially in the second phase prior to main drainage: (1) Stronger differential stress leads to larger fracture area, and (2) stronger initial alignment of fractures orthogonally to the largest external stress direction leads to smaller fracture area.

Generally, larger normal stress acting on fracture surfaces leads to progressive closing of fractures and vice versa (e.g., Jaeger et al., 2009). Since we create stress anisotropy by reducing horizontal stress in order to simulate different scenarios at the same depth, we can expect fractures in more anisotropic stress fields to show higher fracture area values. Note that this also means that the depth of investigation, that is, changing vertical stress, will also affect opening. However, the different simulations only diverge significantly during the second phase, that is, after initial growth. Thus, an additional factor is needed to explain the large differences between scenarios. The vertical alignment of the fractures is much stronger for larger differential stresses (Figure 9a, cf. Figures 4 and 5). Considering an anisotropic stress field, fractures oriented more toward the direction of maximum stress experience less normal stress on their surfaces. Thus, we argue that it is the combination of preferential alignment and reduced horizontal stress that causes the differences in fracture area in the cases displayed in Figure 8a. The decrease in fracture area with stronger horizontal alignment of initial fractures (Figure 8b) can also be explained by the overall orientation distributions of the fracture segments. In the aligned case, the fracture network includes many subhorizontal fracture segments in its highly tortuous fracture paths (cf. Figure 6), which experience stronger normal stresses due to vertical σ_1.

Furthermore, the temporal evolution of the fracture opening is influenced by fracture coalescence and drainage. Since coalescence events generally lead to longer connected fractures, they typically lead to stronger opening. However, stress redistributions may also lead to the closure of dead ends, or neighboring fractures due to increased compression along the newly connected fracture (illustrated in Figure S1). Therefore, coalescence events (steps in Figure 10) can sometimes lead to a measurable reduction in total fracture area in some cases (e.g., red and orange curves in Figure 8). Finally, the expulsion controls the subsequent closure of the fracture network under the confining stress, due to the reduction of pore pressure after drainage. Note that the decrease in fracture area is not correlated with the amount of expulsed fluid but a result of the reconfiguration of the stresses in the model.

4.3. Fracture Connectivity

Since fracture network connectivity can be expected to have a strong impact on fluid flow, understanding the controlling parameters is especially important. A well-connected, percolating fracture network should also comprise connected fractures from different "rows" and "columns" of the regular grid of initial fractures (cf. Figure 2), since otherwise the connectivity is highly directional.

In the case of random initial orientation, connectivity systematically decreases with increasing stress anisotropy (Figure 10). Strong differential stress leads to pronounced alignment of propagating fractures with the largest principal stress, such that fractures only connect in the vertical direction (Figures 4 and 9a). In contrast, fractures propagate in the direction of their initial orientation when the external stresses are isotropic, leading to a highly interconnected network of fractures in this case (Figure 5). As a result of this effect, the simulations with random initial fracture orientation show highest connectivity of the final fracture network for isotropic and very mildly anisotropic stress (Figure 11, upper graph).

For increasing initial fracture alignment, we observe a shift of the maximum connectivity toward higher differential stresses (Figure 11, middle and lower graphs). A reasonable explanation is that a vertical σ_1 is required to deviate the subhorizontal fractures away from their initial path and create connectivity in the vertical direction (Figure 9b). In other words, the fractures need to rotate to be able to connect to upper and lower neighbors. For very strong differential stresses, however, this rotation may happen quickly, such that again exclusively vertical connections are formed, and the connectivity is directional and low. However, it is noteworthy that although the connectivity for the aligned case under strong differential stress is low

(Figure 10b), Figure 6 shows qualitatively that fractures do connect in different directions. Additionally, we see qualitatively that the fracture traces in this case are highly tortuous, which is also a result of the interplay between initial orientation and subsequent rotation under differential stress (Figure 6). Due to their importance to transport properties, we aim to include additional measures of directional connectivity and tortuosity in future studies.

5. Discussion

5.1. Evolution of Drainage Fracture Networks in Strongly Heated Shale

Improving our understanding of the formation of fracture networks in strongly heated, organic-rich shale requires models that can relate the evolution of a fracture network to the stresses within a rock due to fluid generation and subsequent crack propagation. Our modeling and analysis approach reveals characteristic phases of fracture network evolution in response to the stress state and how each parameter reacts to changing boundary and initial conditions. Adapting some of the parameters used in the laboratory studies of Kobchenko et al. (2014) and extending the analysis by the evolution of propagation angles proved crucial to identify the specific phases of the process (Figures 7–10). Thus, our work provides a numerical tool to quantitatively investigate the evolution of a fracture network in a rock with fast internal fluid generation and overpressure buildup, such as strongly heated shale in the vicinity of magmatic intrusions (e.g., Aarnes et al., 2012; Spacapan et al., 2018).

The present study aims at testing our model against existing knowledge of the process and additionally investigates the effect of varying stress boundary conditions and the orientation of initial fractures. The characteristics of the phases of fracture network evolution as described in the interpretation section are in good agreement with results from previously published laboratory experiments. Based on time-lapse synchrotron imaging of heated, immature shale samples (Kobchenko et al., 2011; Panahi et al., 2018), a three-stage process model was proposed: (1) Fractures initiate from thin kerogen flakes or around elongated pores, then (2) propagate and coalesce, preferentially along lamination planes, but sometimes also obliquely, and (3) finally close under confinement after the hydrocarbons have been expulsed. A similar behavior was documented in analogue experiments analyzing CO_2 production in impermeable, elastic gelatin-yeast-sugar gels, though at a larger model scale, which is more comparable to our numerical setup. Fractures formed at the edges of thin, ellipsoidal gas bubbles, then grew and connected, and finally drained through the boundary and stopped growing (Kobchenko et al., 2013, 2014; Vega & Kovscek, 2019). Similar to the behavior in our numerical results, fluctuations in the fracture area are related to fluid overpressure buildup and relaxation (Kobchenko et al., 2014). Thus, we conclude that our model correctly captures the dynamics of the process and may be used to gain addition quantitative understanding that is not available from experiments. For instance, we are able to extend the understanding of the process by demonstrating the relative importance of crucial parameters such as far-field stress anisotropy, local stress redistributions, and alignment of fractures on the characteristics of the fracture network in each phase. We will address these effects in separate sections below.

5.2. Controls on Fracture Growth and Geometry

Understanding the controlling factors that influence the final fracture network geometry is important, as the geometry controls bulk rock properties such as permeability. The general trend of stronger alignment of propagating fractures in the direction of σ_1 with increasing differential stress (Figures 9 and S3) is expected and represents the dominant control on the final orientation distribution (cf. Teixeira et al., 2017). However, our models yield additional insight into the role of stress interactions between fractures and their effect on fracture coalescence. While fracture tips connecting into walls of neighboring fractures at roughly orthogonal angles tend to stay on their path, two approaching fracture tips are deviated by local stress redistribution and grow into each other after the tips pass each other (Figures 4c, 5c, 6c, and S1). This “embrace” has previously been identified as one of the potential modes of hydraulic fracture coalescence (e.g., Wang, 2016) and is the key to identifying the onset of the overall coalescence phase of the fracture network as a whole (Figure 9). However, the transition might be less clear in real rocks where not all fractures undergo the same phases simultaneously. Qualitatively, similar observations were made in laboratory experiments. The photoelastic properties of gelatin allow visualization of stress fields around the fractures, showing that propagating fracture tips are deviated due to interacting stresses between fractures and that tensile tip stresses vanish

upon coalescence (Kobchenko et al., 2014; Vega et al., 2018). However, our numerical results add the benefit of providing a quantitative analysis of the stress state during the coalescence process (cf. Figure S1), which experimental visualization technique does not allow for. Overall, our results emphasize that local stress redistribution may play an important role for fracture coalescence, which influences the connectivity of fractures.

5.3. Controls on Connectivity and Flow Properties

Since fluid expulsion from strongly heated organic-rich shale is mainly controlled by fractures, an important goal is to link fracture network evolution to hydraulic rock properties. In this context, our simulations indicate that differential stress proves important to create higher connectivity in rocks with pronounced layering (Figures 10 and 11). However, the increasing alignment of fractures with the maximum stress direction will likely lead to a strongly anisotropic permeability structure if fractures dominate the fluid flow, especially for strongly anisotropic stress fields. Teixeira et al. (2017) report similar findings using discrete element modeling of shale at the millimeter scale. Under low differential stress, however, our results show that inclined initial flaws can be essential to create fracture connectivity in the vertical direction, since external stresses do not cause rotation of propagating fractures in this direction. This mode of connectivity creation was previously hypothesized by Panahi et al. (2018) but not investigated systematically. Therefore, if the local stress state is not strongly anisotropic, orientation of initial flaws on the microscale may be an important control on the fracture network geometry and thus fluid transport properties. However, since igneous intrusions may cause both local stress perturbations and induce damage due to host rock deformation (Haug et al., 2018; Scheibert et al., 2017; Schmiedel et al., 2019), assessment of realistic boundary and initial conditions is crucial to model the evolving fracture network. Note also that the effects of other parameters such as elastic and strength anisotropy should be investigated in future studies, as they may significantly alter the stress state and direction of propagating fractures.

5.4. Model Limitations

Finally, we will outline some important model limitations. First, the regular grid of fractures in our model setup does not reflect a realistic distribution in a rock, and part of the response might be influenced by the setup, for example, due to a pressure shielding effect of aligned fractures. However, even this simplified setup demonstrates complex fracture interaction phenomena as well as reasonable general trends in the measured parameters and is thus a useful baseline for future realistic setups tuned to investigate specific parameters such as the positioning and density of initial fractures. Additionally, the modeling software ignores the effect of fracture aperture on fracture permeability. Although this may influence flow rates, the coupling between fluid expulsion, opening and closing of fractures, and stress state is included in a physically meaningful way. Importantly, this limitation prevents hydraulic healing of fractures and renewed opening, such that fluid pressures do not build up again. Finally, due to the 2-D nature of our model, additional fracture interactions in the third dimension are not represented. On the other hand, 2-D results are easy to comprehend and visualize and a valuable tool to inform future 3-D studies.

6. Conclusions

In this study, we present a 2-D XFEM numerical model to investigate fracture network evolution in rocks with fast internal fluid generation, overpressure buildup, and expulsion, such as would be expected in strongly heated organic-rich shale close to magmatic intrusions. We integrate analysis of the stress state of the model with tracking of the evolution of specific parameters representing fracture network geometry, including total fracture length, fracture area, connectivity, and propagation angles. Our main conclusions are as follows:

1. The evolution of different fracture network characteristics reveals a three-phase process in our numerical models, comprising (i) initial individual fracture growth dominated by far-field stresses, (ii) interaction and coalescence dominated by local stress redistribution around the fractures, and (iii) fluid expulsion and stress relaxation. This is in good agreement with laboratory experiments at different scales.
2. Magnitude of external stress anisotropy and alignment of the fractures with the largest principal stress direction correlate with the maximum fracture opening.

3. While external stress field configuration controls the main characteristics of the fracture orientation distribution, local stress interactions may cause significant deviations of fracture paths and thus control the coalescence of fractures.
4. In order to create high connectivity in cases with horizontally aligned initial fractures (corresponding to layered rocks), stress anisotropy with $\sigma_V > \sigma_H$ is required. On the other hand, strongly inclined initial fractures are critical for high connectivity if stresses are fully or very nearly isotropic.
5. Strongly anisotropic far-field stresses lead to highly directional connectivity, which may translate to anisotropic fracture permeability.

Data Availability Statement

All data are available from the following repository: https://osf.io/pwjva/ (DOI 10.17605/OSF.IO/PWJVA).

Acknowledgments
We acknowledge funding through the EarthFlows Strategic Research Initiative of the University of Oslo (Universitetet i Oslo) and the Research Council of Norway (Grant no. 267775). We thank geomecon GmbH for access to the numerical code roxol used in this study. We thank Maya Kobchenko for her suggestions for the analysis workflow design.

References

Aarnes, I., Podladchikov, Y., & Svensen, H. (2012). Devolatilization-induced pressure build-up: Implications for reaction front movement and breccia pipe formation. *Geofluids*, *12*(4), 265–279. https://doi.org/10.1111/j.1468-8123.2012.00368.x

Backers, T., C. Gruehser, T. Meier, and G. Dresen (2012), Fracture pattern of borehole breakouts in shale—Comparison of physical and numerical experiments, Paper Presented at 74th EAGE Conference and Exhibition incorporating EUROPEC 2012.

Backers, T., T. Meier, P. Gipper, and O. Stephansson (2015), 2015:30 Technical Note, Rock Mechanics—Assessing the likelihood and extent of fracture growth in the KBS-3 repository at Forsmark, Technical Report Rep., 143 pp.

Belytschko, T., Gracie, R., & Ventura, G. (2009). A review of extended/generalized finite element methods for material modeling. *Modelling and Simulation in Materials Science and Engineering*, *17*(4), 043001. https://doi.org/10.1088/0965-0393/17/4/043001

Bjorlykke, K. (2010). *Petroleum geoscience: From sedimentary environments to rock physics*. Berlin: Springer Science & Business Media. https://doi.org/10.1007/978-3-642-02332-3

Cobbold, P. R., & Rodrigues, N. (2007). Seepage forces, important factors in the formation of horizontal hydraulic fractures and bedding-parallel fibrous veins ('beef' and 'cone-in-cone'). *Geofluids*, *7*(3), 313–322. https://doi.org/10.1111/j.1468-8123.2007.00183.x

Cosenza, P., Ghoreychi, M., De Marsily, G., Vasseur, G., & Violette, S. (2002). Theoretical prediction of poroelastic properties of argillaceous rocks from in situ specific storage coefficient. *Water Resources Research*, *38*(10), 1207. https://doi.org/10.1029/2001WR001201

Dietrich, A. B. (2015), The impact of organic matter on geomechanical properties and elastic anisotropy in the Vaca Muerta shale, Ph.D. Thesis, Colorado School of Mines. Arthur Lakes Library.

Figueroa Pilz, F., Dowey, P. J., Fauchille, A.-L., Courtois, L., Bay, B., Ma, L., et al. (2017). Synchrotron tomographic quantification of strain and fracture during simulated thermal maturation of an organic-rich shale, UK Kimmeridge Clay. *Journal of Geophysical Research: Solid Earth*, *122*, 2553–2564. https://doi.org/10.1002/2016JB013874

Fu, P., Johnson, S. M., & Carrigan, C. R. (2013). An explicitly coupled hydro-geomechanical model for simulating hydraulic fracturing in arbitrary discrete fracture networks. *International Journal for Numerical and Analytical Methods in Geomechanics*, *37*(14), 2278–2300. https://doi.org/10.1002/nag.2135

Galerne, C. Y., & Hasenclever, J. (2019). Distinct degassing pulses during magma invasion in the stratified Karoo Basin—New insights from hydrothermal fluid flow modeling. *Geochemistry, Geophysics, Geosystems*, *20*, 2955–2984. https://doi.org/10.1029/2018GC008120

geomecon (2019), roxol—The fracture network evolution simulator [Computer software], retrieved from www.roxol.de

Haug, Ø. T., Galland, O., Souloumiac, P., Souche, A., Guldstrand, F., Schmiedel, T., & Maillot, B. (2018). Shear versus tensile failure mechanisms induced by sill intrusions: Implications for emplacement of conical and saucer-shaped intrusions. *Journal of Geophysical Research: Solid Earth*, *123*, 3430–3449. https://doi.org/10.1002/2017JB015196

Iyer, K., Schmid, D. W., Planke, S., & Millett, J. (2017). Modelling hydrothermal venting in volcanic sedimentary basins: Impact on hydrocarbon maturation and paleoclimate. *Earth and Planetary Science Letters*, *467*, 30–42. https://doi.org/10.1016/j.epsl.2017.03.023

Jaeger, J. C., Cook, N. G., & Zimmerman, R. (2009). *Fundamentals of rock mechanics*. New York: John Wiley & Sons.

Jin, Z. H., & Johnson, S. E. (2008). Primary oil migration through buoyancy-driven multiple fracture propagation: Oil velocity and flux. *Geophysical Research Letters*, *35*, L09303. https://doi.org/10.1029/2008GL033645

Jin, Z.-H., Johnson, S. E., & Fan, Z. Q. (2010). Subcritical propagation and coalescence of oil-filled cracks: Getting the oil out of low-permeability source rocks. *Geophysical Research Letters*, *37*, L01305. https://doi.org/10.1029/2009GL041576

Kobchenko, M., Hafver, A., Jettestuen, E., Galland, O., Renard, F., Meakin, P., et al. (2013). Drainage fracture networks in elastic solids with internal fluid generation. *EPL (Europhysics Letters)*, *102*(6), 66002. https://doi.org/10.1209/0295-5075/102/66002

Kobchenko, M., Hafver, A., Jettestuen, E., Renard, F., Galland, O., Jamtveit, B., et al. (2014). Evolution of a fracture network in an elastic medium with internal fluid generation and expulsion. *Physical Review E*, *90*(5), 052801. https://doi.org/10.1103/PhysRevE.90.052801

Kobchenko, M., Panahi, H., Renard, F., Dysthe, D. K., Malthe-Sørenssen, A., Mazzini, A., et al. (2011). 4D imaging of fracturing in organic-rich shales during heating. *Journal of Geophysical Research*, *116*, B12201. https://doi.org/10.1029/2011JB008565

Lecampion, B., Bunger, A., & Zhang, X. (2018). Numerical methods for hydraulic fracture propagation: A review of recent trends. *Journal of Natural Gas Science and Engineering*, *49*, 66–83. https://doi.org/10.1016/j.jngse.2017.10.012

Marquez, X. M., & Mountjoy, E. W. (1996). Microfractures due to overpressures caused by thermal cracking in well-sealed Upper Devonian reservoirs, deep Alberta Basin. *AAPG Bulletin*, *80*(4), 570–588.

Mischo, H., and T. Backers (2012), Analysis of fracture coalescence by fracture mechanics numerical simulation, Paper Presented at ISRM International Symposium-EUROCK 2012, International Society for Rock Mechanics and Rock Engineering.

Ougier-Simonin, A., Renard, F., Boehm, C., & Vidal-Gilbert, S. (2016). Microfracturing and microporosity in shales. *Earth-Science Reviews*, *162*, 198–226. https://doi.org/10.1016/j.earscirev.2016.09.006

Panahi, H., Kobchenko, M., Meakin, P., Dysthe, D. K., & Renard, F. (2018). In-situ imaging of fracture development during maturation of an organic-rich shale: Effects of heating rate and confinement. *Marine and Petroleum Geology*, *95*, 314–327. https://doi.org/10.1016/j.marpetgeo.2018.05.002

Panahi, H., Kobchenko, M., Meakin, P., Dysthe, D. K., & Renard, F. (2019). Fluid expulsion and microfracturing during the pyrolysis of an organic rich shale. *Fuel*, *235*, 1–16. https://doi.org/10.1016/j.fuel.2018.07.069

Sanderson, D. J., & Nixon, C. W. (2018). Topology, connectivity and percolation in fracture networks. *Journal of Structural Geology*, *115*, 167–177. https://doi.org/10.1016/j.jsg.2018.07.011

Scheibert, J., Galland, O., & Hafver, A. (2017). Inelastic deformation during sill and laccolith emplacement: Insights from an analytic elastoplastic model. *Journal of Geophysical Research: Solid Earth*, *122*, 923–945. https://doi.org/10.1002/2016JB013754

Schmiedel, T., Galland, O., Haug, Ø. T., Dumazer, G., & Breitkreuz, C. (2019). Coulomb failure of Earth's brittle crust controls growth, emplacement and shapes of igneous sills, saucer-shaped sills and laccoliths. *Earth and Planetary Science Letters*, *510*, 161–172. https://doi.org/10.1016/j.epsl.2019.01.011

Schön, J. H. (2015). *Physical properties of rocks: Fundamentals and principles of petrophysics*. New York: Elsevier.

Spacapan, J., Palma, J., Galland, O., Manceda, R., Rocha, E., D'Odorico, A., & Leanza, H. (2018). Thermal impact of igneous sill-complexes on organic-rich formations and implications for petroleum systems: A case study in the northern Neuquén Basin, Argentina. *Marine and Petroleum Geology*, *91*, 519–531. https://doi.org/10.1016/j.marpetgeo.2018.01.018

Spacapan, J. B., D'Odorico, A., Palma, O., Galland, O., Rojas Vera, E., Ruiz, R., et al. (2020). Igneous petroleum systems in the Malargüe fold and thrust belt, Río Grande Valley area, Neuquén Basin, Argentina. *Marine and Petroleum Geology*, *111*, 309–331. https://doi.org/10.1016/j.marpetgeo.2019.08.038

Spacapan, J. B., D'Odorico, A., Palma, O., Galland, O., Senger, K., Ruiz, R., et al. (2019). Low resistivity zones at contacts of igneous intrusions emplaced in organic-rich formations and their implications on fluid flow and petroleum systems: A case study in the northern Neuquén Basin, Argentina. *Basin Research*, *32*(1), 3–24. https://doi.org/10.1111/bre.12363

Stöckhert, F. (2015), Fracture mechanics applied to hydraulic fracturing in laboratory experiments, Ruhr-Universität Bochum.

Teixeira, M. G., Donzé, F., Renard, F., Panahi, H., Papachristos, E., & Scholtès, L. (2017). Microfracturing during primary migration in shales. *Tectonophysics*, *694*, 268–279. https://doi.org/10.1016/j.tecto.2016.11.010

Townsend, M. R. (2018). Modeling thermal pressurization around shallow dikes using temperature-dependent hydraulic properties: Implications for deformation around intrusions. *Journal of Geophysical Research: Solid Earth*, *123*, 311–323. https://doi.org/10.1002/2017JB014455

Vega, B., & Kovscek, A. R. (2019). A systematic study of internal gas generation in shale source rocks using analog experiments. *Journal of Petroleum Science and Engineering*, *173*, 209–221. https://doi.org/10.1016/j.petrol.2018.10.006

Vega, B., J. Yang, H. A. Tchelepi, and A. R. Kovscek (2018), Investigation of stress field and fracture development during shale maturation using analog rock systems, Paper Presented at SPE Annual Technical Conference and Exhibition, Society of Petroleum Engineers.

Vernik, L. (1994). Hydrocarbon-generation-induced microcracking of source rocks. *Geophysics*, *59*(4), 555–563. https://doi.org/10.1190/1.1443616

Wang, H. (2016). Numerical investigation of fracture spacing and sequencing effects on multiple hydraulic fracture interference and coalescence in brittle and ductile reservoir rocks. *Engineering Fracture Mechanics*, *157*, 107–124. https://doi.org/10.1016/j.engfracmech.2016.02.025

Witherspoon, P. A., Wang, J. S. Y., Iwai, K., & Gale, J. E. (1980). Validity of cubic law for fluid flow in a deformable rock fracture. *Water Resources Research*, *16*(6), 1016–1024. https://doi.org/10.1029/WR016i006p01016

Zanella, A., Cobbold, P. R., Ruffet, G., & Leanza, H. A. (2015). Geological evidence for fluid overpressure, hydraulic fracturing and strong heating during maturation and migration of hydrocarbons in Mesozoic rocks of the northern Neuquén Basin, Mendoza Province, Argentina. *Journal of South American Earth Sciences*, *62*, 229–242. https://doi.org/10.1016/j.jsames.2015.06.006

JGR Solid Earth

Supporting Information for

Numerical Modeling of Fracture Network Evolution in Organic-Rich Shale with Rapid Internal Fluid Generation

Ole Rabbel[1], Karen Mair[1], Olivier Galland[1], Carina Grühser[2], Tobias Meier[2]

[1] Physics of Geological Processes, The NJORD Centre, Department of Geosciences, University of Oslo, Box 1047, Blindern, 0316, Oslo, Norway

[2] geomecon GmbH, Chausseestraße 88, 10115 Berlin, Germany.

Corresponding author: Ole Rabbel (ole.rabbel@geo.uio.no)

Contents of this file

Figures S1 to S5

Introduction

The presented supplementary data include four figures. Figures S1, S2 and S4 are visualizations of the simulation made in Paraview. The data presented in Figures S3 and S5 were extracted from the result xml-files using a Python script provided in the data repository (see acknowledgements in the main submission). For the permeability ellipses in Figure S5, we used the fracture nodes

Figures S1-S2 are visualizations intended to demonstrate the high level of complexity and detail captured in the model. We present them to provide additional support for our observation and interpretation of the role of local stress redistribution after during coalescence and drainage for the propagation behavior our propagating fractures.

Figure S3 shows the distribution of propagation angles for all cases presented in the manuscript. The figure thus provides additional information beyond the comparison of median propagation angles displayed in Figure 9 of the main document.

Figure S4 illustrates an example of the fluid flow field within the interconnected fracture network associated with relaxation of the fluid overpressure in the fractured by expulsion into the boundary domain.

S5 presents the outward flow through from the model into the boundary domain per flow step normalized by the sum of all steps.

For S4 and S5 the reader should keep in mind that the permeability is not modelled as aperture dependent. Therefore, the curve should be understood as a phenomenological visualization rather than a realistic quantification of the expulsion.

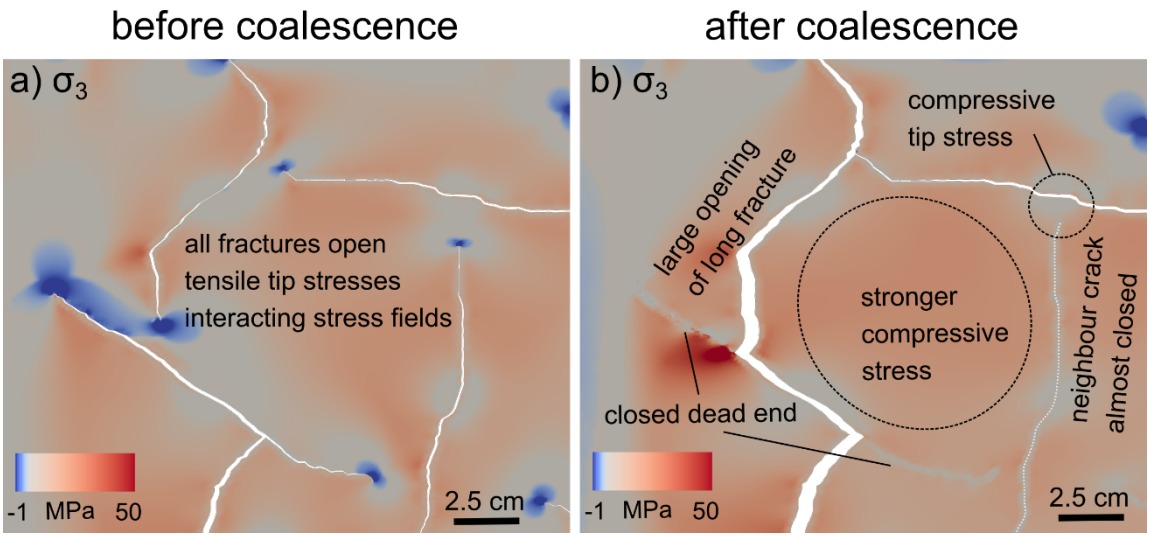

Figure S1. Close-up illustrating smallest principal stress redistribution in the model after fracture coalescence, including mesh deformation (5 times exaggerated). Before coalescence, all displayed fractures show tensile tip stresses of varying magnitudes, as well as interaction of the stress fields with neighboring cracks (a). After an additional propagation step, many of the fractures connect to each other, leading to stress redistribution, strong opening of a long vertical fracture, and closure of dead ends (b). Note that the vertical fracture in the right side of image (b) does not connect to its neighbors, but still shows strongly reduced opening and compressive tip stresses highlighting the local stress interactions captured by the model.

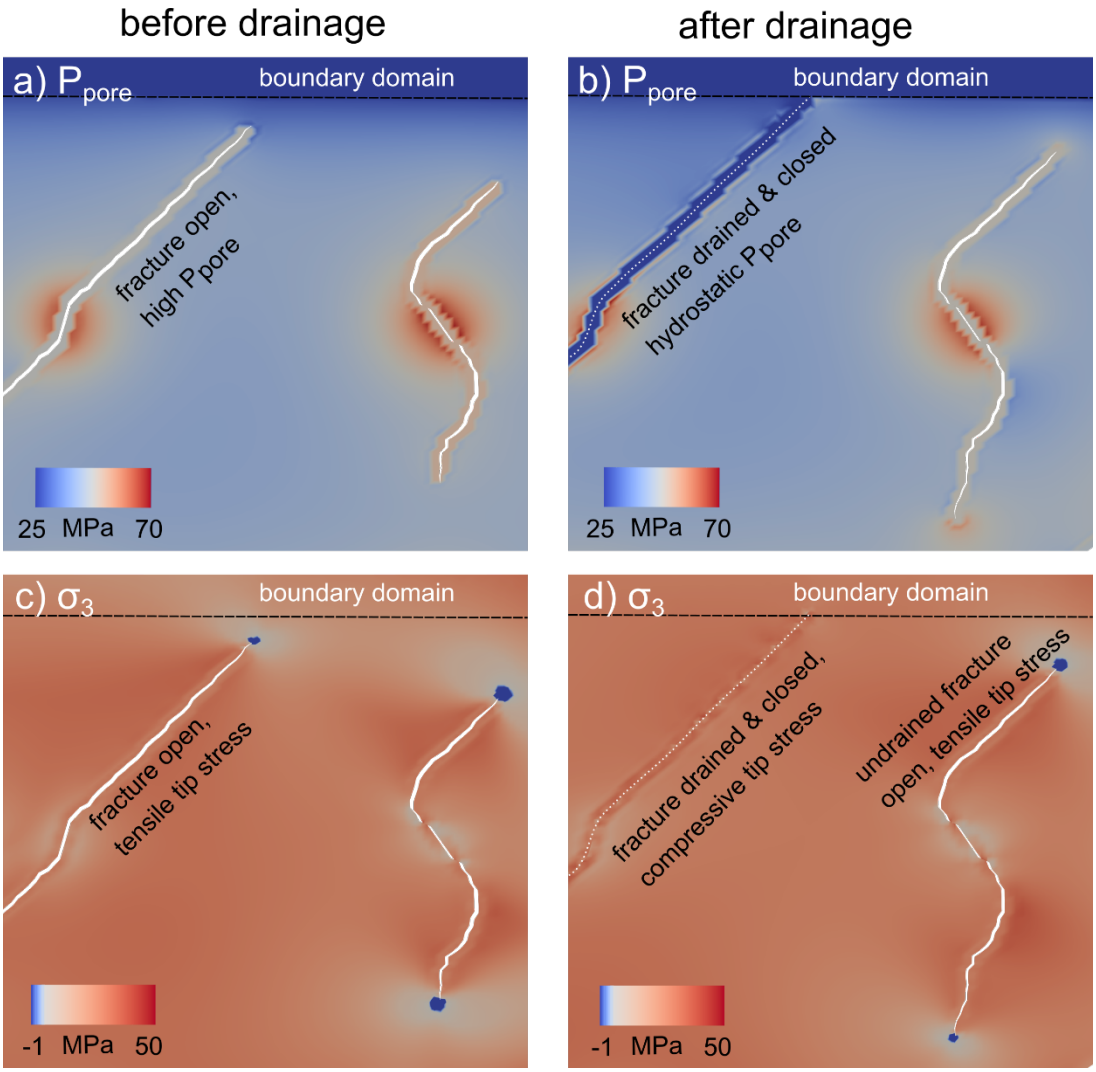

Figure S2. Close-up view of fracture propagation and drainage process displayed as pore pressure (a,b) and smallest principal stress (c,d) observed in the model. Model deformation is included in the displayed imaged, but exaggerated by a factor 5 (for visual clarity). Before drainage, both fractures are overpressured (a) and thus open, and show tensile stress concentration at the tip (c), leading to growth. One of the fractures propagates into the boundary and drains, causing fluid pressure in the fracture to drop to the hydrostatic background level, closure of the fracture, and no more tensile growth (b). In contrast, the undrained fracture adjacent to drained one remains open and overpressured, and maintains tensile tip stresses.

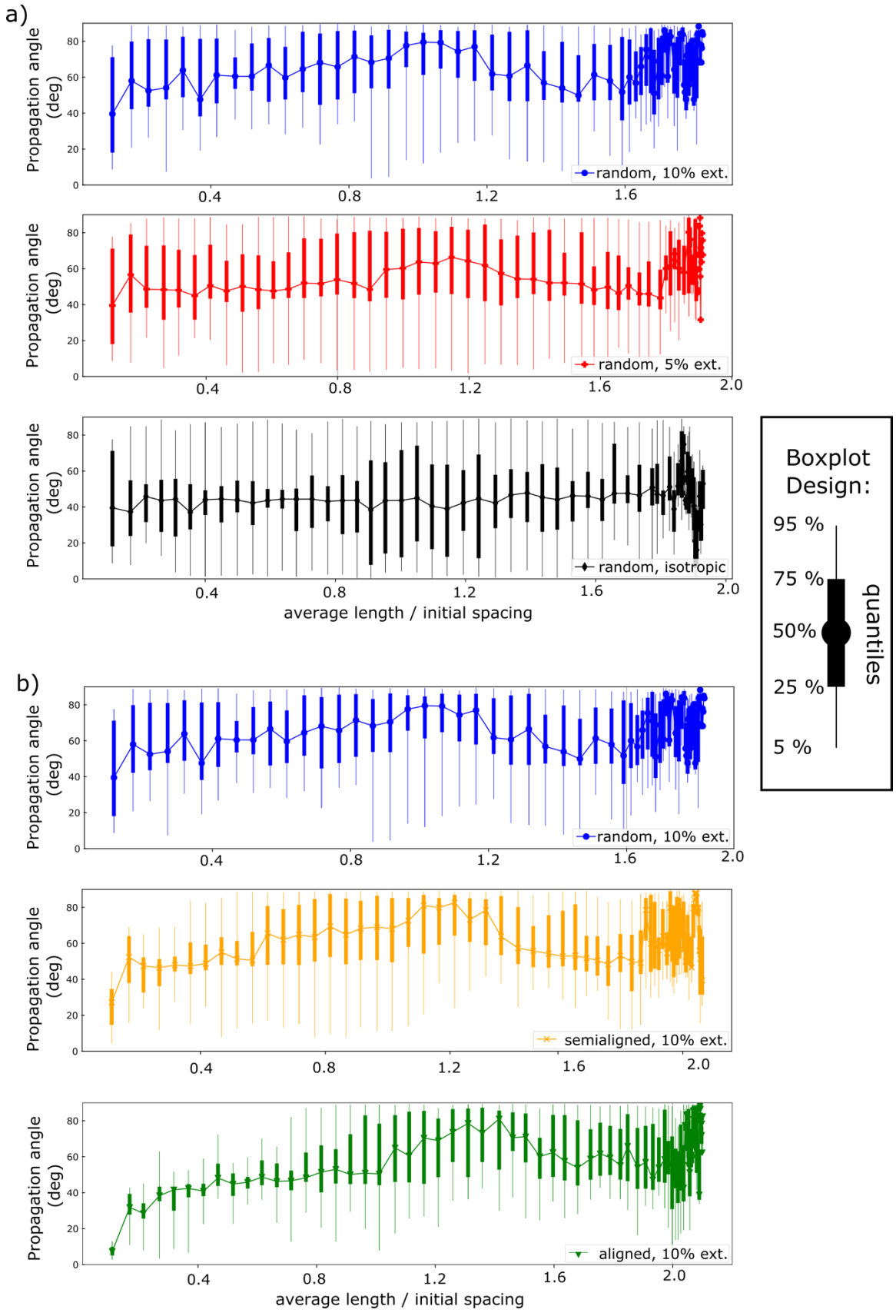
a)
Propagation angle (deg)
random, 10% ext.
random, 5% ext.
random, isotropic
average length / initial spacing
b)
semialigned, 10% ext.
aligned, 10% ext.
Boxplot Design:
95 %
75 %
50%
25 %
5 %
quantiles

Figure S3. Boxplots of the distribution of fracture propagation angle plotted with respect to the horizontal vs. the ratio of average fracture length to the initial spacing. (a) Increasing differential stress from 0 (isotropic) to 10% extensional. (b) Comparison of random, semialigned, and aligned initial crack orientation for a 10% extensional stress configuration. The schematic design explains the boxplot visualization. The random case with isotropic stress shows a widespread and is centered around a median of around 45 degrees throughout the simulation (a). On the other hand, the cases with strong anisotropy (top of a, all curves in b), show a shift of the majority of fracture propagation angle towards higher angles until the maximum is reached. In these cases, at least 75% of the fracture tips propagate at angles of 45-60 degrees to the horizontal, or steeper, during the phase of individual growth (cf. Figure 9).

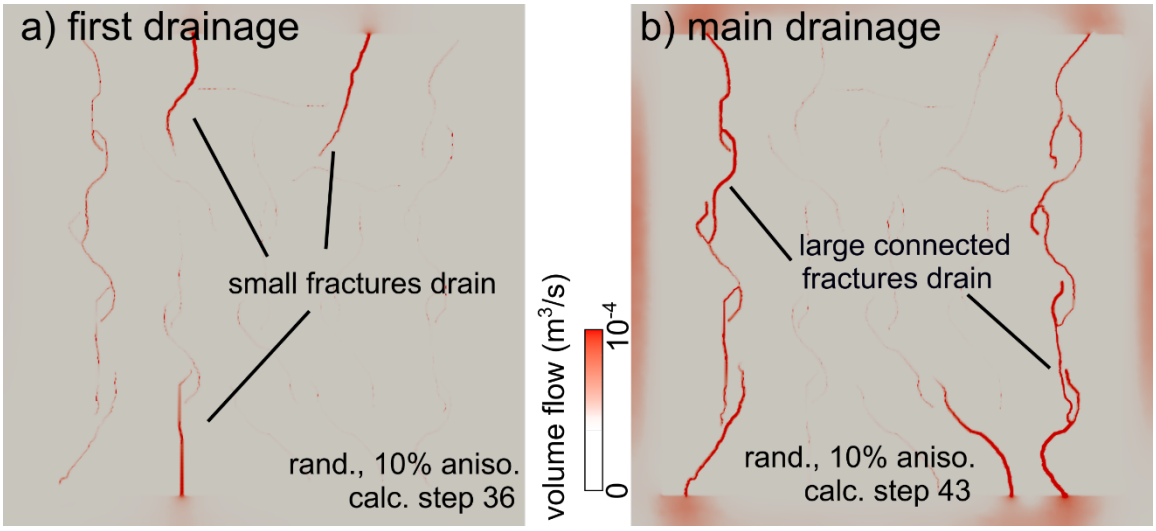

Figure S4. Volume flow field for two different drainage steps in the case of 10% extensional stress anisotropy and random initial orientation. The first drainage step shows three smaller fractures draining and some limited flow within undrained fractures (a). During the main drainage step, two large connected vertical fracture arrays and a single small fracture are drained (b).

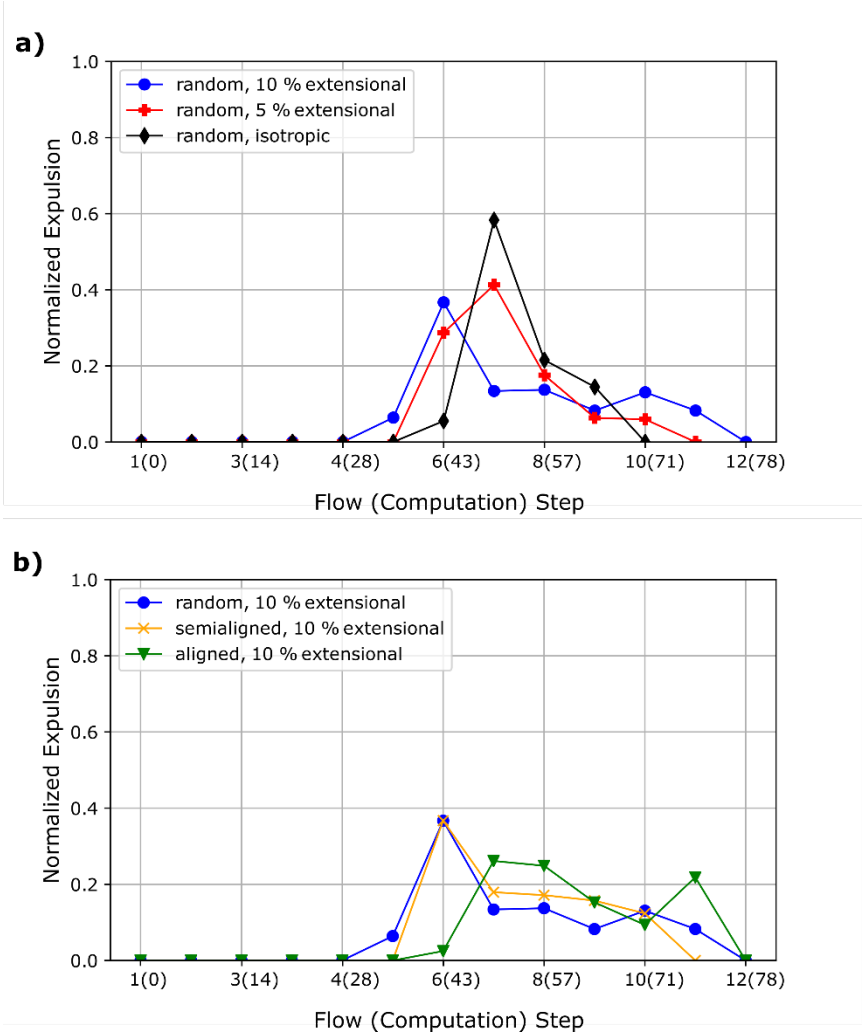

Figure S5. Expulsion (fluid volume flow) from the model domain normalized by the total expulsion at each fluid flow calculation step. We show the curves for random initial fracture orientation under varying differential stress (a) and different initial orientations under 10% extensional stress anisotropy (b).